TECHNISCHE
UNIVERSITÄT
DARMSTADT

Long-Time Simulation of Core-Collapse Supernovae

at the Department of Physics of the Technische Universität Darmstadt

submitted in fulfillment of the requirements for the
degree of Doctor rerum naturalium
(Dr. rer. nat.)

Doctoral thesis
by Carlos Andreas Mattes

First assessor: Prof. Dr. Almudena Arcones
Second assessor: Prof. Dr. Sean Couch

Darmstadt 2018 (year of the viva voce)

Long-Time Simulation of Core-Collapse Supernovae
Langzeit Simulationen von Kernkollapsesupernovae

Accepted dissertation by M.Sc. Carlos Andreas Mattes,
born in Frankfurt am Main, Germany

First assessor: Prof. Dr. Almudena Arcones
Second assessor: Prof. Dr. Sean Couch

Date of submission: 10.07.2018
Date of the viva voce 15.10.2018

Darmstadt 2019 – D17

Please cite this document as:
URN: urn:nbn:de:tuda-tuprints-84388
URI: https://tuprints.ulb.tu-darmstadt.de/id/eprint/8438

This document is provided by tuprints,
E-Publishing-Service of the TU Darmstadt
http://tuprints.ulb.tu-darmstadt.de
tuprints@ulb.tu-darmstadt.de

Abstract

Neutrinos play a crucial role in core-collapse supernovae. An adequate description of the neutrino propagation inside the star, and the neutrino interaction with the stellar material is essential for the simulation of these spectacular astrophysical events. We present the implementation of the Advanced Spectral Leakage (ASL) scheme into the simulation framework `FLASH`. ASL is based on previous gray leakage schemes, and in addition, it takes into account the spectral information of the neutrino distribution in optically thin regions. Moreover, it also models the trapped component of neutrinos in optically thick regions. We show that ASL is capable of producing reasonable results in a direct comparison with the more sophisticated neutrino treatments IDSA and M1 available in `FLASH`. Thereafter, we apply ASL in long-time simulations where we investigate the stability of our simulation setup and discuss the implications on the nucleosynthesis. We close our study with the performance preview of ASL in full 3D simulations which reveals its potential in computationally intensive simulations.

Inhaltsangabe

Neutrinos spielen eine wichtige Rolle in Kernkollapssupernovae. Eine adequate Beschreibung der Neutrinopropagation im inneren des Sterns und die Neutrinointeraktion mit der Sternmaterie sind entscheidend für die Simulation dieser eindrucksvollen astrophysikalischen Ereignisse. Wir präsentieren die Implementierung des Advanced Spectral Leakage (ASL) Schemas in das Simulationsrahmenprogramm `FLASH`. ASL basiert auf vorherigen grauen Abflussschematas, aber zusätzlich berücksichtigt es die spektrale Information der Neutrinoverteilung in optisch dünnen Regionen. Zudem modeliert es noch die gefangene Neutrinokomponente in optisch dichten Regionen. Wir zeigen, dass ASL in der Lage ist annehmbare Ergebnisse zu produzieren in einem direkten Vergleich mit den bereits vorhandenen technisch ausgereifteren Neutrinoverfahren IDSA und M1, welche bereits vorhanden sind in `FLASH`. Wir fahren fort mit der Anwendung ASLs in Langzeitsimulationen in denen wir die Stabilität unserer Simulationskonfiguration untersuchen und die Implikationen für die Nukleosynthese diskutieren. Wir schließen unsere Studie mit der Leistungsvorschau ASLs in kompletten 3D Simulationen, die ASLs Potential in rechenintensiven Simulationen aufweist.

Contents

Chapter 1

Introduction and Motivation

The name supernova is a compound word of the originally Latin words super (above) and nova (new). It refers to the temporal appearance of comparably bright new stars. These events are the result of catastrophic stellar explosions. Our study focuses on a subclass of supernovae which correspond to the death of stars heavier than about ten times the mass of our sun. At the end of stellar evolution, these stars produce extremely heavy cores which collapse due to their own gravitational weight. The release of gravitational binding energy unbinds the stellar envelope and leads to the so called core-collapse supernova (CCSN) explosions. The ejecta of such explosions are rich in freshly produced nuclei which mix into the interstellar medium. About one third of the iron in our galaxy has been produced in such events [62]. The remnant of the stellar core is either a neutron star or a black hole. Especially, the production of neutron stars associates CCSNe with another important nucleosynthesis event, because the merger of a neutron star with either a black hole or another neutron star gives the production sight for the heaviest elements up to uranium, which has recently been confirmed [1]. This makes CCSNe a central ingredient in the chemical evolution of galaxies. Moreover, the passing of an old star is also a trigger for the formation of new stars, because these explosions can produce

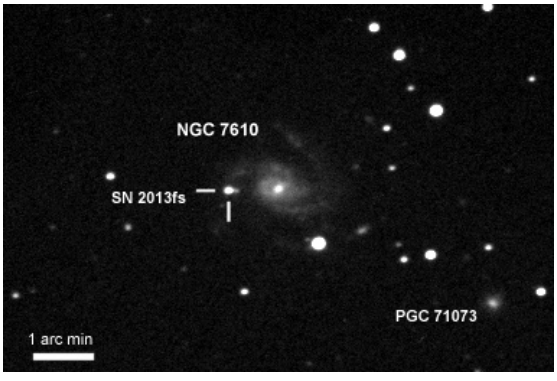

Figure 1.1: Spiral galaxy NGC 7610 including supernova SN 2013fs. Image by David Richards (Aberdeenshire, UK)

the seed perturbation leading to local contractions in molecular clouds (Jeans instability) which initiates the formation of new stars [85].

One of the remaining puzzles in astrophysics concerns the mechanism of these explosions. Only one percent of the potential energy released during the collapse would be sufficient to explode the stellar envelope. However, the major part of the energy is emitted in neutrinos which leave the star with almost no interaction. Understanding the neutrino matter interaction and how it is influenced by multi-dimensional effects, e.g. convection, is still an active field of research. Due to asymmetric motion during the explosion, the emission of gravitational waves is expected which might be observable with newer generations of gravitational wave detectors. Though both neutrino and gravitational wave astronomy are still in a very early stage, in 1987 it was possible to gather about two dozen neutrinos associated with the subsequent visible observation SN 1987A. With today's detectors, a comparable event would count more than ten thousand neutrinos [19]. The core-collapse supernova rate is about one to three events per century. This means that, we can expect a detection combining neutrinos, light and possibly the gravitational wave signal, in the coming century. A theoretical prediction of the ejected composition and its spatial distribution combined with observational data will help us to find the explanation of how CCSNe explode.

Despite the already mentioned SN 1987A another special example of a core-collapse supernova observation is SN 2013fs, see Fig. 1.1, which has been discovered by the Intermediate Palomar Transient Factory [73] in October 2013. The supernova occurred in the spiral galaxy NGC 7610 and has been recorded just about three hours after the stellar disruption. The follow up observations including a variety of telescopes began just other three hours later, making it the earliest supernova explosion observation at present. Among other things, the observational results give new insights about the stellar mass loss during the final years of stellar evolution [152].

1.1 Aim of this Thesis

The aim of this thesis is to close the gap between the onset of explosion and the following shock expansion. We will follow the shock evolution in multi-dimensional simulations within a single simulation setup. This requires the simulation to handle a more than $100,000$ km wide domain with a density rage between 10^0 – 10^{15} g cm^{-3} including discontinuous flows. Additionally, the neutrino physics needs to be incorporated into the setup in a numerically efficient way which will include approximations, but may conserve the input for subsequent nucleosynthesis studies. This will allow us in future to perform parameter studies e.g. variation of progenitor masses, or metallicity.

The thesis is structured as follows: In Chapter 2, we introduce the current theoretical model and understanding of a CCSN. We will briefly describe the final stage of stellar evolution, describe the explosion phases and point on the theoretical challenge of the explosion mechanism. We end the chapter with short summary of the nucleosynthesis sides in a CCSN. Chapter 3 contains a summary of the physical methods. We will recall the basic equations of hydrodynamics and their coupling to the neutrino transport. We will describe the advanced spectral leakage which is an approximate neutrino treatment for

CCSN simulations that will be used in this work. Eventually, we will introduce the simulation framework FLASH which we employ to numerically solve the underlying equations. A detailed comparison between the existing approximate neutrino treatments available in FLASH will be presented in chapter 4. This study includes a comparison in spherical symmetry (1D) as well as in cylindrical symmetry (2D), which also reveals the impact of multi dimensional effects on the neutrino treatments, e.g. convection. Chapter 5 shows the application of ASL in long-time simulations, i.e. simulations of few seconds after the onset of explosion. We will show the evolution for several explosion models and discuss the implications on the nucleosynthesis. We will also mention the weak points of our setup for long-time simulations and our current implementation of ASL where we also formulate possible improvements. We close the chapter with a preview of the ASL performance in full 3D simulations where we show that it has a strong potential due to its numerical efficiency. We finish the thesis with a summary and conclusion in chapter 6.

Chapter 2

Core-Collapse Supernova Theory

The implosion of stellar cores at the end of stellar evolution has been proposed by Hoyle and Fowler in 1960 [59]. However, the early idea, that a thermonuclear runaway of the remaining fuel inside the star yields to the explosion of the envelope, could not been confirmed. In this chapter, we describe the present theoretical modeling of core-collapse supernovae. We begin with a short summary of the stellar evolution of massive stars focusing on the stellar core. This leads us to the progenitor model which is the initial condition for the upcoming collapse phase. The collapse and core bounce are described in Sec. 2.2 and in the following section, we present a plausible explosion mechanism. Finally, we take a closer look at the nucleosynthesis in core-collapse supernovae. The content of this chapter is based on the books, [67, 7, 124] and the reports [13, 149, 63].

2.1 Stellar Core Evolution

Before exploding as a core-collapse supernova, a massive star ($\gtrsim 10\ \mathrm{M}_\odot$) spends most of its time fusing hydrogen to helium in its core. This long-lasting burning stage is called the main sequence phase. In contrast to our sun, the higher central temperature ($\gtrsim 10^7$ K) inside a massive star allows for a more efficient burning process referred to as CNO cycle. This leads to a faster depletion of hydrogen in the center. Once the energy generation drops, the ongoing heat

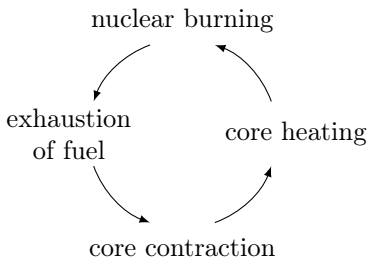

Figure 2.1: Schematic nuclear evolution for the stellar core of a massive star.

transfer towards the surface reduces the central pressure support and results in the contraciton of the stellar core. The consequences for the entire star are rather complicated with regard to the hydrodynamical instabilities in the envelope, e.g. convection, expansion, mass loss. However, the evolution of the stellar core is more predictable. The release of gravitational binding energy heats up the stellar core until the central density and temperature allows for efficient burning of helium into carbon. The new nuclear energy source prevents further contraction. The core passes through several of these nuclear evolution cycles which are represented by Fig. 2.1.

In each cycle, the ash of the previous stage is gradually converted into heavier elements. The new elements are distributed in shells surrounding the core. Usually, the burning continues at the hottest place of each shell which refuels the underlying shell. The nuclear cycle stops when the stellar core consists of iron group nuclei, because these elements have the highest binding energy per nucleon, i.e. the production of heavier elements does not release further energy, but rather consumes energy. With the raising central temperature for each burning stage, the production of thermal neutrinos becomes the dominant energy sink. Once a neutrino is produced, it leaves the star with almost no interaction. Therefore, neutrino cooling, in contrast to other cooling processes e.g. heat diffusion, acts locally. Furthermore, the energy release per nucleon and therewith per mass reduces subsequently for each burning stage. Both, the inner cooling and the reduced mass specific energy density of the fuel, accelerate the

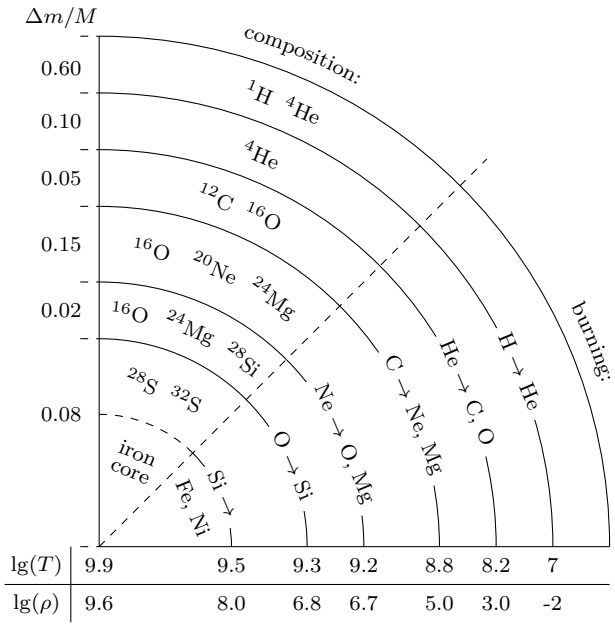

Figure 2.2: Schematic illustration (not to scale) of the "onion skin structure" in the interior of a highly evolved massive star. Along the vertical radius and below the horizontal radius some typical values of the mass, the temperature (in K), and the density (in g cm^{-3}) are indicated. This figure is an adaption of Fig. 35.1 in Ref. [67].

cycles and decouple the core evolution from the envelope. In fact from carbon burning on, the thermal timescale of the star is much larger than the sum of all hydrostatic burning phases which means that any change in the core will not have enough time to adjust the stellar surface temperature. Therefore, it is not possible to determine from its surface temperature whether a star is 10,000 years or 10 hours before exploding as core-collapse supernova.

Fig. 2.2 shows the final structure for a massive star after reaching Silicon burning. It also indicates some typical values for temperature and density and the mass distribution among the shells. Despite the presented burning reactions, there is much more nucleosynthesis occurring during stellar evolution. Especially, the mixing between shells and subsequent (α, n) reactions provide a neutron source which enables the so called s-process. Further information can be found e.g. in Refs. [91, 65].

2.2 Core-Collapse and Bounce

At the high density in the interior of the star, the quantum mechanical nature of the electrons comes into effect. Following the Pauli exclusion principle, the electrons inside the plasma degenerate and provide the dominant pressure source which prevents an early core-collapse. The situation is similar to a white dwarf which is the remnant for low mass stars and also supported by the pressure of degenerate electrons. According to the virial theorem, the internal energy E_i and gravitational energy E_g are related by the equation of state. If inside the core the heat capacity ratio γ is almost constant, then the virial theorem leads to the following relation

$$3(\gamma - 1)E_i + E_g = 4\pi R^3 P(R), \tag{2.1}$$

where R is the core radius, and $P(R)$ is the pressure at the surface of the core. A stable configuration requires a negative total energy,

$$E_{\text{tot}} = E_i + E_g < 0. \tag{2.2}$$

The state of degenerate electrons leads to $\gamma = 5/3$ in the non-relativistic limit. Inserting Eq. 2.1 with $\gamma = 5/3$ and a vanishing surface pressure into Eq. 2.2 leads to the stable configuration describing a typical white dwarf. However, the increasing central density of the core in massive stars forces the electrons to populate energy states beyond the electron rest mass energy equivalent (511 keV). At this ultra-relativistic limit, we obtain $\gamma = 4/3$. If we insert again all numbers and assume a non vanishing pressure at the surface, we do not reach a stable configuration anymore. In the context of white dwarfs, Chandrasekhar derived the upper mass limit for degenerate stars [30][1],

$$M_{ch} \approx 1.46\ (2Y_e)^2\ M_\odot, \tag{2.3}$$

where the electron fraction Y_e gives the number of electrons per baryon. The value of Y_e is not constant in a star. The emission of electron neutrinos during

[1] The value presented in this reference differs due to numerical limitations in the past. The value presented here is taken from Ref. [67]. Additionally, we replaced the mean molecular weight per free electrons μ_e by its inverse, i.e. the electron fraction Y_e.

stellar evolution lowers the value to about $Y_e \approx 0.44$ in the center. In contrast to a white dwarf, the temperature in the center of an evolved massive star exceeds several billion Kelvin. At such conditions, photodisintegration of the iron group nuclei further destabilize the core. A typical photodisintegration process is

$$\gamma + {}^{56}_{26}\mathrm{Fe} \rightleftharpoons 13\alpha + 4n, \tag{2.4}$$

where a gamma ray from the tail of the radiation spectrum decomposes an iron nucleus into thirteen alpha particles and four neutrons. This reaction costs an energy of

$$Q = (13m_\alpha + 4m_n - m_{\mathrm{Fe}})c^2 = 124.4 \text{ MeV}, \tag{2.5}$$

which is taken from the thermal energy of the plasma. As in previous burning cycles, the energy leak is compensated by contraction. However, the increasing density pushes electrons on higher Fermi energies which favors electron captures on nuclei

$$e^- + (Z, A) \rightarrow (Z - 1, A) + \nu_e, \tag{2.6}$$

and on free protons

$$e^- + p \rightarrow n + \nu_e, \tag{2.7}$$

which, again, further reduce the electron pressure component. The release of these neutrinos from the star reduces the total lepton number inside the star. Therefore, the collapse phase is also referred to as deleptonization. In this situation, any contracting perturbation, which as a consequence increases the gravitational acceleration, can no longer be rapidly compensated by the collateral but faster increase of pressure. The stellar core ($R \approx 3000$ km) becomes unstable and collapses. The inner core of ~ 0.8 $\mathrm{M}_\odot$ collapses homologously, which is characterized by a linear increase of infall velocity with respect to radius[2], see Fig. 2.3. At the radius where the infall velocity exceeds the local speed of sound, the matter detaches from the outer core which follows supersonically.

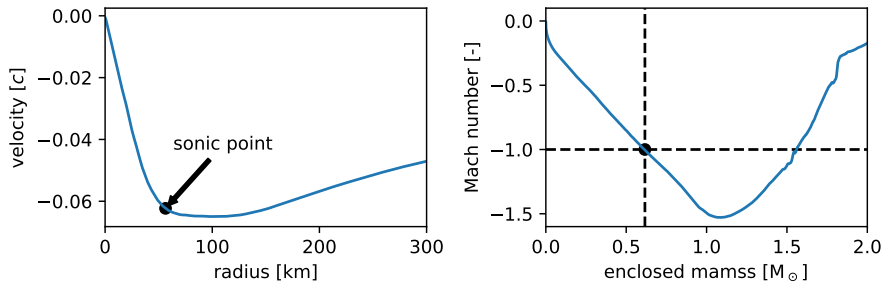

Figure 2.3: Simulation results 10 ms before core bounce. The left panel shows the velocity profile, where the inner core collapses homologously, i.e. $v(r) \sim r$. The right panel shows the Mach number as function of the enclosed mass. In this case, the inner core is about 0.6 $\mathrm{M}_\odot$.

[2] According to Ref. [49], the inner core is essentially the corresponding Chandrasekhar mass for the central conditions.

The core-collapse converts in a timescale of 100 milliseconds about 10^{53} erg of gravitational binding energy into internal energy. When the central density approaches the nuclear density (2.7×10^{14} g cm^{-3}), eventually the repulsive part of the nuclear force is able to stop the collapse. This results in the formation of the so called proto neutron star (PNS). While the new source of pressure gently decelerates the inner core, the outer core abruptly stops in a supersonic collision which forms a surface of discontinuous flow, i.e. the supernova shock. The kinetic energy of the colliding matter is turned into heat which rises the pressure. At the extreme densities inside the PNS ($\geq 10^{12}$ g cm^{-3}), even for neutrinos, the surrounding matter becomes opaque. At this point, the role of neutrinos changes. In contrast to being a local energy sink, neutrinos become a matter constituent holding and moving heat energy inside the PNS.

2.3 Early Explosion Phase

The matter of the outer core continues colliding on the PNS. Under the extreme conditions fast electron capture reactions on free protons produce a large amount of electron neutrinos which cannot leave the PNS and the energy density continues raising. Eventually, the shock surface begins expanding and initiates the explosion. While the shock front propagates outwards, the density below the shock decreases. At some point the matter becomes transparent to neutrinos which results in a strong electron neutrino burst. According to the Rankine-Hugoniot conditions, the pressure difference between inside and outside the shock front determines the shock expansion velocity. The neutrino emission together with the ongoing photodisintegration of iron group nuclei lead to the depressurization and stalling of the shock. Instead of pushing matter away from the core, about 10–20 ms after core bounce, the shock turns into an accretion shock at

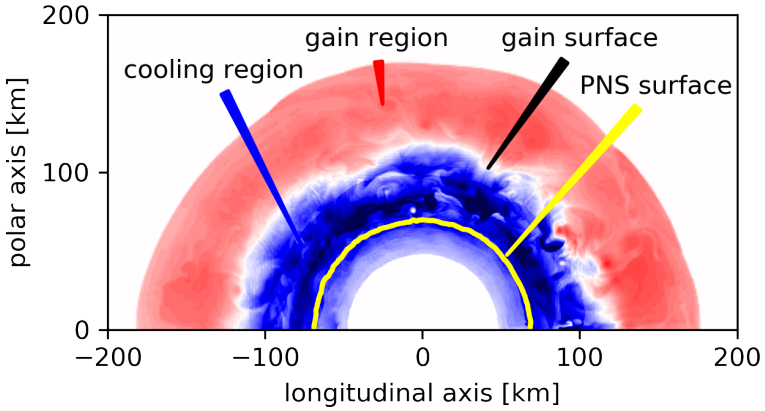

Figure 2.4: Simulation results of the stalled shock at 180 km about 100 ms after core bounce. The red contour below the shock highlights the gain region and blue the cooling region. The intermediate white surface refers to radii where neutrino cooling and heating balance each other. The yellow line marks the contour of 10^{11} g cm^{-3} which indicates the PNS surface.

a radial distance of about 100–200 km. The almost static situation is shown in Fig. 2.4 which presents the result of a numerical simulation at $t = 100$ ms after core bounce. The PNS cools via neutrino emission at its surface. The matter that gets hit by the shock also emits neutrinos but at the same time the intense neutrino flux allows for energy transfer from the streaming neutrinos to the matter. Especially, the absorption of neutrinos on free nucleons, i.e. via

$$\nu_e + n \rightarrow p + e^-, \tag{2.8}$$

$$\bar{\nu}_e + p \rightarrow n + e^+, \tag{2.9}$$

majorly contribute to the neutrino absorption. At the so called gain radius, the neutrino cooling equals the energy gain due to neutrino absorption. For larger radii, neutrino heating dominates which refers to as gain region.

The situation is precarious for the explosion. Either, the shock expansion revives and manages to turn the accretion into an ejection, or the PNS becomes too heavy and collapses into a black hole. The upper mass limit for the PNS is still uncertain. It mainly depends on the equation of state, see Sec. 3.1.3.

2.4 Explosion Mechanism(s)

The still standing problem in supernova theory concerns the shock revival. Despite other possible explosion mechanisms, e.g. magnetohydrodynamic mechanism, see e.g. Refs. [15, 112], we follow the delayed neutrino mechanism introduced by Bethe & Wilson [14]. A detailed discussion on several explosion mechanisms can be found in Refs. [63, 23, 69].

Already in the 1960s, the pioneering works of Colgate & White [32] and Arnett [8, 6] identified the potential of neutrinos to strengthen the shock for a successful explosion. However, the early idea of a prompt explosion after core bounce could not be confirmed by simulations. Usually, the shock stalls and turns into the situation as described in the previous section. In order to revive the shock, Bethe and Wilson in 1985 proposed a mechanism, where delayed neutrino heating close to the shock surface restarts the shock expansion [14]. The mechanism is plausible, because the Kelvin Helmholtz timescale of the hot PNS is about ten seconds where the most efficient cooling comes from the emission of thermal neutrino pairs. Additional (anti-)neutrino pairs are emitted from the hot accretion matter with a total neutrino luminosity of few times 10^{52} erg s^{-1} per neutrino flavor. Neutrino energy deposition close to the shock due to scattering or absorption can turn a fraction of neutrino energy back into thermal energy of the matter. Especially, the presence of free nucleons close to the shock enable the absorption reactions, see Eqs. 2.8 and 2.9, which provide an efficient energy and momentum transfer. The resulting increase in pressure below the shock could revive the shock expansion and eventually turn the accretion behind the shock into the ejection leading to the observable stellar disruption.

More than 30 years after the proposed explosion mechanism, it is still very difficult to confirm. Following Ref. [103], the criterion for a successful explosion can be expressed in terms of timescales. It is the competition between neutrino

energy deposition in the gain layer,

$$t_{\mathrm{heat}} = \frac{\int_{M_{\mathrm{gain}}} \epsilon \, \mathrm{d}m}{\int_{M_{\mathrm{gain}}} (\mathcal{H} - \mathcal{C}) \, \mathrm{d}m}, \tag{2.10}$$

and the advection of matter into the cooling region,

$$t_{\mathrm{adv}} = \int_{R_{\mathrm{gain}}}^{R_{\mathrm{shock}}} v_r^{-1} \mathrm{d}r. \tag{2.11}$$

In Eq. 2.10, M_{gain} refers to the mass of the gain region, ϵ is the mass specific thermal energy inside the gain region, $\mathcal{H}$ and $\mathcal{C}$ are the mass specific neutrino heating and cooling source terms, respectively. The radii R_{gain} and R_{shock}, and the radial velocity v_r in Eq. 2.11 are understood as angle averaged quantities, compare to Fig. 2.4. Generally, the condition $t_{\mathrm{adv}}/t_{\mathrm{heat}} > 1$ indicates the onset of explosion. Already Bethe and Wilson have been aware of the importance of multi dimensional effects on the mechanism, but those calculations have been too expensive at this time. One important feature of non-spherical flows is that they elongate the duration of matter in the gain region. Convection can transport cool matter from the shock to the gain surface where neutrino heating is strongest, and at the same time move the hot matter from the gain radius to the shock instead of accreting it on the PNS. Additionally, the instability of the accretion shock (SASI; [18]) shows that the spherical symmetry of the shock wave is easily broken. The SASI builds up a feedback cycle of aspherical accretion and resulting pressure waves from the PNS surface propagating back to the shock which causes an oscillatory deformation of the shock surface. It also leads to secondary shocks that dissipate kinetic energy and produce extra heating and higher entropy which strengthens the convective activity and additionally pushes the shock. In order to trigger the SASI or non radial flows, the core needs to develop asymmetries. These could arise naturally from the accretion of convective shells and the seed perturbation therein, see Refs. [38, 99]. However, since stellar evolution models are calculated assuming spherical symmetry and applying parameterized convection, the detailed multi-dimensional structure of a CCSN progenitor is unknown. First attempts to evolve a massive star through its last burning stage have been made by Couch et al. [35], and Müller et al. [101, 100].

If the sum of all multi-dimensional effects leads to a robust delayed neutrino explosion mechanism, still needs to be shown. The impact of rotation, see e.g. Ref. [134], or magnetic fields, see e.g. Ref. [98], may also play a crucial role in some events.

2.5 Nucleosynthesis after Explosion

Once the revival has been successful, the shock can further propagate through the star. The matter that gets hit by the shock rapidly heats up. While the peak temperature still reaches up to several million Kelvin, it allows for the production of iron group nuclei. Especially, the production of radioactive nuclei (e.g. ^{56}Ni, ^{44}Ti) becomes important after the stellar disruption, since the radioactive decay provides the energy source for the subsequent supernova light curve and therewith becomes a direct observable, see e.g. Refs. [50, 51]. The

asymmetries of the explosion at very small scales are likely imposed on the large scale ejecta which may explain the fast moving iron/nickel rich ejecta and asymmetries in the supernova remnant Cassiopeia A, see Refs. [61, 51] for the observation and Ref. [146] for the reproduction by a simulation. Additional mass ejection originate from the PNS surface. Once the accretion stops, the hot PNS begins its Kelvin-Helmholtz cooling phase. Therein, the neutrino luminosity initially is still at few times 10^{52} erg s^{-1}, which is sufficient to evaporate a small fraction of the PNS surface during the first few seconds after the end of accretion. Although, the total mass of this ejecta is small, it provides a hardly inimitable side for nucleosynthesis. In this so called neutrino driven wind [138], the acceleration can be strong enough to reach supersonic velocity. Close to the PNS surface, the matter mainly consists of free neutrons and protons, but also contains a minor fraction of light nuclei [5]. When the wind pushes the matter further away from the PNS, it expands and as a consequence, the density and temperature decrease. In this situation, the free nucleons recombine to form alpha particles which further combine to form heavy seed nuclei. The excess of free neutrons, the so called neutron-to-seed ratio, determines the further evolution. The conditions can establish a neutron capture-disintegration equilibrium between free neutrons and neutron rich seed nuclei. Then, the expansion cools the matter rapidly so a non-equilibrium distribution of neutron rich nuclei can freeze out which subsequently decays to stable nuclei. This process of rapid neutron captures is referred to as r-process, see e.g. Ref. [9]. In contrast to the shock heated material, it may also contain isotopes far beyond the iron group. The favorable conditions for the production of heavy nuclei are high entropies, low electron fractions, and short expansion timescales [92]. However depending on the change in electron fraction due to the interaction with the neutrinos, the wind can even become proton rich and therefore move through different nucleosynthesis paths producing less heavy elements, see e.g. Ref. [2].

Fig. 2.5 shows an example of a long-time simulation in spherical symmetry using the setup as described in Sec. 3.3. The red line shows the shock position and the blue line indicates the PNS radius. The dashed lines reveal the fluid motion. Fluid elements that cross the shock after about 500 ms correspond to the nucleosynthesis as initially described. After about 1 s fluid elements are directly emitted from the PNS surface, which is the previously discussed neutrino driven wind.

The dynamic simulation of neutrino driven winds and the following extraction of nucleosynthesis yields is very challenging. Therefore, the first studies to determine the relevant conditions have been made with static models, see e.g. Ref. [120]. Still at present, these models are relevant for systematic studies of nuclear or astrophysical uncertainties, and also to estimate the likelihood of different nucleosynthesis paths in the wind ejecta, see e.g. Ref. [143, 17]. The first hydrodynamic simulations focusing on CCSN nucleosynthesis were based on spherically symmetric models which were strongly parameterized, e.g. introducing a parameter to control the location of ejecta-remnant interface (mass-cut), see e.g. Ref. [150]. The complex neutrino dynamics leading to the explosion has typically been simplified by a piston or thermal bomb approach. While such simulations allows for the study of a large fraction of shock heated material, the prediction of the innermost ejecta becomes sensitive to the parameter choice. An improvement has been made with simulations including the PNS which have been evolved for several seconds after core bounce. These simulations were able

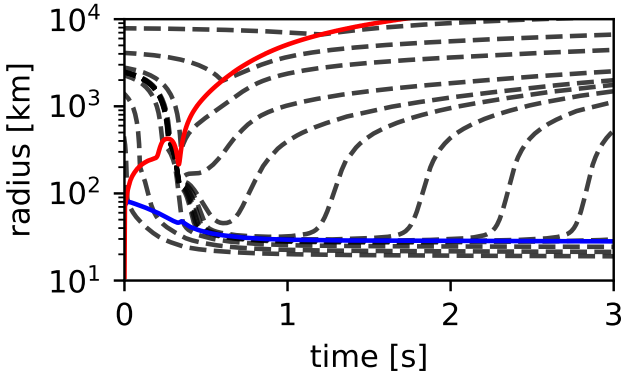

Figure 2.5: Simulation results of an explosion model in spherical symmetry. The red line shows the shock position and the blue line marks the contour of 10^{11} g cm^{-3} which indicates the PNS surface. The dashed lines represent fluid elements which follow the underlying velocity field.

to produce a neutrino driven wind. In contrast to the static models, these simulation results also reproduce the wind termination shock, which evolves when the supersonic wind collides with the subsonic earlier ejecta, see e.g. Refs. [4, 3]. Since the explosions are artificially induced, the neutrino interaction remains a major uncertainty. A further improvement has been made, by incorporating the neutrino interaction into the explosion trigger in order to make the simulation more consistent, see e.g. Refs. [118, 106, 44]. However, these simulations did not intend to reproduce the neutrino driven wind and were only evolved for about 1 s after core bounce which is not sufficient to follow the neutrino driven wind. The most accurate description of neutrino-matter interaction can be found in "self-consistent" neutrino explosions which are only reproducible for low mass progenitor explosions ($\gtrsim 10$ M$_\odot$ electron capture supernovae) or low mass core-collapse supernovae assuming axial symmetry, see e.g. Ref. [55, 144]. Finally, the accurate and dynamic simulation of supernova ejection will require "self-consistent" neutrino explosions in full 3D, since the dimension will likely have an impact on the exposure time of the innermost ejecta with the region of strong neutrino interaction and therewith set the initial conditions for the nucleosynthesis. Furthermore, the investigation of the neutrino driven wind will require simulations beyond one second after the onset of explosion. Unfortunately at present, such 3D long-time simulations are computationally not accessible.

2.6 Supernova Remnants

We previously discussed the precarious situation of the stalled shock. If the star is not able to launch the explosion, the core will certainly collapse to a black hole. However, even after a successful explosion, the PNS can still collapse to a black hole due to either fall back material, or ongoing accretion in the multi dimensional case. Only if the explosion shuts down the accretion and the PNS is light enough to be supported by the EoS at low temperature, the PNS can

turn into a regular neutron star. The naive idea that the remnant depends on the initial main sequence mass of a star could not be confirmed [141, 46]. In fact, the explosiveness of a star is determined by the matter distribution just before the onset of the collapse which due to the highly non-linear burning evolution disconnects from the early main sequence distribution. Explosion criteria have been developed, see Refs. [109, 46], where especially the average density of the core (compactness) appears critical. In the previous section, we already mentioned the asymmetric matter ejection of CCSN. Due to momentum conservation, these asymmetric explosions result in natal kicks and spins of the inner compact object, see e.g. Ref. [11] for observations and Ref. [145] for simulations where the kick is explained by the so called "gravitational tug boat mechanism".

Chapter 3

Physical Methods

In order to simulate the core-collapse and the explosion of massive stars, one needs to solve the equations of hydrodynamics coupled with the long-ranging electromagnetic, gravitational, and neutrino field. The most general framework is a general relativistic formulation of the underlying equations, but solving these equations is very time consuming and therefore not suitable for long-time evolution studies (beyond one second after the onset of explosion). Our goal is to investigate the nucleosynthesis of supernova ejecta by extracting fluid particles representing as many nucleosynthesis conditions realized in core-collapse supernovae as possible.

In sect. 3.1, we recall the equations of hydrodynamics and discuss the relevant simplifications in order to treat a mixture. We also introduce the equation of state for the stellar plasma and show how we can approximate the effects of general relativity on the gravitational potential. In the following section, we describe our approximate neutrino transport scheme and how it is coupled to the equations of hydrodynamics, and in the last section, we give more details on the numerical setup pointing on some important techniques.

3.1 Hydrodynamics

Most of its lifetime, a star remains in hydrostatic equilibrium in this situation the gravitational acceleration is compensated by an increase in pressure. In the non-relativistic case this can be written as

$$\frac{\mathrm{d}P}{\mathrm{d}r} = -G\frac{M(r)\rho}{r^2}. \tag{3.1}$$

Here, P is the pressure, r is the radial distance to the center, G is the gravitational constant, ρ the mass density, and M is the enclosed mass at the given distance. If this equilibrium does not hold anymore, the matter distribution begins to change. In this section, we will derive and discuss the underlying equations of motion. In a more general setup, we would also need to include the effect of magnetic fields, but in this thesis these are excluded. The contend of this section is based on the textbooks: [95, 60, 129].

3.1.1 Conservation equations

The state of a many body system in kinetic theory is described by the particle distribution function $f(\mathbf{q}, \mathbf{p}, t)$ which is so defined that

$$f(\mathbf{q}, \mathbf{p}, t)\mathrm{d}V_q\mathrm{d}V_p \tag{3.2}$$

is the number of particles which, at time t, have position lying within a volume V_q about $\mathbf{q}$ and momenta within a momentum-space volume $\mathrm{d}V_p$ about $\mathbf{p}$. The time evolution of the system is described by the **Boltzmann transport equation**

$$\left(\frac{\partial}{\partial t} + \frac{\mathbf{p}}{m} \cdot \nabla_q - \nabla_q \Phi \cdot \nabla_p\right) f = \left(\frac{\partial f}{\partial t}\right)_{\text{coll}}, \tag{3.3}$$

where ∇_q, ∇_p are, respectively, the gradient operators with respect to $\mathbf{q}$ and $\mathbf{p}$, m is the single particle mass, and Φ is the potential of an external force. The right hand side describes the change of f due to particle collisions. To investigate non-equilibrium phenomena, we must solve Eq. 3.3, with given initial conditions, to obtain the particle distribution function as a function of time. However, this requires a model of the collision term. In order to avoid an explicit modeling, a solution can be derived from the fact that in any particle collision there are dynamical quantities that are conserved. Assuming that $\chi(\mathbf{q}, \mathbf{p})$ is such a conserved quantity for a particle at $\mathbf{q}$ with momentum $\mathbf{p}$ then the relation

$$\int \chi \left(\frac{\partial f}{\partial t}\right)_{\text{coll}} \mathrm{d}V_p = 0 \tag{3.4}$$

holds. Defining the particle density $n(\mathbf{q}, t)$ and the average value $\langle A \rangle(\mathbf{q}, t)$ by

$$n \equiv \int f \, \mathrm{d}V_p, \tag{3.5}$$

$$\langle A \rangle \equiv \frac{1}{n} \int A f \, \mathrm{d}V_p, \tag{3.6}$$

we can multiply Eq. 3.3 with any conserved quantity χ and integrate the momentum space to obtain

$$\frac{\partial}{\partial t}\left\langle n\chi \right\rangle + \nabla_q \cdot \left\langle n\chi \frac{\mathbf{p}}{m} \right\rangle - n\left\langle \frac{\mathbf{p}}{m} \cdot \nabla_q \chi \right\rangle - n\left\langle \nabla_q \Phi \cdot \nabla_p \chi \right\rangle = 0. \tag{3.7}$$

The typical set of conserved quantities include

$$\chi = m \qquad \text{(mass)} \tag{3.8}$$

$$\chi = m\mathbf{u} \qquad \text{(momentum)} \tag{3.9}$$

$$\chi = \frac{m}{2}|\mathbf{w}|^2 \qquad \text{(thermal energy)} \tag{3.10}$$

where $\mathbf{w}$ is defined by the decomposition of the particle velocity $\mathbf{u} = \mathbf{p}/m$ into its average $\mathbf{v} = \langle \mathbf{u} \rangle$ value and the remaining thermal motion $\mathbf{w}$, i.e.

$$\mathbf{u} = \mathbf{v} + \mathbf{w}. \tag{3.11}$$

Introducing the mass density ρ, and the internal energy ϵ by

$$\rho(\mathbf{q},t) = mn(\mathbf{q},t), \tag{3.12}$$

$$\epsilon(\mathbf{q},t) = \left\langle \frac{|\mathbf{w}|^2}{2} \right\rangle, \tag{3.13}$$

the corresponding conservation equations for each χ can be written as follows:

mass:

$$\frac{\partial \rho}{\partial t} + \nabla_q \cdot (\rho \mathbf{v}) = 0 \tag{3.14}$$

This equation is usually referred to as *Continuity Equation.*

momentum:

$$\frac{\partial (\rho \mathbf{v})}{\partial t} + \nabla_q \cdot (\rho \langle \mathbf{u} \otimes \mathbf{u} \rangle) + \rho \nabla_q \Phi = 0, \tag{3.15}$$

where $\mathbf{u} \otimes \mathbf{u}$ is the dyadic product of the particle velocity. Together with eq.3.11 and considering the fact that the fluid velocity $\mathbf{v}$ already describes a mean value and that the thermal motion is a random motion, i.e. $\langle \mathbf{w} \rangle = \mathbf{0}$, the expectation value of the dyadic product splits into

$$\langle \mathbf{u} \otimes \mathbf{u} \rangle = \mathbf{v} \otimes \mathbf{v} + \langle \mathbf{w} \otimes \mathbf{w} \rangle, \tag{3.16}$$

which leads to the *Navier-Stokes Equation*

$$\frac{\partial (\rho \mathbf{v})}{\partial t} + \nabla_q \cdot (\rho \mathbf{v} \otimes \mathbf{v}) + \nabla_q \cdot \mathbf{\Pi} = -\rho \nabla_q \Phi. \tag{3.17}$$

There are many ways of modeling the so called stress tensor $\mathbf{\Pi} = \rho \langle \mathbf{w} \otimes \mathbf{w} \rangle$ which do not violate the second law of thermodynamics. The most simplest model leads to the *Euler Equation.* It assumes a pure isotrope stress $\mathbf{\Pi} = P\mathbf{I}$ which implies that there is no mixing of momenta into different directions or conversion of fluid velocity into thermal energy, or in other words that there is no viscosity. Here, P is the fluid pressure given by the equation of state (see Sec. 3.1.3 for more details) and $\mathbf{I}$ is the identity matrix.

energy:

$$\frac{\partial (\rho E)}{\partial t} + \nabla_q \cdot (\rho E \mathbf{v} + \mathbf{\Pi} \mathbf{v} + \mathbf{h}) = -\rho \mathbf{v} \cdot \nabla_q \Phi, \tag{3.18}$$

where $E = \frac{1}{2}|\mathbf{v}|^2 + \epsilon$ is the specific total energy and $\mathbf{h} = \rho \langle \frac{1}{2} |\mathbf{w}|^2 \mathbf{w} \rangle$ is the heat flux. Modeling the heat flux in a thermodynamic consistent way results in the first order to the well known heat diffusion equation where the heat flux is proportional to the temperature gradient. In our further study, we will neglect this term assuming that $\mathbf{\Pi} \mathbf{v} \cdot \mathbf{n} \gg \mathbf{h} \cdot \mathbf{n}$ for any direction vector $\mathbf{n}$.

3.1.2 Multi-Component Flows

The above deviation of the equations of hydrodynamics is only valid for systems of identical interacting particles. However, the stellar plasma consists of several particles which interact with each other. This leads to a coupled system of Boltzmann Equations. There are two types of particle collisions classified as elastic scatterings and reactions. In elastic scatterings, the mass, momentum,

and energy of the colliding particles are conserved in the collision process. Assuming that the velocities of colliding particles are uncorrelated, which is the case in thermal equilibrium, the binary elastic collision term between species i and j can be written as

$$\left(\frac{\partial f_i}{\partial t}\right)_{\text{coll,el}} = \iint \frac{q_{ij}}{M}\left(\frac{\partial \sigma}{\partial \Omega}\right)\left(f_i' f_j' - f_i f_j\right)\, \mathrm{d}\Omega\, \mathrm{d}\mathbf{p}', \tag{3.19}$$

where $q_{ij} = |\mathbf{p_i} - \mathbf{p_j}|$ is the momentum transfer, M is the reduced mass, and $\left(\frac{\partial \sigma}{\partial \Omega}\right)$ is the differential cross section. In the stellar plasma, these collisions ensure that the fluid velocity is representative for all nuclear species, i.e. $\mathbf{v} \equiv \mathbf{v}_i = \mathbf{v}_j$.

Taking into account inelastic scattering processes or reactions is more difficult, because they lead to additional source terms for the non-conserved quantities. Deriving the hydrodynamics equations for such a system of coupled Boltzmann Equation leads to a coupled system of conservation equations for each species. Considering the approximations of previous section leads to

$$\frac{\partial(\rho X_i)}{\partial t} + \nabla_q \cdot (\rho X_i \mathbf{v}) = \rho R_i \tag{3.20}$$

$$\frac{\partial(\rho \mathbf{v})}{\partial t} + \nabla_q \cdot (\rho \mathbf{v} \otimes \mathbf{v}) + \nabla_q P + \rho \nabla_q \Phi = 0 \tag{3.21}$$

$$\frac{\partial(\rho E)}{\partial t} + \nabla_q \cdot (\rho E \mathbf{v} + P\mathbf{v}) + \rho \mathbf{v} \cdot \nabla_q \Phi = \rho \epsilon_{\text{nuc}}, \tag{3.22}$$

where X_i and R_i are the mass fraction and the production rate of the i-th species, respectively, and ϵ_{nuc} is the mass specific energy generation rate by all combined reactions. The mass fractions and production rates follow the relations,

$$\sum_i X_i = 1 \;\text{ and }\; \sum_i R_i = 0, \tag{3.23}$$

which is a consequence of the mass conservation.

In a numerical setup, it is common to include the summed mass fraction equations which is equivalent to Eq. 3.14. This additional equation helps to guarantee the relations 3.23, which numerically are difficult to hold. It allows for a re-normalization of X_i after each simulation step. Note that the number of nuclei included in a simulation usually does not represent the total abundance of any possible nucleus, moreover it consists of key isotopes relevant for the energy source term which couples to the energy conservation Eq. 3.22 and therefore may change the overall dynamics. In order to get the abundances of the stellar material one usually post processes the nucleosynthesis on tracers, i.e. solutions of the initial value problem

$$\frac{\partial \mathbf{q}}{\partial t} = \mathbf{v}(\mathbf{q}, t), \tag{3.24}$$

for a given position $\mathbf{q}$ inside the star. Since in astrophysical events, nuclei and nuclear reactions are important energy sources, were the energy release leads to a significant mass excess, the mass in classical sense is not conserved. The conserved quantity is the baryon number and therefore we should replace the mass density ρ by the baryon density n_B and call X_i the baryon fraction. In the context of nuclear reactions, it is useful to define the abundance

$$Y_i \equiv \frac{n_i}{n_B} = \frac{X_i n_B}{A_i n_B} = \frac{X_i}{A_i} \tag{3.25}$$

where n_i is the number density of the i-th particle which is related to the particle distribution function. The baryon density is given by

$$n_B = \sum_i A_i n_i, \tag{3.26}$$

which counts the total number of nucleons per volume. In order to regain the classical picture of mass conservation, it is common to define an arbitrary baryon mass which relates the baryon density to the classical mass density. A common choice is the atomic mass unit m_u which is defined as the 12^{th} part of the ground state mass of carbon twelve.

3.1.3 Equation of State

Subject of the equation of state (EoS) in hydrodynamics is finding a closure relation for the above system of partial differential equations, Eqs. (3.14, 3.17, 3.18). The free variable that needs a physical modeling is the pressure P which should be expressed as a function of the other variables.

Another view on the EoS is that it includes the microscopic interactions coupling all the matter constituents. Each of these interactions have a corresponding interaction range induced by the interaction potential. Depending on the cross section, particle density, and particle velocities, the entire set of these interactions is related to a corresponding mean free path which is the average distance a particle covers between collisions. If the interaction range and the mean free path is small compared to the macroscopic length- and timescale, the system reaches local thermal equilibrium (LTE). In this case, the particle distribution function f does only depend on the locally defined temperature T. The local state is determined by the partition function Z which is given by

$$Z = \mathrm{Tr}\bigg(\exp\bigg(-\frac{\hat{H}}{k_B T}\bigg)\bigg). \tag{3.27}$$

Here, $\hat{H}$ is the Hamilton operator of the system of interacting particles. The corresponding thermodynamical potential is the Helmholtz free energy F defined as

$$F = -k_B T \log Z, \tag{3.28}$$

and the thermodynamic quantities (EoS) follow from the fundamental relation

$$\mathrm{d}F = -P\mathrm{d}V - S\mathrm{d}T + \sum_i \mu_i \mathrm{d}N_i, \tag{3.29}$$

where S is the entropy, μ_i the chemical potential and N_i the particle number of the i^{th} independent constituent. Now, we need to derive an ansatz for the partition function, or equivalently the Helmholtz free energy. A desirable form would split the Helmholtz free energy in its constituents, i.e.

$$F = \sum_i F_i, \tag{3.30}$$

but as previously discussed, the constituents interact with each other. As a consequence, we expect a Hamilton operator of the form

$$\hat{H} = \sum_i \hat{H}_i^0 + \hat{V}_i^{\text{intra}} + \sum_j \mathcal{C}_j \hat{V}_{i,j}^{\text{inter}}, \tag{3.31}$$

which splits the Hamilton operator for each constituent i into a non-interacting Hamilton operator[1] $\hat{H}_i^0$, and interaction potentials $\hat{V}_i$ accounting for interactions between particles of the same constituent (intra), and interactions $\hat{V}_{i,j}^{\text{inter}}$ between particles of different constituents (inter), respectively. The factor $\mathcal{C}_j$ prevents double counting. If the mean free path is large compared to the interaction range, then the interaction becomes point like and the dominant term is given by the non-interacting Hamilton operator. In this case a good approximation is given by a non-interacting system. Moreover, the partition function splits into the product of traces in the Fock subspace of the constituent, i.e.

$$Z = \prod_i \text{Tr}\Big(\exp\Big(-\frac{\hat{H}_i^0}{k_B T} \Big) \Big), \tag{3.32}$$

which after application of the logarithm product rule conforms to eq.3.30. However, if the range of the scattering potential is large, or if the particle density increases, then this assumption may become very inaccurate, and an adequate description may require additional correction terms. The challenge in deriving the partition function for interacting systems is that the interactions between particles create quantum correlations. As a consequence, we may expect a highly entangled quantum state. Depending on the interaction, there exist proper approximations in order to extract the energy eigen states, i.e. mean-field theory, Greens function methods, coupled clusters, density functional theory, etc.

The relevant matter constituents in the stellar core, before and after collapse, are nuclei, nucleons, photons, electrons, positrons, and neutrinos [58]. Similar to photons in the stellar atmosphere, also for neutrinos the LTE becomes invalid when the corresponding mean free path becomes comparable to the macroscopic length scale. As a consequence, a separate modeling of the neutrino evolution is needed and presented in Sec. 3.2. For the remaining constituents, we make the previously discussed ansatz, Eq. 3.30, for the Helmholtz free energy

$$F \approx F_{\text{nuc}} + F_{\text{ion}} + F_{\text{rad}} + F_{\text{ele}}. \tag{3.33}$$

The first term F_{nuc} describes the contribution of the nucleons, i.e. unbound protons and neutrons. This term becomes relevant beyond nuclear density, when the nucleons stream out of nuclei. The nucleons are a very good example for the required many body interactions. If we naively assume a non-interacting fermi-gas, we would arrive at an EoS which could not support neutron stars beyond 0.7 $M_\odot$. This would be in contradiction to the observation of neutron stars, see e.g. chapter 5.5 in Ref. [124]. During the last two decades, more EoS models for nuclear matter were developed, that are able to describe the formation of neutron star using parameterized models, e.g. Ref. [72], mean-field theory, e.g. Ref. [58], chiral effective field theory, e.g. Ref. [56], etc. The second term F_{ion} accounts for nucleons bound in nuclei. The range of the Coulomb potential is large enough that the coupling to electrons and among the nuclei needs to be taken into account. A common ansatz is the single nucleus approximation, see Ref. [151], where the diversity of nuclei is described by a single representative nucleus with mass number $\bar{A}$ and charge number $\bar{Z}$.

[1] $\hat{H}_i^0$ can be written as a tensor product of single particle Hamilton operators.

These numbers are defined by

$$\bar{A} = \big(\sum_i Y_i\big)^{-1}, \tag{3.34}$$

$$\bar{Z} = \bar{A}\sum_i Z_i Y_i, \tag{3.35}$$

where Y_i is the abundance as defined in Eq. 3.25 and Z_i is the charge number of the i^{th} nucleus. This reduces the set of charged particles to ions, electrons, and positrons. In the context of the stellar plasma, we expect a large mean free path for ions and degenerate electrons. The degeneracy prevents that all electrons participate in scattering interactions due to Pauli blocking. Therefore, the contribution of the Coulomb interaction F_C can be treated as a perturbation on the non-interacting system. For simplicity, we add these contributions into $F_{\rm ele}$. A detailed discussion on F_C can be found in Refs. [119, 16]. The remaining contribution of the ions is described by an mono atomic ideal gas of particle density $n_B/\bar{A}$. Its Helmholtz free energy results in

$$F_{\rm ion} = \frac{3}{2}\frac{N_B}{\bar{A}}k_B T - TS_{\rm ST}, \tag{3.36}$$

where $S_{\rm ST}$ is given by the Sackur-Tetrode equation (see e.g. Chapter 3 in Ref. [45]). The third term $F_{\rm rad}$ accounts for the photon radiation. In the stellar interior, photons follow the Stefan-Boltzmann law, i.e.,

$$F_{\rm rad} = -\frac{1}{3}\left(\frac{\pi^2 k_B^4}{15c^3\hbar^3}\right)VT^4. \tag{3.37}$$

The last term $F_{\rm ele}$ accounts for electrons and positrons, as well as for the Coulomb corrections F_C. At finite temperature, the Helmholtz free energy of a free fermi-gas does not have a closed analytical form and includes the solution of Fermi integrals. Typically, it is derived from the grand canonical ensemble and later Legendre transformed to the Helmholtz free energy, see e.g. chapter 8.6 and 11.1 in Ref. [60].

Now, that we have an expression for the Helmholtz free energy, we need to choose a set of independent thermodynamic variables, that describe the state. The charge neutrality sets a constraint on the charged particles which we use to determine the electron and positron number. The photon contribution is only temperature dependent. The resulting EoS is then determined by the independent variables (T,V,N_i), where i includes all nuclei and nucleons. The nucleons and nuclei together with the photons are coupled by nuclear reactions. If the nuclear reaction timescale is small compared to the macroscopic timescale, these reactions equilibrate. In this case, the number of nuclei and nucleons is not independent anymore and leads to the additional constraint

$$\mu_{A,Z} = (A - Z)\mu_n + Z\mu_p, \tag{3.38}$$

which relates the chemical potential of a nucleus $\mu_{A,Z}$ of mass number A and charge number Z with the chemical potential of neutrons μ_n and protons μ_p. The situation is called nuclear statistical equilibrate (NSE) and is very similar to the ionization and recombination of atoms. As analogy, nuclei are states of matter consisting of protons and neutrons. The corresponding particle numbers

of the nuclei can be derived from a set of equations similar to the Saha equation, see e.g. chapters 14.1 and 36.2.2 in Ref. [67]. When using the EoS as closure for the equations of hydrodynamics, see Sec. 3.1 and 3.1.2, the volume V is arbitrary. In this case, typically all extensive quantities are replaced by corresponding intensive ones (typically mass specific). In the case when NSE holds, a typical choice is (ρ,T,Y_e). These variables are related to the thermodynamic quantities as follows:

$$\rho = m_u n_B = m_u(n_p + n_n), \tag{3.39}$$

$$Y_e = \frac{n_p}{n_B}. \tag{3.40}$$

Note that the proton density n_p and neutron density n_n in the above equations account for nucleons in- and outside nuclei. These variables correspond to the conversion of baryon- and lepton number. Further note that the solution of the hydrodynamics equations is based on solving conversion equations. This does not explicitly include a temperature evolution, but the energy conservation includes the specific internal energy ϵ. The second and third law of thermodynamics imply that the value of specific internal energy strictly increases with temperature. The inverse relation provides the temperature as a function of specific internal energy.

In our simulation domain, temperatures and densities reach from 10^7 - 10^{12} K and 10^0 - 10^{15} g cm^{-3}. Fig. 3.1 shows the combinations of EoS variables which are realized in a CCSN. It shows a clear correlation between density and temperature. The electron fraction is not clearly correlated to the other state variables, but shows that the lowest values are only realized at the highest densities, i.e. inside the PNS.

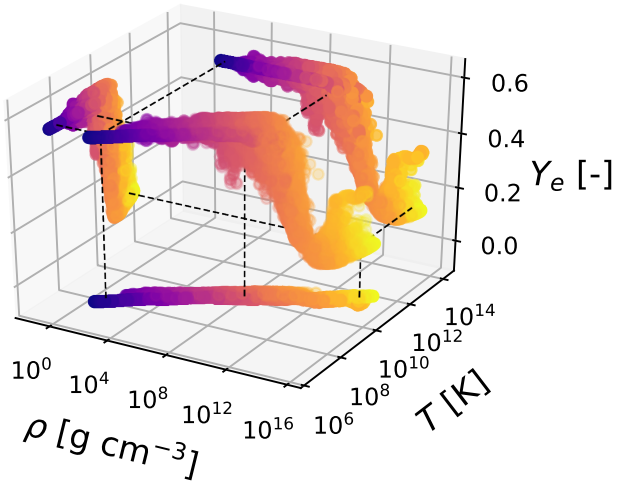

Figure 3.1: Scatter of density, temperature, and electron fraction for various times in a CCSN simulation. The data is taken from a run presented in Ch. 5.1 between few hundred milliseconds before until few seconds post bounce. In all projections, the color indicates the temperature. The dashed lines give an orientation on the projections for three representative points.

3.1.4 Gravitational potential

In context of the stellar environment, the external force field with potential Φ (as described in Eq. 3.3) is the dynamically created gravitational field. In the Newtonian framework, it is given by solving the Poisson equation:

$$\Phi(\mathbf{q}) = -G \int \frac{\rho(\mathbf{q}')}{|\vec{r}(\mathbf{q}) - \vec{r}(\mathbf{q}')|} \, \mathrm{d}\mathbf{q}', \tag{3.41}$$

where G is the gravitational constant and $|\vec{r}(\mathbf{q}) - \vec{r}(\mathbf{q}')|$ is the Euclidian distance between the two points $\mathbf{q}$ and $\mathbf{q}'$. The numerical solution can be derived by summing the multipole expansion of the above equation up to a desired order, i.e.:

$$\Phi(r,\theta,\phi) = \sum_{l=0}^{\infty} \sum_{m=-l}^{l} Q_{lm}(r) \frac{Y_{l,m}(\theta,\phi)}{r^{l+1}} \approx \sum_{l=0}^{l_{\max}} \sum_{m=-l}^{l} Q_{lm}(r) \frac{Y_{l,m}(\theta,\phi)}{r^{l+1}}, \tag{3.42}$$

where $Q_{l,m}$ is the pole, $Y_{l,m}$ are spherical harmonics and (r,θ,ϕ) is the representation of $\mathbf{q}$ in a spherical coordinate system. How the choice of the coordinate center can affect the numerical solution is discussed in Ref. [36].

However, when the iron core of a massive star contracts to a proto-neutron star, the effects of general relativity cannot be neglected. The gravitational potential in general relativity for spherically symmetric stars in gravitational equilibrium has been derived by Oppenheimer & Volkoff [111] based on the work of Tolman (TOV). In order to mimic the effect of general relativity, we replace the Newtonian potential by an effective gravitational potential as described in Ref. [87]

$$\Phi_{\text{eff}} = \Phi - \bar{\Phi} + \bar{\Phi}_{\text{TOV}}, \tag{3.43}$$

where $\bar{\Phi}$ and $\bar{\Phi}_{\text{TOV}}$ are the spherically symmetric Newtonian and TOV potentials, respectively, evaluated on angular averages of the stellar profile. In spherical symmetry, Eq. 3.42 reduces to the mono-pole term ($l = 0$) giving a simple relation for $\bar{\Phi}$. The expression for the TOV potential is more complicated.

$$\bar{\Phi}_{\text{TOV}}(r) = -\frac{4\pi G}{c^2} \int_r^{\infty} \left(\frac{m_{\text{TOV}} c^2}{4\pi} + r'^3 P \right) \left(1 + \frac{P}{\rho c^2 + \epsilon} \right) \frac{1}{\Gamma^2 r'^2} \, \mathrm{d}r' \tag{3.44}$$

$$m_{\text{TOV}}(r) = 4\pi \int_0^r \left(\rho + \frac{e}{c^2} \right) r'^2 \, \mathrm{d}r' \tag{3.45}$$

$$\Gamma = 1 + \frac{|\mathbf{v}|^2}{c^2} - \frac{2G m_{\text{TOV}}}{r c^2} \tag{3.46}$$

The derivation and further information on the TOV potential and the post-Newtonian approximation can be found in e.g. chapter 2.6. of Ref. [67].

3.2 Neutrino transport

3.2.1 Neutrinos

In order to explain how the beta decay conserves energy, momentum and spin, Wolfgang Pauli postulated the existence of a neutral particle involved in these processes in 1930. Its name was introduced by Enrico Fermi who developed

a theory explaining the beta decay. In 1956, the experimental detection of neutrinos was confirmed [40].

Today, neutrinos are part of the standard model of particle physics. They are spin 1/2 fermions of the lepton family. They do only interact via the weak nuclear force. They occur in three flavors corresponding to their associated charged leptons which together with their anti particles lead to six different neutrinos. In the standard model, neutrinos are massless particles. However, the observation of neutrino oscillation indicates that neutrinos are massive particles, but until now the mass could not be determined, see e.g. Ref. [41].

In this work, we will only consider standard model neutrinos.

3.2.2 Neutrino treatment

The transport equation for neutrinos can be derived in a similar way as the hydrodynamics equations from the Boltzmann equation (see eq.3.3). Since the neutrinos interact with the medium, the moment expansion requires a model of the collision term. In contrast to the derivation of the hydrodynamics equations, we start with the general relativistic Boltzmann transport equation derived by Lindquist [83]

$$p^\alpha \left(\frac{\partial f_\nu}{\partial x^\alpha} - \Gamma_\alpha{}^\beta{}_\gamma \, p^\gamma \frac{\partial f_\nu}{\partial p^\beta} \right) = \left(\frac{\partial f_\nu}{\partial \tau} \right)_{\text{coll}}, \tag{3.47}$$

where p and x are the contravariant momentum and position vectors, Γ is a Christoffel symbol, f_ν is the neutrino distribution function and the right hand term is the collision term. Together with the fundamental relation $p_\mu p^\mu = m$, where in our case $m \equiv 0$, the above equation results in a seven dimensional problem for each neutrino species which are coupled by the collision term.

We will derive from this equation the Advanced Spectral Leakage (ASL) [116]. ASL is designed for spherically symmetric simulations or for the use in ray-by-ray schemes. This reduces the dimension of the above equation to the spherically symmetric case and Lindquist in Ref. [83] also gives the corresponding transport equation. The general relativistic setup and the $\mathcal{O}\left(\frac{v}{c}\right)$ expansion are shown in Ref. [79]. The $\mathcal{O}\left(\frac{v}{c}\right)$ expansion of the Boltzmann transport equation is the starting point of the Isotropic Diffusion Approximation (IDSA) [82, 12] and ASL. It is given by

$$\frac{\mathrm{d}f_\nu}{c\mathrm{d}t} + \mu \frac{\partial f_\nu}{\partial r} + \left(A + \frac{1}{r} \right)(1-\mu^2) \frac{\partial f_\nu}{\partial \mu} + \left(\mu A - \frac{v}{cr} \right) E \frac{\partial f_\nu}{\partial E} = j_{\text{em}}(1-f_\nu) - \chi_{\text{ab}} f_\nu + C_{\nu,\text{sc}}, \tag{3.48}$$

where $f_\nu = f_\nu(t, r, \mu, E)$ is the neutrino distribution function which in spherical symmetry depends on the time t, radius r and the momentum phase space decomposed in angle cosine μ and particle energy E. The function A is given by

$$A = \mu \left(\frac{\mathrm{d}\log\rho}{c\mathrm{d}t} + \frac{3v}{cr} \right), \tag{3.49}$$

where ρ is the matter density. Note that the first term implies a Lagrangian time derivative and the partial derivatives are understood to be taken comoving with the fluid element. On the right hand side in Eq. 3.48, we introduce the particle emissivity j_{em}, particle absorptivity χ_{ab}, and the scattering part of the

collision term $C_{\nu,\mathrm{sc}}$. The factor $(1-f_\nu)$ accounts for Pauli blocking in the case of neutrinos and is not present in the case of photons (see e.g. Eq. 20 in Ref. [29]). The Ansatz to solve this equation is a separation of the neutrino distribution function into a trapped and a free streaming component coupled by a source term Σ:

$$f_\nu = f_\nu^t + f_\nu^s, \tag{3.50}$$
$$D(f_\nu^t) = C_\nu^t - \Sigma, \tag{3.51}$$
$$D(f_\nu^s) = C_\nu^s + \Sigma, \tag{3.52}$$

where D is the linear differential operator generating the left side of Eq. 3.48 and assuming that the right hand sight can be split into $C^t + C^s$.

In the core-collapse supernova scenario this separation is motivated by the formation of the dense proto-neutron star (PNS) $\rho \gtrsim 10^{11}\mathrm{g/cm}^3$ and its sharp density gradient which separates it from the surrounding matter $\rho \lesssim 10^8\mathrm{g/cm}^3$. Inside the very dense region, the neutrinos become a fluid constituent (trapped) and outside the PNS, neutrinos can escape with almost no interaction with the surrounding matter (free streaming). Due to the sharp density gradient at the PNS surface, the transition region between the two regimes is expected to be very thin. In order to describe the separation more accurately, we define some characteristic quantities. The emissivity j_{em} corresponds to neutrino production reactions. The leading contributions in core-collapse supernovae are

- Neutrino production in charge current reactions:

$$p + e^- \to n + \nu_e, \tag{3.53}$$
$$(Z, A) + e^- \to (Z-1, A) + \nu_e, \tag{3.54}$$
$$n + e^+ \to p + \bar{\nu}_e. \tag{3.55}$$

- Annihilation neutrinos:

$$e^- + e^+ \to \nu + \bar{\nu}. \tag{3.56}$$

- Bremsstrahlung neutrinos from free nucleons $N \in \{p, n\}$

$$N + N \to N + N + \nu + \bar{\nu}. \tag{3.57}$$

where ν without index can be any flavor chosen for the entire equation. The absorptivity χ_{ab} consists of the inverse reaction rates of the emissivity. The total rate is the sum of the single reaction rates:

$$j_{\mathrm{em}} = \sum_r j_{\mathrm{em},r}, \tag{3.58}$$
$$\chi_{\mathrm{ab}} = \sum_r \chi_{\mathrm{ab},r}, \tag{3.59}$$

where r stands for all reactions and their inverse given by Eqs. 3.53 – 3.57. Furthermore, neutrinos can also interact by scattering. In ASL, we take into account only elastic scattering on nucleons N or nuclei (A, Z):

$$N + \nu \to N + \nu \tag{3.60}$$
$$(A, Z) + \nu \to (A, Z) + \nu. \tag{3.61}$$

The corresponding elastic scattering rates are accounted in

$$\chi_{\mathrm{sc}} = \sum_{s} \chi_{\mathrm{sc},s} \tag{3.62}$$

where s includes all reactions in Eqs. 3.60-3.61. The leading inelastic reactions are given by stimulated emission

$$\chi_{\mathrm{inel}} = \sum_{s'} \chi_{\mathrm{inel},s'} \approx \sqrt{\sum_{r} \chi_{\mathrm{ab},r}\, j_{\mathrm{em},r}}, \tag{3.63}$$

As a next step we introduce the neutrino total and energy mean free path

$$\lambda_{\mathrm{tot}} = \frac{c}{\chi_{\mathrm{sc}} + \chi_{\mathrm{ab}} + j_{\mathrm{em}}}, \tag{3.64}$$

$$\lambda_{\mathrm{en}} = \sqrt{c\frac{\lambda_{\mathrm{tot}}}{\chi_{\mathrm{inel}}}}, \tag{3.65}$$

where the energy mean free path is the geometrical mean between the total mean free path and the mean free path for only inelastic scattering reactions. In contrast to the total mean free path, the energy mean free path sets a higher weight on reactions where neutrinos exchange energy with the fluid. The corresponding optical depth is defined by:

$$\tau_{\mathrm{tot/en}}(E, \mathbf{x}) = \min_{\gamma} \int_{\gamma:\mathbf{x}\to\infty} \frac{1}{\lambda_{\mathrm{tot/en}}(E, \mathbf{x}'(s))}\, \mathrm{d}s. \tag{3.66}$$

Conceptually, the optical depth accumulates the average number of interactions that an escaping particle experiences before leaving the system on the most probable escape path. In general multidimensional cases, special algorithms are required in order to find the escape path γ (e.g. Ref. [117]). However, in the context of a core-collapse supernova, the minimizing path γ can be approximated as the radial path from the star's gravitational center to infinity. Note, that by definition $\tau_{\mathrm{en}} \leqslant \tau_{\mathrm{tot}}$, which gives rise to the definition of four regimes.

1. $\tau_{\mathrm{tot}} \gg 1$ and $\tau_{\mathrm{en}} \gtrsim 1$, the *equilibrium-diffusive* regime. At this condition, the neutrinos are in thermal equilibrium with the fluid and can be treated as additional constituent of the fluid. In the following, we will refer neutrinos in this regime as *trapped*.

2. $\tau_{\mathrm{tot}} \sim 1$ and $\tau_{\mathrm{en}} \lesssim 1$, the *diffusive* regime. Neutrinos are still interacting frequently with matter, but not necessarily in thermal equilibrium. The neutrino mean free path is large compared to typical system lengths. Thus, neutrinos are not bound tightly to matter which corresponds to diffusive propagation.

3. $\tau_{\mathrm{tot}} \sim 1$, the *semitransparent* regime. This regime describes the transition between interacting neutrinos and almost non-interacting (free) neutrinos. The propagation is neither dominated by diffusion, nor are neutrinos streaming only in one direction without been scattered. The surfaces where $\tau = 2/3$ define the so called neutrino surfaces $R_\nu(E)$ (or neutrino spheres, in the case of spherical symmetry). For τ_{tot}, these surfaces describe the region of last interaction before the neutrino of a given flavor and energy streams through transparent matter. For τ_{en}, these surfaces are the location where neutrinos decouple thermally from matter.

4. $\tau_{\rm en} \lesssim 1$, the *free-streaming* regime. In this regime, the surrounding matter appears transparent to neutrinos. Neutrinos propagating through this region can stream freely, almost without any matter interaction. However, if the neutrino flux is large, a small fraction of reabsorption may still contain a significant amount of energy relevant for the neutrino explosion mechanism in core-collapse supernovae.

Trapped component: Following IDSA [82], also in ASL, we assume isotropic distribution functions $f_\nu^t = f_\nu^t(t, r, E)$, but we do not directly model the source function Σ for the trapped component. Instead, we mimic Σ with timescale arguments as shown below in Eq. (3.73). For the trapped particles, we assume that these are almost in thermal equilibrium with the matter, which allows for a local reconstruction of f_ν^t from local quantities as presented in eq.(3.76). In order to couple the trapped component to the hydrodynamics equation, we introduce the following quantities referring to the local number and energy density of trapped neutrinos:

$$Y_\nu(t, r) = \frac{4\pi}{(hc)^3} \frac{m_u}{\rho} \int f_\nu^t E^2 \, \mathrm{d}E \tag{3.67}$$

$$Z_\nu(t, r) = \frac{4\pi}{(hc)^3} \frac{m_u}{\rho} \int f_\nu^t E^3 \, \mathrm{d}E, \tag{3.68}$$

which correspond to the following conservation equations

$$\frac{\partial(\rho Y_\nu)}{\partial t} + \nabla_q \cdot (\rho Y_\nu \mathbf{v}) = \rho \dot{Y}_\nu \tag{3.69}$$

$$\frac{\partial(\rho Z_\nu)^{3/4}}{\partial t} + \nabla_q \cdot ((\rho Z_\nu)^{3/4} \mathbf{v}) = \frac{3}{4} Z_\nu \rho^{3/4} \frac{\dot{Z}_\nu}{Z_\nu}. \tag{3.70}$$

Eqs. 3.69 and 3.70 are also valid in the multidimensional case and therefore, we write the equation for generalized coordinates q. In contrast to IDSA, ASL does not solve the diffusion limit as described in the appendix of Ref. [82] in order to get $\dot{Y}_\nu$ and $\dot{Z}_\nu$. As mentioned before, these source terms are determined by time scale arguments. The distribution function of trapped neutrinos in the comoving frame changes due to neutrino production and diffusion, i.e.

$$\frac{\mathrm{d}f_\nu^t}{\mathrm{d}t} = \dot{f}_{\nu,\rm prod}^t + \dot{f}_{\nu,\rm diff}^t, \tag{3.71}$$

where the production tends to establish the thermal equilibrium distribution and the diffusion accounts for migration of neutrinos beyond advection due to large mean free paths. The expressions are

$$\dot{f}_{\nu,\rm prod}^t = \frac{(f_\nu)_{\rm eq} - f_\nu^t}{\max(t_{\nu,\rm prod}, \Delta t)} \exp\left(- \frac{t_{\nu,\rm prod}}{t_{\nu,\rm diff}} \right), \tag{3.72}$$

$$\dot{f}_{\nu,\rm diff}^t = - \frac{f_\nu^t}{\max(t_{\nu,\rm diff}, \Delta t)} \exp\left(- \frac{t_{\nu,\rm diff}}{t_{\nu,\rm prod}} \right), \tag{3.73}$$

where the equilibrium distribution $(f_\nu)_{\rm eq}$ is given by the Fermi-Dirac distribution function

$$(f_\nu)_{\rm eq} = \frac{1}{\exp\big((E - \mu_\nu)/T_\nu\big) + 1}, \tag{3.74}$$

assuming the neutrino temperature T_ν to be equal to the matter temperature and a weak equilibrium which determines the neutrino chemical potential

$$\mu_{\nu_e} = \mu_e - \mu_n + \mu_p = -\mu_{\bar{\nu}_e}. \tag{3.75}$$

Here, μ_e, μ_n and μ_p are the relativistic chemical potentials of electrons, neutrons, and protons, respectively. The sum of the chemical potentials of the other neutrino flavors equals to zero, because by construction we treat these neutrinos and their anti-particles equally. The trapped component is related to Y_ν via Eq. 3.67 and is reconstructed by:

$$f_\nu^t = \gamma (f_\nu)_{\rm eq}(1 - \exp(-\tau_{\rm en})), \tag{3.76}$$

where γ is the normalization factor set by equation 3.67[2].
The timescales are given by:

$$t_{\nu,\rm prod} = (j_\nu)^{-1} \tag{3.77}$$

$$t_{\nu,\rm diff} = \frac{\alpha_{\rm diff}\ \tau_{\nu,\rm tot}\ \lambda_{\nu,\rm tot}}{c} \tau_{\nu \rm tot}, \tag{3.78}$$

where $\alpha_{\rm diff}$ is a parameter which allows for control of the diffusion rate. It has a typically value of $\alpha_{\rm diff} \sim 3$ according to Ref. [116].

Free streaming component: The free streaming component is evaluated along a ray from the center. This component keeps its spectral information and accounts for the emission of neutrinos along the radial direction. We follow Ref. [82] in order to reduce Eq. 3.48 to

$$\frac{\partial \hat{f}_\nu^s}{c\partial \hat{t}} + \hat{\mu}\frac{\partial \hat{f}_\nu^s}{\partial r} + \frac{1}{r}(1-\hat{\mu}^2)\frac{\partial \hat{f}_\nu^s}{\partial \hat{\mu}} = -(\hat{j} + \hat{\chi})\hat{f}_\nu^s + \hat{\Sigma}, \tag{3.79}$$

where the hat denotes an evaluation in the lab frame. Instead of following IDSA, ASL also applies timescale arguments, such as Eqs. 3.72 and 3.73, for the evolution of the free streaming component. In the following, we consider all calculations in the lab frame.

The quantities of interest is the source terms coupling to the hydro. We define the emission rate R_ν^k and the absorption rate H_ν^k with $k \in \{0, 1\}$, where $k = 0$ means coupling to the lepton number and $k = 1$ coupling to the energy. The corresponding lepton number and energy source terms are

$$\dot{Y}_l = -m_u(R^0_{\nu_e} - R^0_{\bar{\nu}_e} - H^0_{\nu_e} + H^0_{\bar{\nu}_e}), \tag{3.80}$$

$$\dot{u} = -(R^1_{\nu_e} + R^1_{\bar{\nu}_e} + 4R^1_{\nu_{\mu,\tau}}) + (H^1_{\nu_e} + H^1_{\bar{\nu}_e}). \tag{3.81}$$

These rates depend on their associated spectral rates r_ν and h_ν via[3]

$$R_\nu^k = \int_0^\infty r_\nu E^{2+k}\, {\rm d}E, \tag{3.82}$$

$$H_\nu^k = \int_0^\infty h_\nu E^{2+k}\, {\rm d}E. \tag{3.83}$$

[2]Note, that this choice is arbitrary. We could use Eq. 3.68 as well.

[3]Note that the sum of the spectral rates $(r_\nu + h_\nu)$ is closely related to the right hand side of Eq. 3.79, but Eq. 3.79 still dependence on the angle cosine μ.

Furthermore, we split the spectral emission rate into a production and diffusion part. The production rate stays associated with j_ν and the spectral rate is given by

$$r_{\nu,\mathrm{prod}} = \frac{4\pi}{(hc)^3}\frac{j_\nu}{\rho} \tag{3.84}$$

and the diffusion rate is

$$r_{\nu,\mathrm{diff}} = \frac{4\pi}{(hc)^3}\frac{1}{\rho}\frac{(f_\nu)_{\mathrm{eq}}}{t_{\nu,\mathrm{diff}}}. \tag{3.85}$$

The production rate is dominant in optically thin conditions and the diffusion rate in opaque regions. The combined spectral emission rate r_ν is given by a smooth interpolation between both regimes.

$$r_\nu = (1-\alpha_{\mathrm{blk}})\,\tilde{r}\,\mathcal{N}_\nu \exp(-\tau_{\nu,\mathrm{en}}/\tau_{\mathrm{cut}}), \tag{3.86}$$

where

$$\tilde{r}_\nu = \frac{r_{\nu,\mathrm{prod}} r_{\nu,\mathrm{diff}}}{r_{\nu,\mathrm{prod}} + r_{\nu,\mathrm{diff}}}, \tag{3.87}$$

is the harmonic mean of the spectral production and diffusion rates and

$$\mathcal{N}_\nu = \frac{\int_0^\infty \tilde{r}_\nu E^2\,\mathrm{d}E}{\int_0^\infty \tilde{r}_\nu \exp(-\tau_{\nu,\mathrm{en}}/\tau_{\mathrm{cut}})E^2\,\mathrm{d}E} \tag{3.88}$$

is a normalization factor. The parameters α_{blk} and τ_{cut} are specific to ASL. According to Ref. [116], reasonable values of these parameters are $\alpha_{\mathrm{blk}} \sim 0.5$ and $\tau_{\mathrm{cut}} \sim 10$. The parameter α_{blk} controls the neutrino luminosity and therewith the neutrino heating. The location where the free streaming component builds up is controlled by τ_{cut}.

The re-absorption of emitted neutrinos along a ray is given by the spectral absorption rate h_ν. The spectral absorption rate is based on the luminosity integration

$$\frac{\mathrm{d}l_\nu}{\mathrm{d}r} = 4\pi r^2 \rho r_\nu - \frac{\chi}{c}\mathcal{H} l_\nu, \tag{3.89}$$

where $\mathcal{H} = \exp(-\tau_{\nu,\mathrm{tot}})$ is an exponential cutoff to ensure an integration only of the free streaming component and the luminosity is related to the free streaming distribution function via the free streaming spectral neutrino density n_ν^s

$$n_\nu^s \equiv \frac{4\pi}{(hc)^3} f_\nu^s = \frac{l_\nu}{4\pi r^2 c \bar{\mu}_\nu}, \tag{3.90}$$

where $\bar{\mu}_\nu$ is the spectral neutrino flux factor which is approximated by

$$\bar{\mu}_\nu(E) = \frac{1}{2}\left(1 + \sqrt{1 - \left(\frac{R_\nu(E)}{\max(r, R_\nu(E))}\right)^2}\right), \tag{3.91}$$

where $R_\nu(E)$ is the energy dependent neutrino sphere, see Ref. [82]. The spectral absorption rate is then given by

$$h_\nu = \frac{1}{\rho} n_\nu^s\, \chi_{\mathrm{ab}} \mathcal{F}\, \mathcal{H}, \tag{3.92}$$

where $\mathcal{F}$ is the Pauli blocking factor for electrons and positrons in the final state

$$\mathcal{F}_{e^{\mp}} = \left(1 - \frac{1}{\exp((e \pm Q \mp \mu_e)/T) + 1}\right). \tag{3.93}$$

Eq. 3.89 can be derived from Eq. 3.79 assuming a static background field of neutrinos, integrating the angle cosine μ, and neglecting the diffusion part of Σ (see first term of Eq. 6 in Ref. [82]). The diffusion part is handled by the timescale argument in r_ν, but the relevant region for the application of this approximation is in optically thin regions. The final source terms coupling to the hydrodynamics are given by:

$$\dot{Y}_e = \dot{Y}_l - \dot{Y}_{\nu_e} + \dot{Y}_{\bar{\nu}_e} \tag{3.94}$$

$$\dot{\epsilon} = \dot{u} - \frac{1}{m_u}(\dot{Z}_{\nu_e} + \dot{Z}_{\bar{\nu}_e} + 4\dot{Z}_{\nu_{\mu,\tau}}) \tag{3.95}$$

In Sec. 4.2.3, we will introduce the leading general relativistic corrections on the free streaming neutrino density, see eq.3.90. However, the implementation of these corrections is an extension of ASL, and specific to the study made in Ch. 4. It does not correspond to the original ASL presented in Ref. [116].

3.3 Numerical Setup

In this section, we present the numerical framework which we use in order to follow the stellar center from core-collapse until several seconds after core bounce. In sec.3.3.1, we introduce the FLASH[4] code and the setup that we use to simulate core-collapse supernovae, followed by sec.3.3.2, where we give more details on the implementation of ASL in FLASH.

3.3.1 The FLASH code

We use FLASH version 4 in order to solve the equations of hydrodynamics (Eqs. 3.14, 3.17, 3.18). FLASH [48, 43] is a publicly available multiphysics multiscale simulation code developed and administrated by the Flash Center for computational science at the University of Chicago. The simulation setup, used in this thesis, is based on the previous work by Sean Couch, Evan O'Connor [34, 33, 37, 107], and Kuo-Chuan Pan [114]. The setup includes the use of an adaptive mesh refinement (AMR) which puts higher resolution on demand, PARAMESH, [86]. In our setup, the refinement is based on the gradients of density, pressure, and entropy. Fig 3.2 shows the AMR acting in a cylindrically symmetric CCSN simulation. In the background, we see the contours of the entropy gradient. Clearly visible is the additional radial constraint on the maximum refinement level, which leads to the radial distribution of blocks with step wise increasing size from the center up to about 200 km in radial direction. The AMR block structure above 200 km is also influenced by the gradient criteria. As a consequence the refinement level at the shock front is set to the maximum allowed by the radial criterion. Furthermore, we use the optimized unsplit hydrodynamics solver [75, 74], which solves conservation equations using a finite volume method. The face fluxes are reconstructed using the third-order

[4] `http://flash.uchicago.edu`

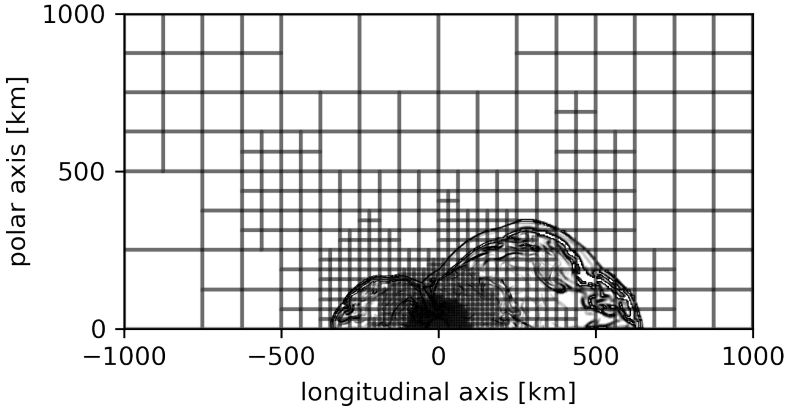

Figure 3.2: AMR example in a cylindrically symmetric CCSN simulation. The background shows the contours of the entropy gradient as one representative indicator for the refinement. The entropy gradient also reveals the shock position.

piecewise parabolic method (PPM) [31] and using a hybrid slope limiter [10] in order to avoid numerical flux oscillations and ensure a more stable solution. The time evolution is performed by applying a hybrid approximate Riemann solver, which uses the HLLC solver on smooth flows and the more diffusive HLLE near discontinuous flows (shocks) in order to prevent numerical shock instabilities (see e.g. Refs. [121, 130]). In cases where we simulate on an extended domain ($R_{\max} \gtrsim 20,000$ km), the numerical treatment of the equation of state is divided into two density regions. The boundary is set to $\sim 10^6$ g cm^{-3}, where the nuclear contribution $F_{\rm nuc}$ is negligible and NSE is not established. The dominant contribution comes from degenerate electrons. As discussed in sec.3.1.3, the electron contribution requires the calculation of Fermi integrals. In the numerical setup, solving Fermi integrals for each equation of state call is not suitable. In our simulation, the electron-positron free energy is tabulated as described in Refs. [139, 140]. The other constituents are calculated based on their analytical formula. The Coulomb corrections are calculated according to Ref. [151]. At the high density regime, we assume NSE. The contribution of free nucleons is also not given by an analytical formula. Here and in case of a reduced domain ($R_{\max} \lesssim 20,000$ km), we use a tabulated EoS containing all contributions.

Note, that due to different conventions for the low/high density EoS in a numerical setup (e.g. table spacing, internal energy including/excluding binding energy, chemical potentials including/excluding rest mass, etc.), a thermodynamically consistent transition from one treatment to the other may not be straight forward. One approximate, but numerically stable way can be achieved by an interpolation between the two regimes[5].

The gravitational potential is calculated using the new multipole solver for self gravity [36]. The Advanced Special Leakage (ASL) [116], was implemented to FLASH as part of this thesis.

[5]Thanks to Hannah Yasin for this practical approach.

3.3.2 ASL in FLASH

The development of ASL in FLASH was a major part of this thesis. The advection of the trapped neutrino components (Eqs. 3.69, 3.70) is handled by the hydrodynamics solver. The local neutrino source terms (Eqs. 3.94,3.95) are coupled to the hydrodynamics in an operator splitting approach, see e.g. chapter 5 in Ref. [77]. The optical depths (Eq. 3.66) and the spectral neutrino density (Eqs. 3.90,3.89) require an integration in radial direction. We calculate these values in a ray-by-ray approach which is based on the existing *NeutrinoLeakage* module [108, 37] available in FLASH. The rays are equally distributed on angular bins. Each ray consists of equally spaced radial bins up to a certain radius and it continues logarithmically spaced to the maximum ray radius. The user specifies the number of radial and angular bins, the maximum radius, the central spacing, and the radius where the log-spacing begins.

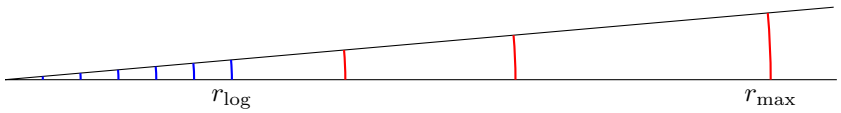

Figure 3.3: Schematic structure of the rays. The inner spacing (blue) is linear. Beginning from the radial position $r_{\log}$, the spacing (red) continues logarithmically up to the maximum ray radius $r_{\max}$.

In the current implementation, the spectral information is descretized in either 12 or 20 energy groups which are logarithmically spaced between 3 to 300 MeV. This requires more data per ray compared to a gray scheme. Hence, the MPI communication model has been refactored which improves the code performance/scaling, especially in full 3D simulations. The neutrino input physics includes neutrino emission and absorption on free nucleons and nuclei [20], neutrino scattering off nucleons and nuclei in the elastic approximation [20], electron-positron annihilation [94], and nucleon-nucleon Bremsstrahlung [54].

In order to study longtime simulations with various explosion energies, we introduced a heating parameter f_{heat} which modifies Eq. 3.81 to

$$\dot{u} = -(R^1_{\nu_e} + R^1_{\bar{\nu}_e} + 4R^1_{\nu_{\mu,\tau}}) + f_{\text{heat}}(H^1_{\nu_e} + H^1_{\bar{\nu}_e}). \tag{3.96}$$

Using f_{heat} only in the energy source term ensures, that the electron fraction is not directly affected.

Chapter 4

Neutrino Schemes in FLASH

ASL has been implemented as part of this thesis, see Sec. 3.2. During the code development, we tested our implementation against `AGILE-ASL` [81, 116]. In the context of this thesis, the first benchmark of our implementation of the ASL is a comparison to the other spectral neutrino transport methods available in `FLASH`, i.e. IDSA [114] and M1 [110]. The chapter is based on the publication by Pan, Mattes, O'Connor, Perego, Couch, and Arcones, see Ref. [115]. The purpose of this study is to understand the impact of different neutrino transport methods on multidimensional core-collapse supernova simulations.

Neutrinos play a crucial role in the core-collapse supernova (CCSN) explosion mechanism. The requirement of accurately calculating the transport of neutrinos makes simulations of the CCSN mechanism extremely challenging and computationally expensive. Historically, this stiff challenge has been met by making approximations to the full transport equation. In this work, we compare CCSN simulations in one- and two-dimensions with three approximate neutrino transport schemes, each implemented in the `FLASH` simulation framework. We compare a two moment M1 scheme with an analytic closure (M1), the Isotropic Diffusion Source Approximation (IDSA), and the Advanced Spectral Leakage (ASL) method. We identify and discuss the advantages and disadvantages of each scheme. For each approximate transport scheme, we use identical grid setups, hydrodynamics, and gravity solvers to investigate the transport effects on supernova shock dynamics and neutrino quantities. We find that the transport scheme has a small effect on the evolution of protoneutron star (PNS) radius, PNS mass, and the mass accretion rate. The neutrino luminosities, mean energies, and shock radii have a $\sim$ 10-20% quantitative difference but the overall qualitative trends are fairly consistent between all three approximations. We find larger differences in the gain region properties, including the gain region mass and the net heating rate in the gain region, as well as the strength of PNS convection in the core. We investigate the progenitor, nuclear equation of state, and stochastic perturbation dependence of our simulations and find similar magnitudes of impact on key quantities. We also compare the computational expense of the various approximations.

4.1 Introduction

Simulations of the core-collapse supernova (CCSN) mechanism require a challenging array of input physics, including multidimensional magnetohydrodynamics, detailed neutrino transport, involved microphysics, and general relativistic gravity. Over the roughly six-decade history of computational investigation of the CCSN mechanism, this complex mix of input physics has put this problem at the cutting-edge of computational complexity and expense. Dominating the difficulty is the requirement to accurately simulate the transport of neutrinos in this complex context. The transport of neutrinos must be followed from the diffusive, optically thick protoneutron star (PNS), through the semi-transparent region between the PNS and the stalled supernova shock, and into the completely transparent, free-streaming region beyond the shock. Solving the full seven-dimensional Boltzmann transport equation for neutrinos is almost universally too steep a challenge for high-resolution, time-dependent CCSN simulations (but see [105]). Approximating the full transport equation is common, though different groups working on the problem apply various different approaches.

Despite the challenge of CCSN mechanism simulations, tremendous progress has been made in recent years. After decades of research marked by cycles of promise then failure, several groups are now reporting successful neutrino-driven explosions in 2D [88, 102, 21, 26, 133, 122, 110, 131, 142]. These results often show significant quantitative, and even qualitative, differences for similar initial conditions. These various works use a variety of different hydrodynamic and neutrino transport approaches, making a direct code-to-code verification impossible. Here, we present a controlled code-to-code verification of different neutrino transport approximations commonly used in multidimensional simulations of the CCSN mechanism. We compare the two-moment explicit "M1" closure method [107], the isotropic diffusion source approximation (IDSA) [82], and the advanced spectral leakage (ASL) method [117], using the same simulation framework, FLASH [48, 43].

In this study, we restrict ourselves to 1D and 2D simulations. While current high-fidelity simulations in 1D only result in explosions for very low-mass iron core progenitors [68], it has long been understood that multidimensional effects in 2D, such as neutrino-driven convection and the standing accretion shock instability (SASI), aid shock expansion and explosion [24]. In recent years, it has become clear that fully 3D simulations are necessary as the enforced symmetry of 2D is unduly influencing the quantitative outcomes of CCSN simulations [33, 53, 76, 89, 90].

While a controlled comparison in 3D is desirable, there is yet no detailed code comparison of CCSN simulation in even 2D (although see the recent work of [64, 28]). The careful comparison of 1D, high-fidelity CCSN simulation codes executed by [80] is extremely valuable, and even led to improvements in the approach for approximating general relativistic gravity now widely used [87]. Multidimensional comparisons are challenging because of the non-linear feedback between the hydrodynamics, transport, and gravity. The development of non-linear instabilities in 2D and 3D can make it a challenge to disentangle what differences in the underlying numerical methods are leading to differences in the results. Here, we attempt to address this difficulty by carrying out 1D and 2D comparisons of different neutrino transport approximations using *iden-*

tical hydrodynamics, gravity solvers, EoS implementations, and computational grids. Non-linear feedback and instabilities can still magnify small differences, but using a common code for everything except neutrino transport allows us the most controlled study of the impacts of different transport methods on the overall results of CCSN simulations. This approach can shed light on the magnitude of the impact of different transport approximations in multidimensional simulations and their relative computational expense.

Our presentation of this study is as follows. In Section 4.2, we describe our numerical methods, including the details of the three different transport approximations we employ. In Section 4.3, we present our results, starting with a comparison of 1D simulations then continuing on to discuss 2D simulations. We also briefly explore the impact of different equations of state (EoS) and contrast this with the differences arising from different transport schemes. Additionally, in Section 4.3, we discuss the difference in overall code performance for the different approaches. We conclude in Section 4.4.

4.2 Methods

4.2.1 Hydrodynamics and gravity

We use the `FLASH` setup as described in Sec. 3.3.1 using the effective GR potential as also used in [110]. We place the outer boundary of the domain at 10^4 km and employ 9 levels of refinement. We use 5 base AMR blocks in the radial dimension for both the 1D and 2D simulations, and 10 base AMR blocks along the cylindrical direction in 2D. Each AMR block contains 16 zones per dimension, giving a smallest zone width of $\sim$0.488 km. To save computation time, we reduce the maximum AMR level based on the distance from the center of the proto-neutron star (PNS), enforcing an effective angular resolution of $< 0^\circ.53$. We use a radial power law profile for density and velocity as outer boundary conditions to approximate the stellar envelope rather than a pure outflow boundary condition which overestimates the mass accretion flow and can affect the shock evolution at late times [34].

4.2.2 Progenitor and nuclear equation of state

We carry out our comparison using two progenitor models from [148] with zero-age main sequence masses of 15 and 20 $M_\odot$ (hereafter "s15" and "s20"). The structures of these two progenitor models are quite different. The s20 progenitor model has a larger and denser silicon shell compared to the s15 model, whose density declines much faster with radius in this region. This leads initially to a larger mass accretion rate onto the PNS after bounce in s20 when compared to s15. At the silicon-oxygen interface, the s20 model has a very strong density gradient which gives a marked drop in the mass accretion rate around $\sim$200 ms after bounce. Such a sharp density drop is absent in s15, further distinguishing these models. Finally, after the accretion of the silicon-oxygen interface the density structure in s20 is such that the mass accretion rate remains fairly constant, but in s15 the mass accretion rate continues to slowly decrease.

We use the Steiner, Fischer, & Hempel (SFHo) EoS, which is tuned to fit, among other parameters, neutron star (NS) radius observations [132]. We con-

sider two additional EoS: the Lattimer & Swesty EoS (with incompressibility $K = 220$ MeV, LS220) [72], and the Hempel & Schaffner-Bielich (HS) EoS with the DD2 parameterization, HS(DD2) [47]. Gauging the impact of different EoS gives us a point of comparison for interpreting the magnitude of the effect of different transport approximations. Variants of the Lattimer & Swesty EoS have been widely used in the CCSN simulation community since they first became available almost 30 years ago. The LS220 EoS does not, however fulfill certain theoretical and experimental nuclear physics constraints (see, e.g., [57, 70]). The HS(DD2) EoS, on the other hand, shows good agreement with nuclear experiment about cluster formation properties [47], but predicts larger NS radii than SFHo. All three EoS have a maximum gravitational mass greater than $2\,M_\odot$, as required by observations [42].

4.2.3 Neutrino transport

We compare three different neutrino transport implementations using the same hydrodynamics, gravity, and EoS, described above. We use the two-moment explicit "M1" closure method [107], the isotropic diffusion source approximation (IDSA) scheme [82], and the advanced spectral leakage (ASL) method [117]. In this section, we briefly described each method and highlight salient points of each relevant to our comparison effort.

M1

Our M1 neutrino transport scheme is a multidimensional, three-species, energy-dependent, approximation to Boltzmann neutrino transport. Instead of evolving the entire angle-dependent distribution function, we only evolve the first two angular moments. This is similar to the derivation of the equations of hydrodynamics, see Eq. 3.7, but without integrating the energy dependence, because we cannot assume LTE for the neutrinos. The zeroth angular moment, $\mathcal{J}$, represents the energy density of neutrinos within an energy bin, while the first moment, $\mathcal{H}^i$, represents the momentum density of neutrinos within an energy bin. We follow the formulation of [128, 107, 110], i.e. we closes the system of equations assuming the M1 closure for the second moment (Eddington tensor), $\mathcal{K}^{i,j}$. In the optically thick regime, neutrinos propagate isotropically, which leads to an Eddington tensor of the form:

$$\mathcal{K}^{i,j}_{\text{thick}} = \frac{J}{3} h^{i,j}, \tag{4.1}$$

where $h^{i,j} = 1 + W^2 v^i v^j$ is the projection tensor including the Lorentz factor W and the fluid velocity components v^i. In the optically thin regime, we take the free streaming limit of the Eddington tensor:

$$\mathcal{K}^{i,j}_{\text{thin}} = \mathcal{J} \frac{\mathcal{H}^i \mathcal{H}^j}{\mathcal{H}^2}. \tag{4.2}$$

The total Eddington tensor results from a smooth interpolation between this regimes, constructed as

$$\mathcal{K}^{i,j} = \frac{3(1-\chi)}{2} \mathcal{K}^{i,j}_{\text{thick}} + \frac{3\chi - 1}{2} \mathcal{K}^{i,j}_{\text{thin}}, \tag{4.3}$$

where χ is an interpolation factor, which asymptotes to 1/3 (giving $\mathcal{K}^{i,j} = \mathcal{K}^{i,j}_{\rm thick}$) in the optically thick limit, and approaches 1 (giving $\mathcal{K}^{i,j} = \mathcal{K}^{i,j}_{\rm thin}$) in the free streaming limit. Following Ref. [96], we insert the interpolation factor

$$\chi = \frac{1}{3} + \frac{2}{15}(3\phi^2 - \phi^3 + 3\phi^4), \tag{4.4}$$

where $\phi = \sqrt{\mathcal{H}^2/\mathcal{J}^2}$ is the flux factor (compare to Eq. 3.91). The shown Eddington tensor is derived in the Fluid rest frame and still needs to be transformed to the laboratory frame.

We simulate 12 energy groups, logarithmically spaced between 1 MeV and 275 MeV. We use opacities from `NuLib` [107]. Briefly, these include elastic scattering on nuclei and nucleons; charged current absorption of electron type neutrinos and anti-neutrinos on nucleons and electron type neutrinos on heavy nuclei; and thermal emission of heavy-lepton neutrinos and anti-neutrinos from electron-positron annihilation and nucleon-nucleon Bremsstrahlung. These opacities and attendant corrections, including ion-ion correlations and the heavy nucleus form factor, are based on [20, 25]. We neglect weak magnetism corrections in order to more closely match the opacity sets used in IDSA and ASL.

The neutrino moment equations are solved using standard techniques borrowed from hydrodynamics. In regions of low optical depth, the evolution equations are hyperbolic and the spatial flux between grid zones is determined using a Riemann solver. In the high optical depth limit, where the optical depth of a grid zone is greater than 1, we transition the flux determination from the Riemann solution to the asymptotic diffusion limit fluxes. We calculate the energy space fluxes (due to gravitational red shift and velocity gradients) explicitly. The neutrino-matter interaction source terms are treated implicitly, see appendix B of Ref. [110].

IDSA

A detailed description of IDSA is provided in [82] and [114] Here, we briefly review the approach reiterating the equations relevant for the present comparison. In IDSA, the distribution function f of transported neutrinos is decomposed into a free-streaming component f^s and a trapped component f^t. These two components are evolved separately and linked by a diffusion source term Σ, see Eq. 3.50. The diffusion source term is expressed as

$$\Sigma = \min\left\{\max\left[\alpha + (j+\chi)\frac{1}{2}\int f^s d\mu, 0\right], j\right\}, \tag{4.5}$$

where

$$\alpha = \nabla\cdot\left(\frac{-1}{3(j+\chi+\phi)}\nabla f^t\right), \tag{4.6}$$

is a non-local diffusion scalar, j the emissivity, χ the absorptivity, ϕ the scattering opacity, and μ the cosine of the angle between the neutrino propagation and the radial direction. The trapped neutrino distribution f^t is evaluated using Equation 4.5, 4.6 and the transport equation

$$\frac{\partial f^t}{c\,\partial t} = j - (j+\chi)f^t - \Sigma, \tag{4.7}$$

assuming the spectral shape of the trapped component to be described by a Fermi distribution function. The diffusion scalar α is solved by an explicit diffusion solver. Once f^t is determined, the net interaction rates $\mathcal{S}$ can be evaluated by

$$\mathcal{S} = \frac{\partial f^t}{c\partial t} + \Sigma - (j+\chi)\frac{1}{2}\int f^s d\mu, \tag{4.8}$$

and hydrodynamics quantities are updated by:

$$\frac{\partial Y_e}{c\partial t} = -\frac{m_b}{\rho}\frac{4\pi c}{(hc)^3}\int \left(\mathcal{S}_{\nu_e} - \mathcal{S}_{\bar{\nu}_e}\right) E^2 dE, \tag{4.9}$$

$$\frac{\partial e}{c\partial t} = -\frac{m_b}{\rho}\frac{4\pi c}{(hc)^3}\int \left(\mathcal{S}_{\nu_e} + \mathcal{S}_{\bar{\nu}_e}\right) E^3 dE - Q_x, \tag{4.10}$$

where ρ is the matter density, m_b the baryon mass and h the Planck constant. Q_x is the cooling provided by μ and τ neutrinos which is modeled by a grey leakage scheme [54, 125]. In our current IDSA solver, we only consider the transport of electron flavor neutrinos and anti-neutrinos. The streaming neutrino distribution f^s and streaming neutrino flux for the next step can be calculated from the neutrino net interaction rates and the streaming transport equation. To couple the trapped neutrino component with matter, IDSA uses the same definition for neutrino fraction Y_ν^t and neutrino energy density Z_ν^t, see eqs. 3.67 and 3.68. These contributions have been showen to be crucial in CCSN simulations by [93]. Note that the current IDSA solver does not include any GR corrections to the transport equations.

The IDSA solver was first implemented in 1D coupled to the `AGILE` hydrodynamics code [82] and compared with the `AGILE-BOLTZTRAN` code [78] in the Newtonian limit. The latter solves the full Boltzmann transport equation. Good agreement of neutrino fluxes and spectra between IDSA and full Boltzmann transport was found in [82], but IDSA leads to a slightly larger maximum shock radius (∼10-20%) and a faster shock contraction.

To extend the IDSA solver to multiple dimensions, one could either solve for the diffusion scalar α in multiple dimensions, but keep the streaming component isotropic [114], or implement the IDSA with a 'ray-by-ray plus' approach [135, 137]. In the latter case, the domain is decomposed in several radial directions, along which the transport problem is solved separately as in spherical symmetry, but neutrino quantities can be still advected in multiple dimensions. In this paper, we implement the IDSA solver in `FLASH` with the former approach, keeping the diffusion scalar in multi-D but solving the streaming component isotropically. 12 energy bins that are logarithmically spaced from 3 to 200 MeV are used in the IDSA solver. We use neutrino rates for the emission, absorption, and scattering of neutrinos off neutrons, protons and nuclei from [20] and nucleon-nucleon Bremsstrahlung from [54].

ASL

The Advanced Spectral Leakage (ASL) method [116, 117] is a three-species approximate neutrino treatment designed to model neutrinos in the context of core-collapse supernovae and compact binary mergers. It is based on previous gray leakage schemes [126, 125, 108], but in addition it carries spectral information on discretized neutrino energies and models trapped neutrino components.

A detailed description of ASL is given in Sec. 3.2. ASL has been implemented in several hydrodynamics codes, both Eulerian and Lagrangian, including `AGILE` [81] in spherically symmetry, FISH [66] and SPHYNX [27] in 3D.

For this study, we use ASl with 12 energy groups. The ray-grid consists of 1000 radial zones, linearly spaced up to 150 km and logarithmically spaced up to 3000 km, and additionally in 2D 37 uniform angular zones providing a resolution of 4°.9. The implementation presented in Sec. 3.2 which follows Ref. [116] is purely Newtonian. The usage of ASL in relativistic simulations or in simulations employing an effective GR gravitational potential requires the introduction of the most important relativistic corrections also in the neutrino propagation. In fact, the ASL results presented in this comparative study are qualitatively different for pure Newtonian ASL models. In the latter cases, shock revivals are observed soon after 230ms post bounce, at the occurrence of the progenitor shell interface, in 2D cylindrically symmetric models. These explosions are robust with respect to variations in the ASL free parameters and relate to systematically larger (∼20%) neutrino mean energies that significantly enhance the heat deposition inside the gain region. A similar effect is observed also in 1D, however the increased heating rate is not strong enough to drive an explosion in more pessimistic spherically symmetric models.

Here, we present the extension of ASL that we have adopted in this comparative study, which includes the gravitational redshift and the Lorentz boost between the fluid and grid reference frames. They affect radiation propagation in optically thin conditions and its absorption by the moving fluid. Since in this work we perform 1D spherically symmetric simulations and, for the 2D cylindrically symmetric models, we adopt a ray-by-ray approach for the propagation of the free streaming neutrinos, we present the relativistic extension for spherically symmetric models.

We assume a radial gauge, polar slicing metric

$$\mathrm{d}s^2 = -\alpha^2 \mathrm{d}t^2 + X^2 \mathrm{d}R^2 + R^2 \left(\mathrm{d}\theta^2 + \sin^2\theta \mathrm{d}\phi^2\right), \tag{4.11}$$

where R is the areal radius, α the lapse function relating the proper time lapse of comoving observers to the coordinate time lapse $\mathrm{d}t$; θ and ϕ the angles describing a two-sphere; $X = \left(1 - 2Gm_{\mathrm{grav}}/(Rc^2)\right)^{-1/2}$, m_{grav} being the gravitational mass (i.e., the total energy) enclosed in a sphere of radius R. The lapse function is related with the effective GR gravitational potential $\phi_{\mathrm{GR,eff}}$ by:

$$\alpha = \exp\left(\frac{\phi_{\mathrm{GR,eff}}}{c^2}\right) \tag{4.12}$$

and $\phi_{\mathrm{GR,eff}}$ is obtained from the effective gravitational mass m_{grav}, as outlined in [107].

All the local quantities contained inside ASL, including neutrino source terms, are computed in the fluid reference frame (FRF), distinct from the coordinate frame (CF) associated with the metric Equation (4.11). The neutrino field energy in the two frames are related by a boost transformation:

$$\mathcal{E}^{\mathrm{CF}} = W(1+v)\mathcal{E}^{\mathrm{FRF}}, \tag{4.13}$$

where $W = (1 - (Xv/\alpha)^2)^{1/2}$ is the Lorentz factor, and v the radial component of the fluid velocity as measured by an observer at constant radius. Additionally,

the energy of the radiation field, climbing radially out of the gravitational well by a distance ΔR, is redshifted according to

$$\frac{\mathcal{E}^{\mathrm{CF}}(R)}{\mathcal{E}^{\mathrm{CF}}(R+\Delta R)} = \frac{\alpha(R+\Delta R)}{\alpha(R)}\,. \tag{4.14}$$

The local spectral neutrino rates s_ν are first transformed from the FRF to the CF. To design the boost transformation at a coordinate radius R for the spectral rates, we consider that the amount of emitted neutrinos (per baryonic mass) is Lorentz invariant:

$$\int_0^\infty s_{\nu,\mathrm{CF}}(R,E)E^2\mathrm{d}E\,\mathrm{d}t_{\mathrm{CF}} = \int_0^\infty s_{\nu,\mathrm{FRF}}(R,E)E^2\mathrm{d}E\,\mathrm{d}t_{\mathrm{FRF}}\,, \tag{4.15}$$

where $\mathrm{d}t_{\mathrm{FRF}}$ is the proper time and $\mathrm{d}t_{\mathrm{FRF}} = \alpha\,\mathrm{d}t_{\mathrm{CF}}$. The energy in the neutrino field transforms according to Equation (4.13):

$$\int_0^\infty s_{\nu,\mathrm{CF}}(R,E)E^3\mathrm{d}E\,\mathrm{d}t_{\mathrm{CF}} = W(1+v)\int_0^\infty s_{\nu,\mathrm{FRF}}(R,E)E^3\mathrm{d}E\,\mathrm{d}t_{\mathrm{FRF}}\,. \tag{4.16}$$

To go from the FRF to the CF, we define $f(R,E) = s_\nu(R,E)E^2$ and make the following ansatz about f in the two frames:

$$f_{\mathrm{CF}}(R,E) = \xi_2\, f_{\mathrm{FRF}}(R,\xi_1\,E)\,. \tag{4.17}$$

Then we solve for ξ_1 and ξ_2 by imposing Equations (4.15) and (4.16).

The CF transformed rates are used to evolve radially the neutrino luminosities, including the gravitational redshift. This is done in an operator splitting way: first, the luminosity is evolved between two neighboring radial zones according to equation (40) in [116]. Then the redshift correction is applied over the zone separation. We consider that, moving from R to $R+\Delta R$, the particle luminosity is not affected by the gravitational redshift in the CF frame:

$$\int_0^\infty l_{\nu,\mathrm{CF}}(R,E)E^2\mathrm{d}E = \int_0^\infty l_{\nu,\mathrm{CF}}(R+\Delta R,E)E^2\mathrm{d}E\,, \tag{4.18}$$

while the energy luminosity is (cf. Equation (4.14)):

$$\int_0^\infty l_{\nu,\mathrm{CF}}(R,E)E^3\mathrm{d}E = \frac{\alpha(R+\Delta R)}{\alpha(R)}\int_0^\infty l_{\nu,\mathrm{CF}}(R+\Delta R,E)E^3\mathrm{d}E\,. \tag{4.19}$$

In analogy with the boost transformation, we define $g(R,E) = l_\nu(R,E)E^2$ and we make the following ansatz about g between R and $R+\Delta R$:

$$g_{\mathrm{CF}}(R+\Delta R,E) = \psi_2\, g_{\mathrm{CF}}(R,\psi_1\,E)\,. \tag{4.20}$$

We solve for ψ_1 and ψ_2 by imposing Equations (4.18) and (4.19). Finally, the luminosity is locally transformed back to the FRF using the inverse of the boost transformation, Equation (4.17), to compute the spectral neutrino densities required to compute the local absorption rates. This procedure is applied over the entire radial profile.

Neutrino stress in the momentum equation and from free streaming particles is not taken into account in the current implementation.

ASL contains three free parameters that require calibration: $\alpha_{\rm blk}$, $\tau_{\rm cut}$, and $\alpha_{\rm diff}$. As outlined in [116], $\alpha_{\rm blk}$ affects the total luminosity and the heat deposition, $\tau_{\rm cut}$ the neutrino energy, and $\alpha_{\rm diff}$ the PNS cooling rate. In [116] these parameters are calibrated in 1D against detailed Boltzmann transport, using the `AGILE-BOLTZTRAN` code [81], a 15 $M_\odot$ zero-age main sequence mass progenitor [149], and the LS220 EoS. The calibrated (standard) values were $\alpha_{\rm blk} = 0.55$, $\tau_{\rm cut} = 20$, and $\alpha_{\rm diff} = 3 + 2X_h$, where X_h is the mass fraction of heavy nuclei. Since the implementation of ASL used in this comparison also contains GR corrections in contrast to the original implementation, we have repeated the calibration using the `FLASH-M1` code in 1D, the s20 progenitor and the SFHo EoS as reference case. We have obtained $\alpha_{\rm blk} = 0.5$, $\tau_{\rm cut} = 15$, and $\alpha_{\rm diff} = 3+2X_h$, comparable with the standard parameter set presented in [116]. We have tested that differences between models employing the standard and the recalibrated parameter sets do not qualitatively change the simulation outcome for the calibration setup, but the original parameters lead to undesirable quantitative discrepancies for a detailed comparison. For instance, the maximum shock radius is reached about 10 ms later.

4.2.4 Initial condition

We evolve the s15 and s20 progenitors from core collapse to ∼15 ms post-bounce using `GR1D` [108, 107] and then remap the simulations to `FLASH`. `GR1D` employs the same M1 scheme as in `FLASH-M1` but additionally includes inelastic process that are not included in `FLASH-M1`, `FLASH-IDSA`, and `FLASH-ASL` (hereafter, M1, IDSA, and ASL). This post-bounce remapping approach is similar to that employed in [110].

Restarting a `GR1D` simulation with M1 is straightforward, since M1 and `GR1D` share identical variables and inelastic processes are subdominant during the accretion phase after core bounce. However, in IDSA and ASL only trapped neutrinos are advected with the fluid. We, therefore, have to decouple trapped neutrinos from the total neutrinos in the initial conditions obtained from `GR1D`. We assume that the neutrino flux in M1 is purely from the free-streaming neutrinos and use the flux factor suggested in [78], where it was assumed that all neutrinos with a given energy are isotropically emitted at their last scattering neutrino sphere. Therefore,

$$\frac{1}{2}\int f^s(E)d\mu = \frac{2\mathcal{F}(E)}{1+\sqrt{1-\left(\frac{R_\nu(E)}{\max(r,R_\nu(E))}\right)^2}}, \tag{4.21}$$

where $\mathcal{F}(E)$ is the neutrino flux at energy E, and $R_\nu(E)$ is the corresponding neutrino sphere. $R_\nu(E)$ is determined from energy-dependent opacities and is defined as the radius where the energy-dependent optical depth becomes 2/3. Once we know the distribution function of the free-streaming neutrinos, the distribution function of the trapped neutrinos is simply $f^t(E) = \max(f(E) - f^s(E), 0)$, and the neutrino fraction and energy can be calculated by using Eqs. (3.67) and (3.68).

The comparison in the following sections are done with 12 energy bins in all three transport schemes, but it should be noted that the maximum energy bin in IDSA (200 MeV) is lower than the maximum energy bin in M1 (275 MeV) and

ASL (300 MeV). We have tested each transport scheme with a varying number of energy bins (from 12 up to 20 bins) in both 1D and 2D. No significant differences (other that stochastic variations for the 2D simulations) were found.

4.3 Results

4.3.1 Transport comparison in spherical symmetry

We perform a series of 1D spherically symmetric simulations with M1, IDSA, and ASL. We begin with a comparison of s20 with the SFHo EoS. Figure 4.1 shows the time evolution of shock radius, PNS radius and mass, mass accretion rate, and the mass and net neutrino heating rate in the gain region obtained with the different transport schemes. The mass accretion rate (measured at 500 km radius) and PNS mass are nearly identical in all three transport schemes, verifying that the initial conditions, and the hydrodynamic and gravity solvers are consistent in all three schemes. M1 restarts smoothly from the GR1D and we do not observe any noticeable effects due to relaxing the model on the FLASH grid. IDSA takes about 5 ms to relax the GR1D quantities and shows some small oscillations on the shock radius and neutrino quantities. ASL takes longer ($\sim$ 30 ms) to relax the GR1D model and a more pronounced oscillation of the PNS radius (likely due to the lack of neutrino pressure) is observed (see Figure 4.1). Since the transition from GR1D to FLASH-M1 is smooth, we attribute these early oscillations seen in IDSA and ASL to differences in the treatment of neutrino transport.

During the first $\sim$100 ms post-bounce, M1 and IDSA show a very similar shock radius evolution and peak at $\sim$145 km, while the ASL run has a relatively smaller shock radius evolution and peak at $\sim$135 km. At $\sim$15 ms, the shock radius in the ASL simulation becomes comparable to the M1 simulation, and

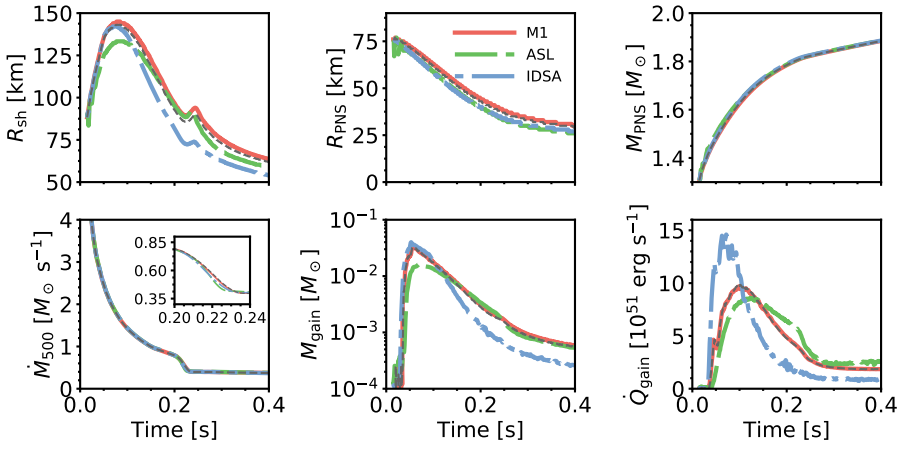

Figure 4.1: Time evolution of several shock radius, PNS radius, PNS mass, mass accretion rate, mass in the gain region, and heating in the gain region for the simulations of s20 progenitor with SFHo EoS. Different color represents simulation with different neutrino transport scheme.

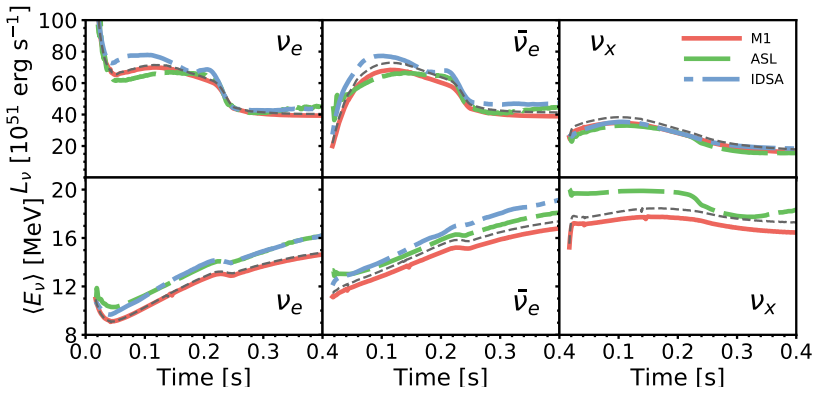

Figure 4.2: Time evolution of of neutrino luminosities (top row) and mean energies (down row) for the simulations of s20 progenitor with SFHo EoS. Different color represents simulation with different neutrino transport scheme.

after this time the evolution is similar. On the other hand, the IDSA run gives a ∼15% smaller shock radius at ∼200 ms post-bounce, but this difference becomes smaller at late time. All three schemes give a similar PNS radius and mass, but the M1 scheme has a slightly larger PNS radius, which might be due to either the different treatment of the heavy-lepton neutrinos and/or the higher PNS cooling in ASL and IDSA. Figure 4.2 shows the time evolution of neutrino luminosity and mean energy obtained with the three transport schemes. When the shock has stalled at ∼80 ms, the IDSA (ASL) run has the highest (lowest) electron neutrino luminosity $\sim 80\times10^{51}\,\mathrm{erg\,s^{-1}}$ ($\sim 60\times10^{51}\,\mathrm{erg\,s^{-1}}$) among the three schemes, and the M1 run lies between the IDSA and ASL. The same trend can be seen in the electron anti-neutrino luminosity. The IDSA and M1 show similar shock radius and PNS radius (which is approximately the radius of the neutrinosphere), resulting in a similar gain radius, but IDSA has a higher heating rates at early time and a lower heating rates at late time. We note that IDSA has a second bump on its electron neutrino luminosity at ∼200 ms. This feature does not exist in either the M1 or ASL runs, but the electron neutrino luminosity after the second bump in the IDSA matches with the M1 and ASL runs at $t > 200$ ms. A transition between two limiting cases in the IDSA diffusion solver in Equation 4.5 is a possible origin of this feature.

Both IDSA and ASL show slightly higher electron neutrino and electron anti-neutrino mean energy than M1 in the first 200 ms. The difference grow to ∼10% after ∼200 ms post-bounce. (see Figure 4.2). However, the μ/τ neutrino mean energy in ASL is usually ∼ 15% higher than in M1. This excess reduces to ∼ 10% only after the drop in the accretion rate due the progenitor shell interface. This larger excess reveals the challenge for leakage schemes to model extended scattering atmospheres. We note that the leakage solver for μ/τ neutrinos in IDSA does not track the mean energy and therefore are not plotted it in Figure 4.2.

Figure 4.3 shows the radial profiles of density, entropy, electron fraction, and heating rates of the three transport schemes at different post-bounce times. After a few hundreds ms, all schemes have developed a negative entropy gradient

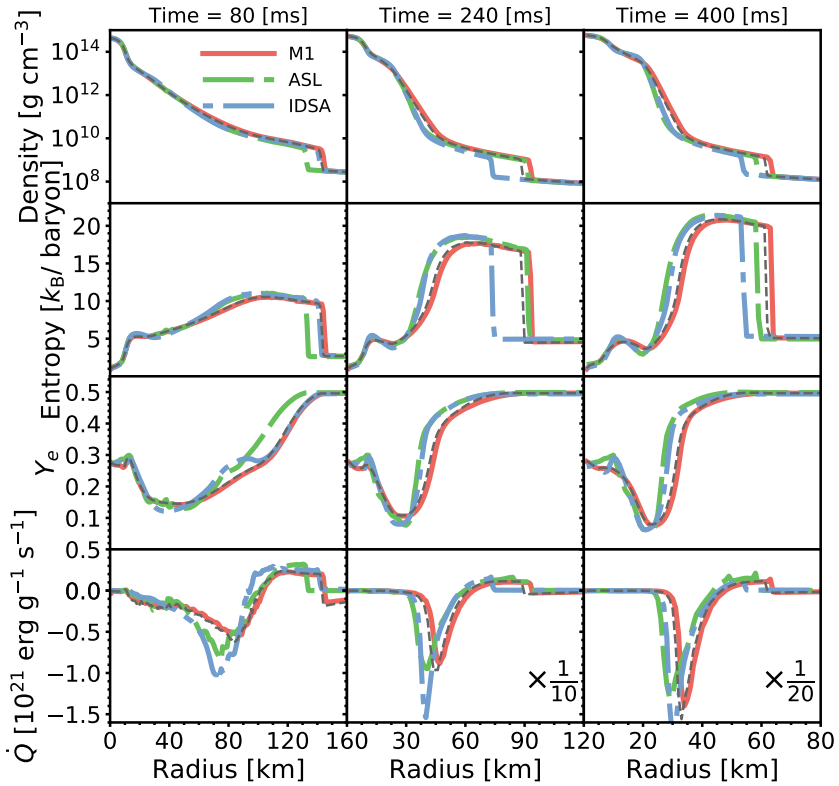

Figure 4.3: 1D radial profiles at different post bounce times for the simulations of s20 progenitor with SFHo EoS. Different color represents simulation with different neutrino transport scheme.

just below the PNS radius. The simplified treatment of the diffusive regime in leakage schemes prevents an effective transport and redistribution of the heat inside the optically thick PNS. As a consequence, the dominant heavy-flavor cooling at the PNS surface produces a more pronunced entropy gradient in ASL and IDSA, compared to M1. The negative heating rates of M1 outside of the shock front at 80 ms post-bounce is due to the exchange of momentum from streaming neutrinos. It should be noticed that ASL and IDSA only include neutrino compressional heating from trapped neutrinos, but no neutrino stress from free streaming neutrinos. During the entire post bounce evolution, M1 has the largest radial extent then IDSA and ASL. At 240 and 400 ms, all three schemes give very consistent radial profiles, except the IDSA run has a smaller shock radius at 240 ms.

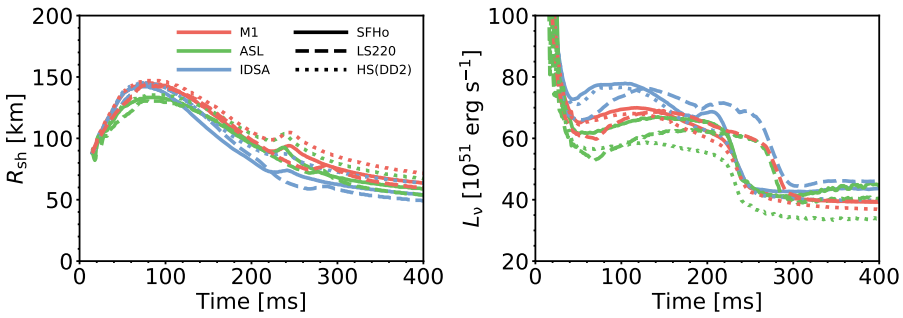

Figure 4.4: Time evolution of several shock radius and electron neutrino luminosity for the simulation of s20 progenitor. Different line style represents different EoS and different color shows simulation with different neutrino transport scheme.

4.3.2 A comparison with different EoS

Recent CCSN simulations suggest that the EoS could have impact on the explodeability [34, 135], on SASI activity [71], on the dynamics of stellar-mass black hole formation [113], on gravitational wave signals [71, 123, 113, 97], and on neutrino signals [71, 123, 113, 97]. In order to disentangle the effects of the EoS from the neutrino transport methods, we perform 1D simulations of the s20 progenitor for all the three transport methods with two additional EoS: LS220 and HS(DD2). The time evolution of shock radius and electron neutrino luminosity can be seen in Figure 4.4 for the three transport schemes we consider. The LS220 runs have a later drop in the neutrino luminosity from about ∼250 ms to ∼300 ms due to a different treatment of the low density EoS that causes a different mass accretion evolution. The simulations using the HS(DD2) EoS give the largest shock radius, followed by simulations using SFHo and LS220 EoS. The runs with SFHo (LS220) EoS have the highest (lowest) electron neutrino luminosity, respectively. The neutrino luminosity with the HS(DD2) EoS is slightly lower than that with SFHo.

All three transport schemes show the same trends while varying the EoS, suggesting that the usage of different EoS has a lower impact than the usage of different transport schemes. Therefore, the differences we discussed in the previous section do not depend on the specific choice of the EoS.

4.3.3 Transport comparison in cylindrical symmetry

In this section, we extend our comparison to multiple dimensions by comparing the three transport schemes via 2D cylindrically-symmetric simulations. In Figure 4.5, we show the same quantities for our 2D simulations as we have shown for the 1D simulations in Figure 4.1. The overall behavior is very similar to 1D until about ∼100 ms when convection begins to take hold in the gain region, breaking the spherical symmetry as visible by stronger shock oscillations, and non-zero anisotropic velocities. Up to ∼400 ms post bounce, none of the three models shows signs of incipient explosions.

Figure 4.5 reveals that both the PNS mass and accretion rate evolve simi-

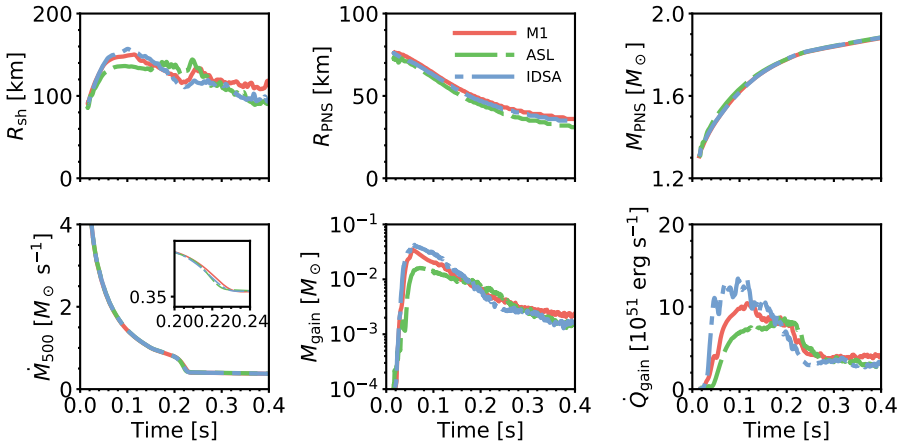

Figure 4.5: Time evolution of several shock radius, PNS radius, PNS mass, mass accretion rate, mass in the gain region, and heating in the gain region for the simulations of s20 progenitor with SFHo EoS in 2D. Different color represents simulation with different neutrino transport scheme.

larly for all treatments since they are essentially determined by the underlying progenitor structure and gravity, neither of which is strongly impacted by the neutrino transport scheme or dimensionality. This is consistent with our results in 1D (Section 4.3.1). Once spherical symmetry is broken and convection becomes non-linear (after ∼100 ms) several of these displayed quantities begin to deviate from the 1D results. The first noticeable deviation is in the shock radius (top left panel of Figure 4.5), which reaches roughly the same maximum radius (∼135 km for ASL, ∼150 km for M1 and ∼155 km for IDSA), but then has a much slower decline. When the silicon/oxygen interface accretes through the shock at ∼220 ms, the shock radii are between ∼110-130 km, which is ∼30-40 km more than the value at the corresponding time in 1D. This is due to the additional dynamical pressure support and dissipation from the turbulent motions behind the shock [104, 39, 84]. In the bottom-center and bottom-right panels of Figure 4.5, we show the mass and the neutrino heat deposition rate in the gain region, respectively. These quantities further show the qualitative effect of multidimensional dynamics on the CCSN central engine. Compared to the analogue quantities for the 1D cases in Figure 4.1, we notice a slower decrease of the mass in gain region and an increased heat deposition at later times. Both of these are a result of, and also contribute to, the presence of aspherical flows in the gain region and the increased shock radius. Lastly, we note that as seen in Figure 4.5, the PNS radius is decreasing at a slower rate in the 2D simulations compared to the equivalent 1D simulations. This is due to the presence of PNS convection.

Figure 4.6 shows the evolution of neutrino luminosities and mean energies for the 2D simulations. Compared to the 1D simulations, the non-spherical accretion of turbulent material onto the PNS leads to variable signals on small timescales. This is most evident at later times, after convection has fully developed, and in the electron neutrino and anti-neutrino signals, which are emitted

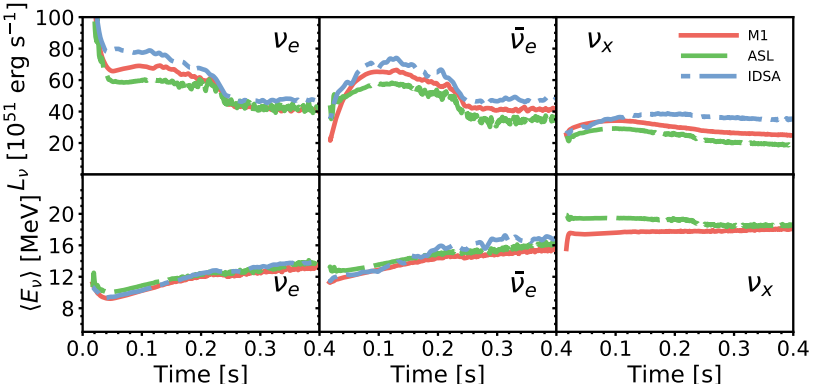

Figure 4.6: Time evolution of of neutrino luminosities (top row) and mean energies (down row) for the simulations of s20 progenitor with SFHo EoS in 2D. Different color represents simulation with different neutrino transport scheme.

closer to the material in the convection zone. The heavy-lepton neutrinos originate from deeper inside in the gravitational well where the fluid motions are calmer. In 2D, convection inside the PNS increases the heat transfer from the opaque center to the surface where neutrino cooling is more efficient. This results in higher luminosities for the representative ν_x species compared to 1D models (see the top-right panel in Figure 4.2 and Figure 4.6). The M1 simulation has less of an enhancement, consistent with the milder PNS convection discussed below.

In order to understand where the differences among the neutrino treatments occur, we consider radial profiles of angular averages at different simulation times (see Figure 4.7). These profiles confirm that also in 2D the PNS is very similar for the different schemes. However, in contrast to the 1D case, the negative entropy and lepton gradients trigger PNS convection, which leads to a flatter entropy profile below the PNS radius. The density and entropy per nucleon (first two rows in Figure 4.7) compare well at small radii, where all of the matter is shocked in each transport scheme. The differences that do arise at small radii are consistent with variations of the PNS radius. The ASL simulation shows the most compact PNS, while the PNS radius in M1 and IDSA are slightly larger. The radial profiles of density and entropy can differ substantially below the shock and inside the gain region where the angular averages contain both shocked and unshocked matter at various percentages for the different schemes. A direct comparison in this regime is less straightforward.

The neutrino radiation is chiefly coupled to the matter via energy and electron fraction source terms. In the last two rows of Figure 4.7 we show quantities related to these source terms, i.e. the electron fraction (second last row), and the rate of energy exchange between the matter and the neutrinos (bottom row; negative values means the matter is losing energy to neutrino interactions). In general, the matter begins to deleptonize after it accretes through the shock and dissociates into free neutrons and protons. The lower shock radius for ASL at 80 ms accounts for the difference in Y_e seen there. At late times ASL tends to exhibit larger electron fractions, even greater than 0.5, close to the shock

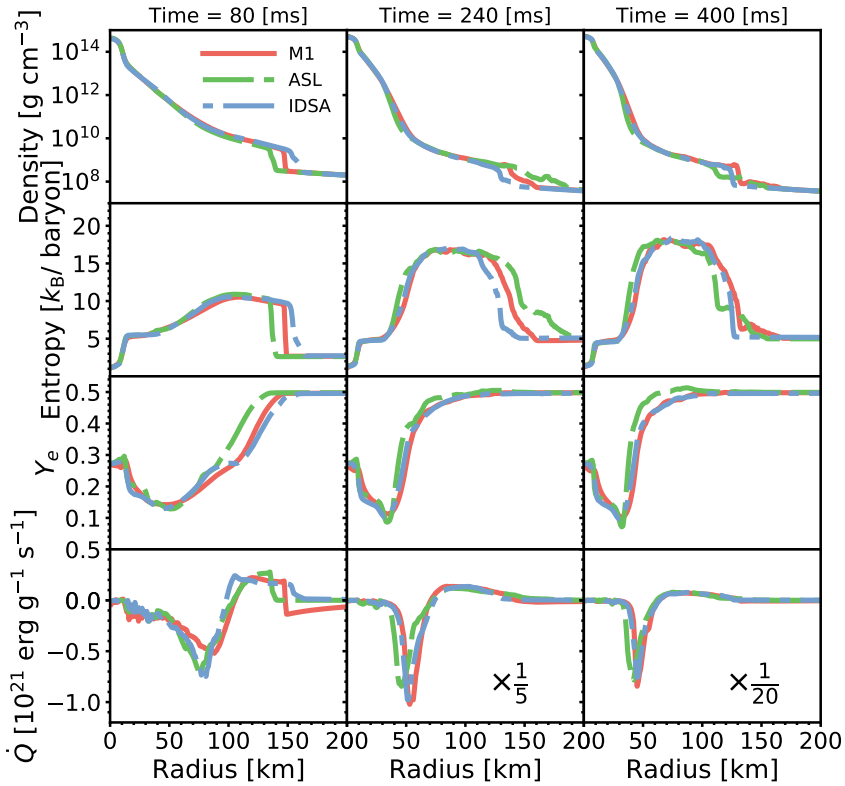

Figure 4.7: Angular averaged radial profiles at different post bounce times for the simulations of s20 progenitor with SFHo EoS in 2D. Different color represents simulation with different neutrino transport scheme.

position. The Y_e in this regime is set by the deleptonization rate, but also via the neutrino heating. In the ASL simulation, the marginally but systematically larger electron neutrino luminosity enhances the rate of conversion of neutrons into protons inside the heating region. Moreover, the ray-by-ray scheme tends to enlarge the relative differences between the electron neutrino and electron anti-neutrino spectra as seen in the luminosities in Figure 4.6.

The neutrino energy source term reveals the location and strength of the neutrino interaction, see the last row in Figure 4.7. Especially during the shock expansion at 80 ms, IDSA and ASL show a very similar cooling signature below the gain radius which is located at about 100 km. As in 1D, M1 cools less inside this region. Above the gain radius up to the shock radius, M1 and ASL show a similar heating signature where IDSA deposits slightly more heat. At radii above the shock ASL and IDSA have a vanishing neutrino energy source term, but M1 also takes the neutrino pressure work on the in-falling matter into account. Furthermore, we note that comparing to 1D (Fig. 4.3) where M1

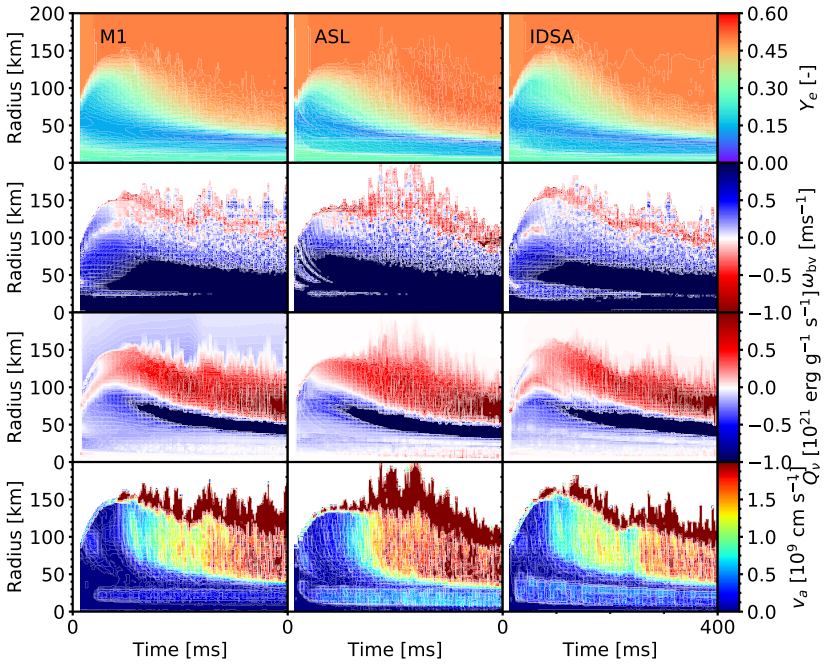

Figure 4.8: Time evolution of angular averaged profiles. Each column represents the data of one of the schemes. The first row shows the electron fraction Y_e, the second row are the profiles of the Brunt-Väisälä frequency ω_{bv}, the third row is the neutrino energy source term $\dot{Q}_\nu$, and the last row gives the anisotropic velocity v_a.

shows a larger radial extent in all given profiles (e.g. the rising entropy between 30–60 km at 240 ms), all schemes show a closer agreement in the radial extent of their equivalent 2D profiles (Fig. 4.7). Here, the strong PNS convection in ASL and IDSA lessens the difference and leads to an apparent equalization of the PNS radii among the schemes.

Figure 4.8 shows the evolution of the angle-averaged electron fraction Y_e, Brunt-Väisälä frequency [22], neutrino energy deposition, and anisotropic velocity [136], giving more insights about the 2D effects on the different schemes. During the early shock expansion (first 100 ms), these profiles are very similar, except a slightly noise around the neutrino sphere in the first 50 ms in ASL. When convection happens (after $\sim$ 100 ms), all values close to the shock surface diverge, but the central part remains comparable for all schemes and is consistent with the previous discussion on Figure 4.7.

The radial profiles of Brunt-Väisälä frequency and energy deposition reveal the different heating behavior between ASL and the other schemes during the first $\sim$100 ms. It shows that for ASL there is a lag of heating between $\sim$50–100 km during the early shock expansion which explains the lower maximum

shock radius. The lack of this heating feature in ASL is also confirmed by the anisotropic velocity profile. It shows that convection inside the gain region sets in ∼50 ms later in ASL than in the other schemes. Furthermore, the profiles of anisotropic velocity shows that IDSA and ASL tend to result in more aspherical flows inside the PNS compared to M1. This is a direct consequence of the missing energy transport in the optically thick regime typical of leakage schemes, which causes larger entropy gradients in spherically symmetric models (Section 4.3.1), and stronger convection in cylindrically symmetric ones. In fact, convection is even stronger in ASL compared to IDSA because in the former case leakage prescriptions are assumed for all neutrino flavors, while in the latter only for heavy flavor neutrinos. This stronger convection also leads to more noise in the energy source term inside the PNS in the ASL simulation: electron anti-neutrinos produced in trapped conditions just below the PNS radius are advected with the fluid at larger densities, where their presence is suppressed by lepton degeneracy. As a consequence, their energy is converted into matter internal energy and competes with local neutrino cooling. However, due to the high densities inside the PNS, this spurious effect does not translate into strong entropy artifacts, but rather in noise in the neutrino energy source term, as visible in Figure 4.6. Furthermore, the profile of anisotropic velocity reveals that ASL and IDSA evolve shock deformations very early. This is visible by the spikes in anisotropic velocity at the shock front which is a result of averages considering shocked and unshocked matter. It has also been indicated by the radial profiles in Fig. 4.7, where at 80 ms (first column) the profile for M1 shows a sharp discontinuity at the shock position, but the profiles of ASL and IDSA are slightly smoothed. This refers to acoustic waves which evolve from the strong PNS convection and aspherical accretion and disturb the spherical symmetry of the shock surface in these schemes.

A further confirmation of the robustness of this study was done by also varying the progenitor. Performing the same setup with s15 leads to the same overall behavior as seen in Figure 4.9. The s15 progenitor does not have the accretion of the shell interface at about 220 ms post bounce and the shock declines much faster which leads to a better overall agreement between all schemes.

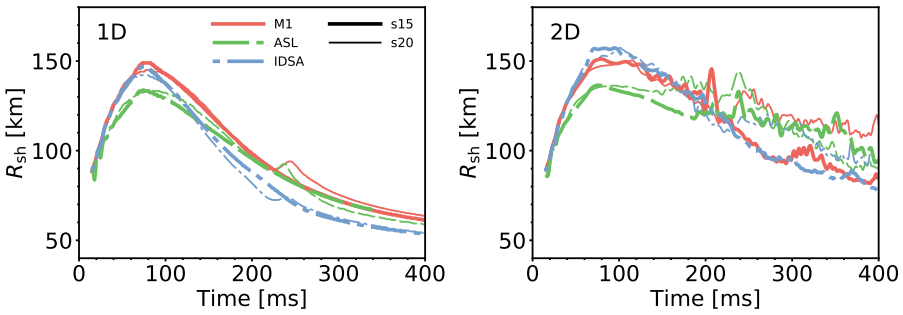

Figure 4.9: Comparison of the average shock radius for a different progenitor models. The solid lines show the data for the more compact s15 model and the dashed lines are the already shown results of s20 as a reference. Different color represents simulations with different neutrino transport scheme.

4.3.4 Sensitivity study

Multidimensional simulations using spherical grids [133, 135, 137, 131] require small initial density perturbations to trigger asymmetric motion, e.g. convection. In contrast, our 2D simulations have been performed on a cylindrical grid which naturally introduces perturbations due to the spherical flow on a Cartesian grid. In order to reveal the influence of these initial perturbations on the simulation outcome, but also the specific feedback on the different transport schemes, we perform five additional simulations adding random perturbations at the level of 0.1% in the initial post-bounce conditions for each transport scheme. We adopt the 2D setup with the s20 progenitor and SFHo EoS as described in Sec. 4.3.3.

Figure 4.10 shows the spread of average shock radii for simulations with 5 different perturbation seeds for each transport scheme. It reveals that the influence of these perturbations is very low during the the shock expansion phase ($\sim$ 100 ms). The first visible deviations among the runs for a given transport scheme (colored bands) are visible for IDSA when the shock stalls ($\sim$ 50 ms). For M1 and ASL the deviations begin growing later ($\sim$ 100 ms). These deviations happened when non-spherical transient waves moving around the post-shock region. At the moment when the progenitor shell interface crosses the shock ($\sim$220 ms), the sudden re-expansion of the shock further broadens the deviations. Even so much as to lead to an explosion in one of the five M1 simulations. The large deviations in the runs with ASL at the same time ($\sim$220 ms) might be a ray-by-ray effect in 2D which leads to enhanced post-shock fluid motions and shock deviations as described in [131], but when the shock declines again, the deviations shrink and become comparable to the deviations of the non-exploding bands of the other transport schemes. For these cases, the averaged trend remains very similar to the results of the first panel in Fig. 4.5. As

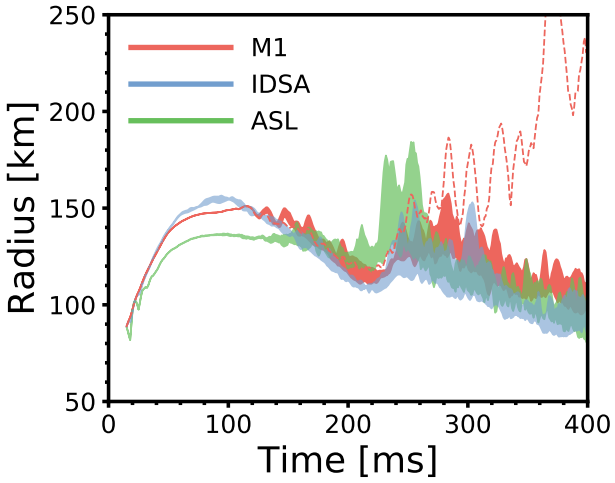

Figure 4.10: Variation bands of the average shock radius for the 2D simulations with an introduced initial density perturbation at the per mill level. Different colors represent different neutrino transport schemes. The red dashed line shows the only exploding model with M1.

conclusion, we find that IDSA is sensitive to small perturbations at early times (∼100 ms), and that the ray-by-ray implementation can amplify strong asymmetric shock expansions. Inclusion of random perturbations resulted in shock revival and explosion for one M1 simulation that failed otherwise This points to the overall sensitivity of CCSN simulations to progenitor perturbations, as discussed in detail by [34, 99, 100]. This is especially true in 2D where stochastic motions can trigger shock expansion which can be very favourable for the development of an explosion.

4.3.5 2D code performance

In this section, we give an overview of the computational performance of the different transport schemes. Our benchmark is designed as follows: we restart the 2D setup with the s20 progenitor and SFHo EoS as described in Sec. 4.3.3 at 100 ms post bounce. At this time, the averaged shock radius is almost at its maximum, see Fig. 4.5, which means that the initial AMR activity has reached an almost stable configuration. The observed range spans 100 simulation steps. We compare the ratio of core-hours spent in the neutrino treatment to the core-hours spent for solving the hydrodynamics in our simulation. The runs for the different schemes were performed on different clusters, but this ratio should robustly measure the performance of the applied scheme. Additionally from the advance in simulation time during these 100 steps, we extrapolate how many steps the simulation takes to advance one millisecond in simulation time.

Figure 4.11 summarizes the results. As expected, the M1 transport is the most expensive scheme per step, requiring eight times as many core-hours as a single hydrodynamic step. This is a result of evolving the first two moments of the neutrino distribution function. M1 is closely followed in expense by IDSA,

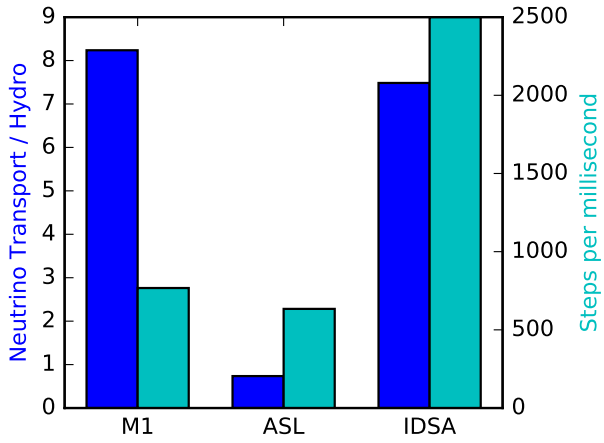

Figure 4.11: Performance comparison for the different neutrino schemes. The left axes corresponds to the blue bars (left one for each scheme) showing the ratio of core-hours spent in Radiation unit compared to the Hydro unit. The right axis corresponds to the cyan bars giving the number of steps required to advance the simulation by one millisecond.

which requires a factor of ~ 7.5 per hydrodynamic step. IDSA spends most of this time in solving the diffusion equation. ASL is the most approximate scheme, but has the advantage in efficiency. When running on a single node, the code spends almost the same computing time on the hydrodynamic calculation as on the neutrino scheme. Regarding the advance in simulation time, M1 and ASL show a comparable time step restriction which leads to a similar amount of steps to reach 1 ms simulation time. While the ASL time step is soley based on the CFL condition for the hydrodynamics (set by the sound speed c_s), M1 is set by the CFL condition for the radiation transport (set by the speed of light c). Nominally, this means a time step difference of c/c_s, but since M1 performs two radiation step per hydrodynamic step, the ratio is closer to $c/(2c_s)$. Due to the dense regions of the PNS having a very high sound speed, this ratio is close to unity. The explicit diffusion solver in IDSA requires a much smaller time step than M1 and ASL which in the current implementation is non-adaptive leading to a constant value of 2500 steps per millisecond simulation time.

The overall 2D performance of the IDSA is worse than M1 but it should be noted that the performance of `FLASH-IDSA` is tuned for 3D simulations and with GPU acceleration. To avoid the overhead of data copying between GPU and CPUs, we have added an additional layer of AMR block loop by doing data transfer and neutrino transport at the same time. The sequential calculation on CPUs leads to the low performance of IDSA in this particular benchmark.

Since the communication in the IDSA diffusion solver is mostly associated with neighboring zones, we have ported our IDSA solver with `OpenACC` for GPU acceleration. Figure 4.12 shows the relative computing time of the `FLASH-IDSA` with different dimension and block size on the Swiss supercomputer, Piz Daint. The performance is evaluated with 20 energy groups and the baseline run is using the Cray XC-30 system (with NVIDIA K20X GPU) and with 16 zones per AMR block per dimension. As discussed in Section 4.3.5, the speedup in 2D

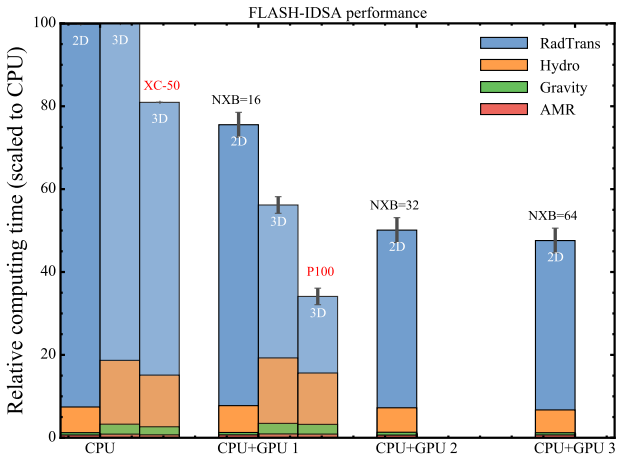

Figure 4.12: Relative computing time of IDSA on the Piz Daint supercomputer (Cray XC-30 and newly upgraded XC-50). Different group of bars represent the performance with/without GPUs and with different AMR block size. Bars with(out) red labels are running on the Cray XC-50 (XC-30) system.

is worse than 3D. This is because the 2D data in an AMR block is too small to fill the GPU cores. Increasing the AMR block size from 16×16 to 32×32 can further improve the 2D performance (see Figure 4.12). In this study, we need a controlled grid step for all transport schemes to understand the transport effect. Thus, the grid setup is not tuned to the best 2D performance, and therefore GPUs are not used in the performance study in Section 4.3.5. The new Cray XC-50 system is about 25% faster than the original XC-30 system without using GPUs. The use of P100 GPUs on XC-50 give a speed up of 2.9 in the neutrino transport region and an overall speed up of 2.3. However even with GPU acceleration, the time step in the current IDSA solver is still restricted to $\sim 4 \times 10^{-7}$ s due to the explicit implementation in the diffusion solver.

With regard to the memory consumption for the different neutrino transport schemes, IDSA only requires 4 additional variables on the solution per grid cell, i.e. 2 (Y_ν, Z_ν) $\times 2$ $(\nu_e, \bar{\nu}_e)$, which refer to the additional conservation equations for trapped neutrino particle and energy fraction, see Eqs. (3.67) and (3.68). ASL also includes the trapped component of a representative heavy flavor neutrino species ν_x, which therefore results in 2×3 variables per grid cell. The trapped neutrino spectra in the IDSA and ASL are re-constructed in a AMR block level and therefore do not need to be stored in each grid cell. On the other hand, M1 carries the spectral neutrino density (scalar) and flux (vector) on the grid which leads to 4 (density + flux) $\times$ 3 $(\nu_e, \bar{\nu}_e, \nu_x)$ $\times N_e$ (energy groups), i.e. in the case of $N_e = 12$, M1 requires 144 additional variables per grid cell. In addition to grid variables, IDSA uses $2(\nu_e, \bar{\nu}_e) \times N_e (= 12) \times R_N (= 1000)$ variables for the spherically averaged streaming source terms, and $9 \times R_N$ spherically averaged thermodynamics variables to solve the streaming component, where R_N is the number of radial zones. ASL uses 37 rays and each ray takes $6 \times R_N (= 1000)$ thermodynamics variables. These ray-by-ray variables have to be copied and synchronized for each processor but it takes much less memory than grid variables. In 2D simulations, the memory consumption of the solution usually is not a limiting factor, however it should be considered in 3D simulations where the number of grid cells significantly increases and therewith the time and memory consumption for writing checkpoints.

4.4 Conclusions

We have presented a series of 1D and 2D simulations of the s15 and s20 progenitors from [147] with the SFHo, LS220, and HS(DD2) EoS, and with three different neutrino transport schemes, including M1, IDSA, and ASL. We ran all these simulations with the publicly available code `FLASH`. While fixing the hydrodynamics and gravity solvers, we varied the progenitor model, nuclear EoS, and the neutrino transport scheme in order to investigate the impact of different transport methods on features of CCSN simulations.

In spherically symmetric simulations, all three transport schemes show consistent results on the evolution of the shock and neutrino quantities but with variation in certain metrics at about the $\sim$10% level. The variation we observe in 2D simulations is similar to that in 1D, but multidimensional convection leads to larger PNS radii and higher μ/τ neutrino luminosities. In particular, IDSA and ASL show earlier, stronger PNS convection than M1 leading to differences in the evolution of the PNS radii and neutrino luminosities. Between trans-

port schemes, an important difference is the prediction of neutrino luminosities and mean energies. Especially at later times, these quantities still show a large spread among the schemes. We find that convection around the PNS surface could produce an imbalance of electron and electron anti neutrinos in the ASL 2D run, giving large values of electron fraction (> 0.5) inside the gain region. This could be an artifact from the ray-by-ray implementation in the ASL.

When testing the sensitivity of our results to the initial progenitor profile. The differences between the transport schemes show the same trends when varying the progenitor structure and EoS. When computing resources are limited, our comparison results suggest that approximate transfer schemes can have value in their potential computational efficiency and other key factors such as nuclear EoS, turbulence, dimensionality, etc., may result in larger differences than from the neutrino transport approach. ASL runs $\sim$10 times faster than M1 and IDSA, making it possible to do a large parameter space simulations in 2D or even in 3D and giving reasonable shock dynamics. However, the ASL scheme seems to inaccurately predict the Y_e evolution, which is sensitive and important for innermost nucleosynthetic yield. In that case, one might favor the M1 scheme. The IDSA scheme lie between M1 and ASL. The IDSA runs with a slightly slower speed than M1 but is more memory efficient than M1. The memory usage could be a bottleneck for GPU programming and when moving to 3D simulations. The M1 scheme with three species neutrinos could accurately captures the changes of Y_e, and the distribution and flux of neutrinos in both opaque and transparent regions, but will cost computing time and memory.

Chapter 5

Application of ASL in FLASH

5.1 Long-time simulations using ASL

We define a long-time core-collapse supernova simulation as a simulation which follows the shock expansion after the onset of explosion for several seconds. The goal of our simulations is the extraction of representative fluid elements (tracer particles) which contain the relevant information for post-processing nucleosynthesis calculations. The setup for the long-time simulations differs from the setup used in Ch. 4. The domain is enlarged from $10,000$ km up to $160,000$ km using high and low density EoS as described in Sec. 3.3.1, where we use the EoS by Latter & Swesty [72] with a nuclear incompressibility of 220 MeV (LS220) at high densities. The progenitor, taken for the following results, is the same as in Ch. 4, i.e. the 20 $M_\odot$ solar metalicity progenitor from [148] (s20WH07), but evolved including the collapse phase. The major difference between the setup in this Chapter to the setup used in Ch. 4 is the treatment of gravity. Here, we only perform Newtonian simulations, which also means that the GR corrections in ASL are not taken into account.Compared to simulations including general relativistic corrections, in the Newtonian case, the PNS radius is much larger due to the lower gravitational acceleration. This results in larger neutrino spheres which lead to lower neutrino mean energies. However, the streaming neutrinos in the Newtonian case are not redshift corrected, but still, the inclusion of GR corrections generally tends to favor explosions [110]. We decided to exclude the effective GR potential in order to simplify the calculation, keeping in mind that we use an artificial neutrino heating factor to control the explosion. The ASL parameters for the Newtonian setup are taken from Ref. [116], i.e.:

$$\alpha_{\mathrm{bulk}} = 0.55, \tag{5.1}$$

$$\tau_{\mathrm{cut}} = 10, \tag{5.2}$$

$$\alpha_{\mathrm{diff}} = 3 + 2X_h, \tag{5.3}$$

where only τ_{cut} has been reduced from its reference value $\tau_{\mathrm{cut}} = 20$ in order to prevent heating at the PNS surface at late times when the density gradient at the PNS surface becomes very steep.

5.1.1 Collapse and Bounce

The set of reactions in our ASL implementation contains electron capture reactions on nuclei and free nucleons which allow ASL to describe the deleptonization phase. We begin with a closer look at the progenitor. According to the virial theorem, see Eq. 2.1, the stellar core is unstable if $\gamma \leqslant 4/3$. The extent of the unstable core depends much on the input physics. In the following, we compare three different EoS implementations, i.e. LS220 [72], STOS [127], and SFHo [132]. Fig.5.1 shows the radial profiles of the heat capacity ratio for the 20 $M_\odot$ progenitor model. In the case of the STOS EoS, we observe an inner unstable core and an outer unstable shell. This outlier indicates that there might be a problem with this EoS table in that region. Generally, the significant difference between the lines is surprising, since in this region, the EoS should be dominated by the well understood degenerate electron gas. However, the discrepancy may come from different compositions (considered NSE species) and their interaction with the electrons. Table 5.1 gives the enclosed masses, and radii of the inner core as well as the collapse time using ASL for the different EoS implementations. According to the differences in their core stability, each EoS has its proper collapse duration.

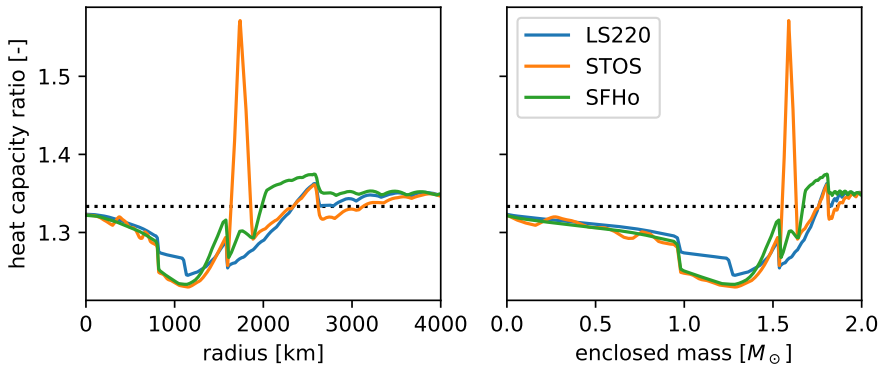

Figure 5.1: Heat capacity ratio as function of radius (left) and enclosed mass (right) of the progenitor model, s20WH07, for different EoS. The dotted line indicates the value of $\gamma = 4/3$.

mass [$M_\odot$]	radius [km]	collapse time [ms]	EoS
1.76	2350	288	LS220
1.55 – 1.88	1650 – 3100	259	STOS
1.67	2000	329	SFHo

Table 5.1: Enclosed mass and radius of the unstable core for different EoS Tables. The values for the STOS EoS refer to the unstable core and the largest unstable shell.

Since the setup for long-time simulations only uses 12 neutrino energy groups instead of 20, we need to verify that the collapse is not strongly affected by the reduction of energy groups. We repeat the above simulation using LS220

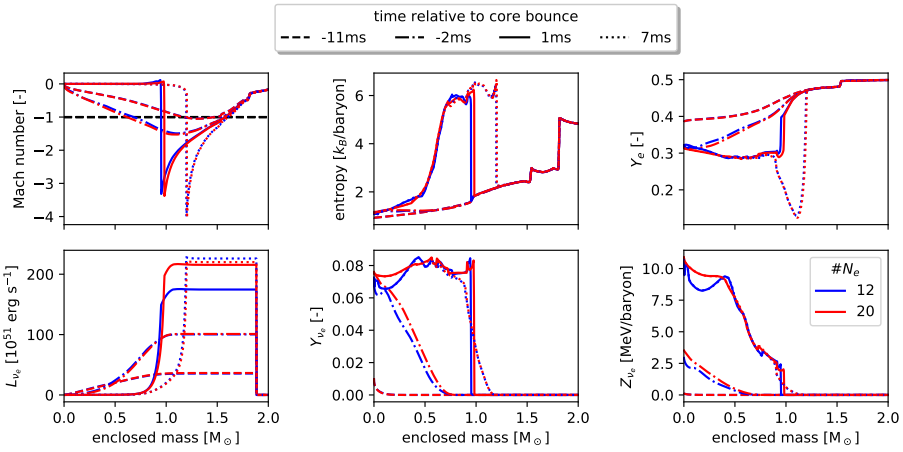

Figure 5.2: Collapse phase for simulations using 12 (blue) or 20 (red) neutrino energy groups. The different panels show mach number (sign corresponds to flow direction), entropy, electron fraction, electron neutrino energy luminosity and the electron neutrino trapped component.

and 12 energy groups. The results are presented in Fig. 5.2 which shows an almost identical evolution for both cases. The collapse time is insignificantly shorter ($\Delta t = 0.6$ ms) when running with 12 energy groups. The Mach number reveals the inner core ($|M| < 1$) which at -11 ms begins to detach at about 1.5 $M_\odot$. During the collapse the sonic point moves inwards in mass coordinate. Just before bounce, it is at about 0.5 $M_\odot$. As expected, the inner core stays unshocked, which is characterized by a lower specific entropy than the shocked matter up to the shock surface. Shortly after bounce, the neutrino burst sets in. It reduces the entropy just behind the shock. During the collapse, electron capture reactions reduce the electron fraction. While the central density rises, more and more of these electron capture neutrinos get trapped and increase the value of Y_{ν_e}. At bounce, the matter below the shock surface reaches an almost constant value of $Y_e \approx 0.3$, but as soon as the density at the shock front allows for the streaming of neutrinos, the total lepton number reduces. As a consequence, the local rate equilibrium,

$$e^- + p \rightleftharpoons n + \nu_e, \tag{5.4}$$

becomes unstable and favors the right hand side which manifests in a further reduction of Y_e. For both runs, the onset of streaming results in the same profile of lowered electron fraction at 7 ms post bounce. The build up of the luminosity is also almost identical, where the visible difference in Fig. 5.2 appears due to small time differences ($\Delta t \lesssim 0.5$ ms) in the data. We conclude, that the streaming is very well represented with 12 energy groups. Though, the trapped component builds up differently in the center. Using 12 energy groups traps up to $\sim$ 10% less neutrinos in the inner core. The central Y_e after bounce is also slightly higher when using 12 energy groups which also indicates the different deleptonization. However, if the PNS structure is not the objective of the simulation, then the collapse using only 12 energy groups is sufficient. The

results in cylindrical symmetry for the collapse are very similar and do not give further insights.

5.1.2 Shock Stalling

The early explosion phase consists of the neutrino burst and the stalling of the initially expanding shock. In addition, asymmetries in the gain region develop during this phase. Many aspects of these asymmetries have already been discussed in Ch. 4. Here, we will briefly present the shock stalling in the long-time setup without additional heating. Running the long-time simulation setup with 12 energy groups, we obtain the results presented in the first column of Fig. 5.3. We can directly compare these results to the 2D simulation presented in Ch. 4 (see Fig.4.8), which we show again in the second column. As expected, the simulation with GR corrections shows a more compact neutron star. This is truly an effect of the GR potential and not an artifact of using a different EoS, because SFHo leads to larger PNS radii than LS220, see Fig. 4.4.

After about 100 ms the shock stalls at a radius of about 180 km. Analogously to the results in Ch. 4, the averaged shock radius (blue line) begins to oscillate strongly when the Si-O shell interface in the progenitor crosses the shock surface

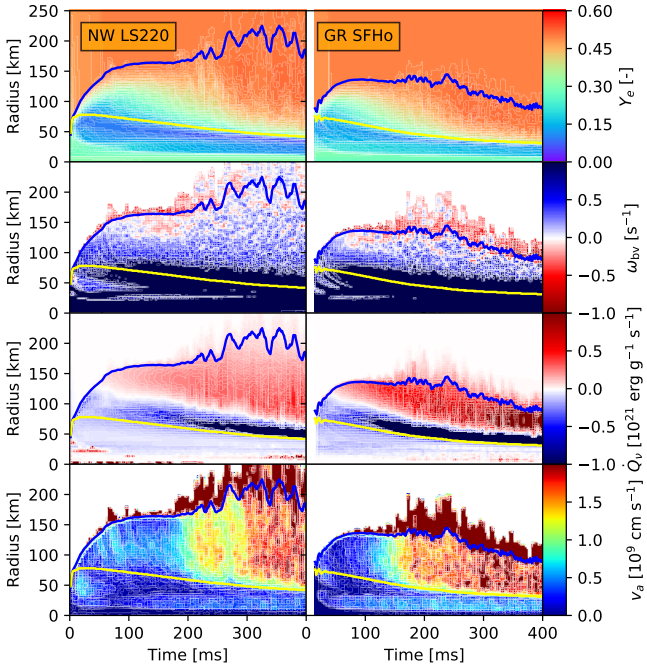

Figure 5.3: Time evolution of radial averaged profiles for the Newtonian longtime-setup (first column), and the 2D setup from Ch. 4 applying GR corrections and the SFHo EoS (second column). The first row shows the electron fraction Y_e, the second row is the profiles of the Brunt-Väisälä frequency ω_{bv}, the third row is the neutrino energy source term $\dot{Q}_\nu$, and the last row gives the anisotropic velocity v_a. On top of each panel, the blue line represents the averaged shock radius, and the yellow line is the averaged PNS radius.

at about 200 ms post bounce, but in contrast to the GR results, the averaged shock radius does not decline during the first 400 ms. Moreover, the shock surface deformation begins earlier and is more pronounced in the Newtonian case. This can be seen in the profiles of anisotropic velocity v_a, where apparently strong anisotropic areas above the averaged shock radius are the result of angle averaged areas including shocked and unshocked matter. The stronger shock deformation before 100 ms in the Newtonian case is a consequence of the stronger PNS convection as discussed below. Consistent with the GR results, ASL shows the same behavior of the neutrino energy deposition $\dot{Q}_\nu$ during the first hundred milliseconds where heating during the expansion is missing. Therefore, we confirm that the missing heating of ASL during the shock expansion is intrinsic and not an artifact of the restart procedure in Ch. 4. Another similarity is the early evolution of PNS convection though in the Newtonian case it appears stronger. This can be seen in the profiles of the Brunt-Väisälä frequency ω_{bv} and the anisotropic velocity v_a during the first 100 ms between 25 km and the PNS radius (yellow line). The convection is triggered by the energy release of trapped neutrinos which in the Newtonian case is clearly visible in the profile of $\dot{Q}_\nu$ at about 25 km. The heating that appears in the PNS center (below 25 km) is the adjustment of the trapped component to the weak equilibrium. It might be reduced when using 20 energy groups, but it stays located at the center and does not raise convection. After about 200 ms the central adjustment disappears.

Fig. 5.4 gives further diagnostic quantities which have also been discussed in Fig. 4.1. As expected, it reveals that the PNS mass is greater and that the mass accretion rate is stronger in the general relativistic treatment. Interestingly, the mass inside the gain region is greater in the Newtonian case, but the energy deposition initially is not. This relates to the fact, that despite the redshift of

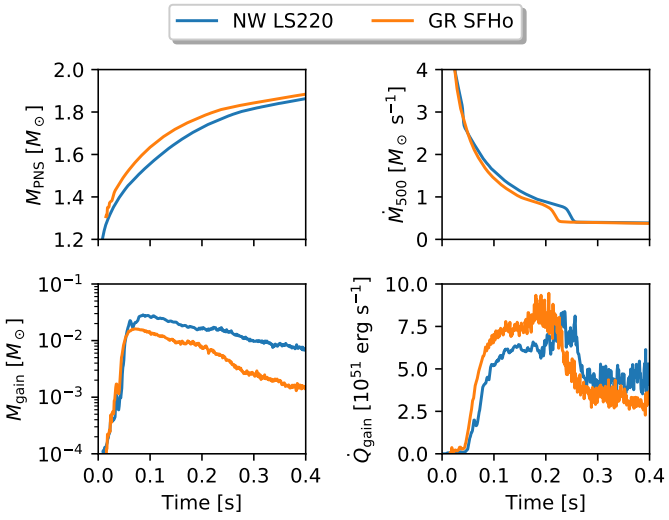

Figure 5.4: Time evolution of PNS mass, mass accretion rate at 500 km, mass in the gain region, and heating in the gain region for the long-time simulation setup (blue) and the 2D run from Ch. 4 (orange).

neutrinos, generally the GR treatment favors explosions, see e.g. [110].

Altogether, we can summarize up to this point, that the long-time setup produces results which are qualitatively comparable with the results that we have presented in Ch. 4.

5.1.3 Explosion

In this subsection, we compare different explosion models. In order to produce different explosions, we use the neutrino heating factor as introduced in Eq. 3.96 and perform six runs varying the heating factor between 1 and 1.6. The objective is to study the longtime behavior of our simulation setup with respect to a possible post-processing nucleosynthesis. We define the explosion time, as the time after bounce when the mean shock radius passes 500 km. Upon this definition, all models explode during the first second. The results for the first second after core bounce are shown in Fig. 5.5. As expected, models with a higher heating factor explode earlier and therefore accrete less mass on the PNS. After the explosion time, the mass accretion rate as defined in

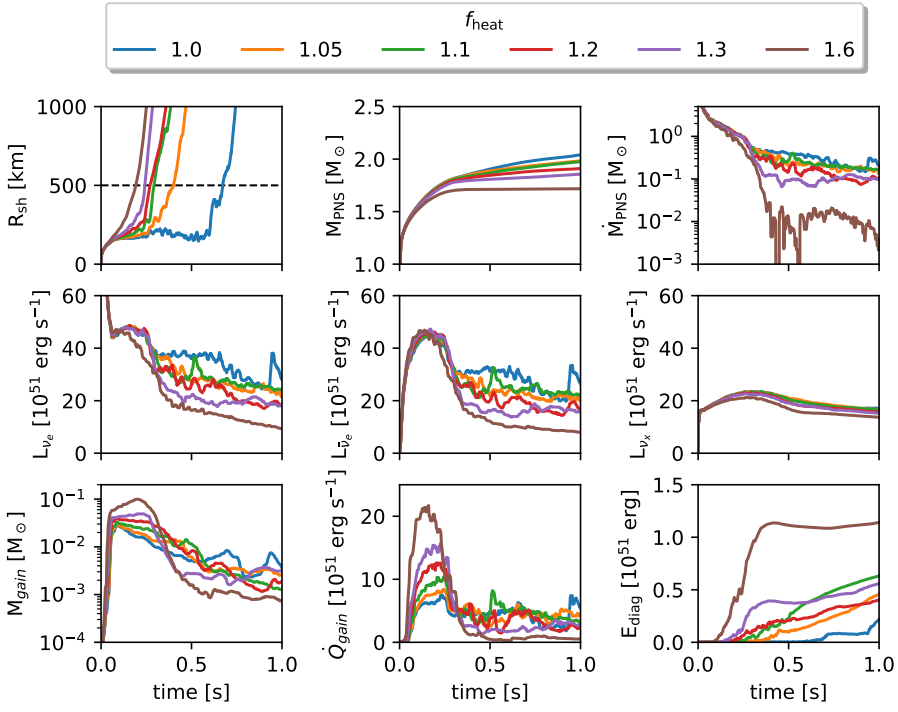

Figure 5.5: First second after bounce for models whith different heating factors. From the upper left penel to the right in the first row, we present the evolution of shock radius, where the radius of 500 km (dashed line) indicates the onset of explosion, the PNS mass, the mass accretion rate of the PNS. The second row shows the energy luminosities for the different ASL neutrino flavors, and in the last row, we display the mass of the gain region, the neutrino energy deposition in the gain region, and the diagnostic energy.

Ch. 4, i.e. accretion rate at 500 km, may falsify the actual value. Hence, we consult the mass accretion rate directly on the PNS in the following. Except the run with $f_{heat} = 1.6$ which appears like a prompt explosion, all models show a similar behavior up to about 200 ms post bounce when the progenitor shell interface crosses the shock surface. From then on the electron (anti-) neutrino luminosities show a wide scatter among the models. The values range between 20×10^{51} to 40×10^{51} erg s^{-1} and are very noisy which directly results from the also noisy accretion. The ν_x-luminosity stays smooth which reflects that these neutrinos originate mainly from the inner PNS. Another direct correlation to the heating factor is found on the mass and neutrino energy deposition inside the gain region during the first 200 ms. A counter-intuitive result is the relation between heating factor and diagnostic energy. Naively, one could expect that the more efficient the energy deposition of neutrinos the greater the explosion energy which seems true for the case with $f_{\rm heat} = 1.6$. However, the diagnostic energy for the other models grows at very different rates, so that e.g. the case with $f_{\rm heat} = 1.1$ reaches a higher diagnostic energy after one second than models with higher heating factor. This is caused by the non-linear feedback of neutrinos produced by accretion on the internal energy of the ejected matter.

Focusing on the nucleosynthesis, we present the peak temperature at the shock front and the amount of unbound matter in Fig. 5.6. The peak temperature is obtained by the maximum temperature in the volume between the shock surface and a virtual surface laying 5% of the shock radius below in radial direction. The amount of unbound (i.e. positive total energy) mass is measured as difference relative to the reference case[1]. Since, the amount of ejected (i.e. unbound, positive radial velocity, and radial location $\geq$ 500 km from the PNS center) mass for the reference case is negligible compared to the other models, as seen later in Fig. 5.7, the shown values represent the ejected mass quite well (± 0.02 M$_\odot$). The peak temperature at the shock is a good indicator for the explosive nucleosynthesis. Matter, that falls through the shock surface, heats up and as long as the temperature is sufficiently high, the progenitor composition

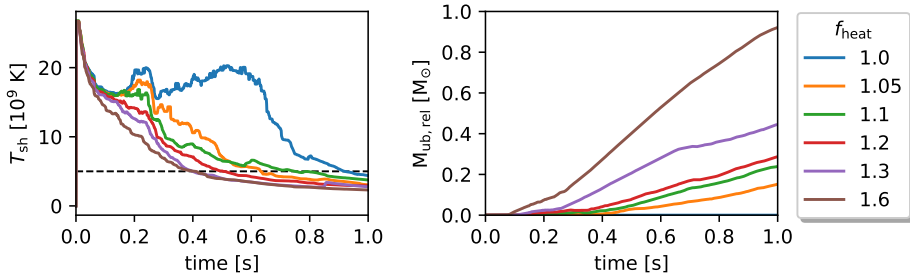

Figure 5.6: Evolution of the peak shock temperature (left panel) and the mass of unbound matter relative to the run using $f_{\rm heat} = 1.0$ (right panel). The black dashed line in the left panel indicates 5 GK, which approximately is the threshold for matter in NSE (5 GK).

gets processed. An indicator for the temperature where NSE can establish is

[1] A numerical offset in the absolute value originates from a side effect of the inflow condition, and possibly by a mismatch of the zero point energy for the specific internal energy in the EoS table.

f_{heat}	1.00	1.05	1.10	1.20	1.30	1.60
t_{expl} [ms]	672	399	293	271	243	192
$t(T_{\mathrm{sh}} < 5 \times 10^9$ K) [ms]	917	631	749	493	399	398
$\mathrm{M_{PNS}}(t = 1$ s) [$\mathrm{M_\odot}$]	2.04	1.98	1.96	1.91	1.86	1.72
$\mathrm{E_{diag}}(t = 1$ s) [10^{51} erg s^{-1}]	0.22	0.46	0.63	0.40	0.56	1.14
$\mathrm{M_{ub,rel}}(t = 1$ s) [$\mathrm{M_\odot}$]	0.00	0.15	0.24	0.29	0.44	0.92

Table 5.2: Diagnostics of the explosions up to one second post bounce. For the different models, we present the explosion time, and the time when the shock peak temperature falls below 5 GK. Furthermore, we give the values for the PNS mass, the diagnostic energy, and the mass of unbound matter after one second.

5 GK. Except the model with $f_{\mathrm{heat}} = 1.05$, the time when the peak temperature does not reach NSE anymore anti-correlates with the heating factor. Since, the peak temperature somehow probes the minimum shock radius, an asymmetric explosion could be the reason for the breaking of this correlation. The amount of ejected mass again shows the expected correlation. In table 5.2, we quantitatively summarize the above-mentioned results after the first second for the different explosion models.

The peak shock temperature is only one indicator for the nucleosynthesis during the explosion. Most of the mass may follow much deeper below the shock surface. In the interest to decide whether the majority of ejected matter is still processing its composition or not, we decompose the ejected mass at $t = 1$ s for a subset of the explosion models, see Fig. 5.7. Matter above 10 GK is certainly in NSE, below 10 GK down to about 5 GK the composition may reach NSE and down to 1 GK the nucleosynthesis shuts down. Below 1 GK, the composition is frozen and matter gets simply ejected. The electron fraction reveals in how far matter has also been processed by neutrino interactions. The electron fraction up to the Helium shell, see Fig. 2.2, is about $Y_e = 0.5$. For all models except $f_{\mathrm{heat}} = 1.00$, the majority of ejected mass is already below 3 GK after the first second and has an electron fraction of about $Y_e = 0.5$. The spread around $Y_e = 0.5$ is not symmetric. Since the valley of stability favors neutron-rich isotopes, we can assume that this also holds for the ejecta. However, the model with $f_{\mathrm{heat}} = 1.00$ favors proton-rich ejecta. To understand the difference between the model with $f_{\mathrm{heat}} = 1.00$ and the others, and also give an explanation why the diagnostic energy at one second does not correlate with the heating factor, we look at the radial position of the ejecta and its angular direction. We take into account the morphology of the explosion by distributing the angular bins weighted with the corresponding solid angel, i.e. a flat distribution in the fourth column of Fig. 5.7 corresponds to a spherically symmetric mass ejection. Comparing the different models, it clearly reveals that the first model differs strongly to the other models, because it is a weak bipolar explosion that after one second still has most of its ejecta below 5000 km. We

[3]By construction, neutrinos in our simulation are only coupled to the hydrodynamics up to $r_{\mathrm{max}} = 3000$ km, see Fig. 3.3

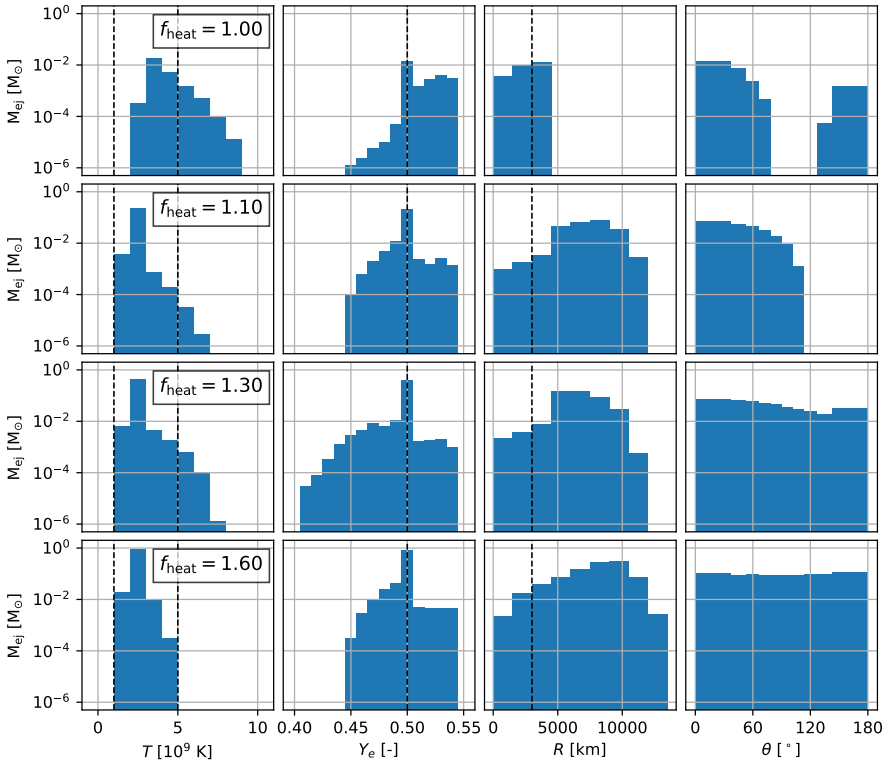

Figure 5.7: State of the ejected matter for four explosion models after one second. Each row represents the results for one corresponding model. The columns from left to right show the distributions of temperature, electron fraction, radial position, and direction of the ejected mass. The vertical lines in these columns mark 1 GK and 5 GK (NSE freeze out), $Y_e = 0.5$ (symmetric matter), and the distance of 3000 km to the PNS center (shut down of neutrino interaction[3]). In the last column, the angular bins are chosen to match an equal solid angel.

also see that the ejection to the northern hemisphere ($\theta < 90°$) is stronger in this case. The ejection for the case with $f_{\rm heat} = 1.10$ appears mono-polar into the northern hemisphere. The comparably high diagnostic energy at this time results from the strong one sided accretion. The models with greater heating factors lead to almost spherically symmetric mass ejection, where the case of $f_{\rm heat} = 1.60$ is the most advanced one and the explosive nucleosynthesis is already freezing out its composition.

One second after core bounce, we find that all models in our study explode with a variety of mass ejection morphology. Up to 200 ms, the models evolve as expected regarding the different neutrino heating factors, but the later accretion phase leads to unpredictable evolution which shades the naively expected correlations with the heating factor, e.g. diagnostic energy, or shock peak temperature.

5.1.4 Long-Time Evolution

None of the presented runs has established a neutrino-driven wind after one second. It may appear at a later time and eject the matter which is interesting for nucleosynthesis studies. Furthermore, the diagnostic energy did not saturate yet and therefore does not allow for a prediction of the observable explosion energy. Hence, we continue the evolution of the presented models.

Running the models up to five seconds produces the results presented in Fig. 5.8. Due to numerical problems, the run with $f_{\mathrm{heat}} = 1.00$ could not continue beyond ~ 3 s after core bounce. After five seconds, neither the shock radius position, nor the PNS mass, correlates with the heating factor anymore. Only the two models with the largest heating factor manage to shut down the accretion onto the PNS. It even appears as if these models produce a neutrino driven wind after 4 s which reduces the PNS mass. However at the same time, the neutrino luminosities of these models experience a strong increase which is a side effect of the ray-by-ray implementation of ASL. The PNS density gradient at later times gets very steep which makes the transition from trapped to free streaming neutrinos very fragile, i.e. the optical depth cutoffs $\mathcal{H}$ in Eq. 3.89 together with the grid interpolation can lead to explosive heating inside the PNS

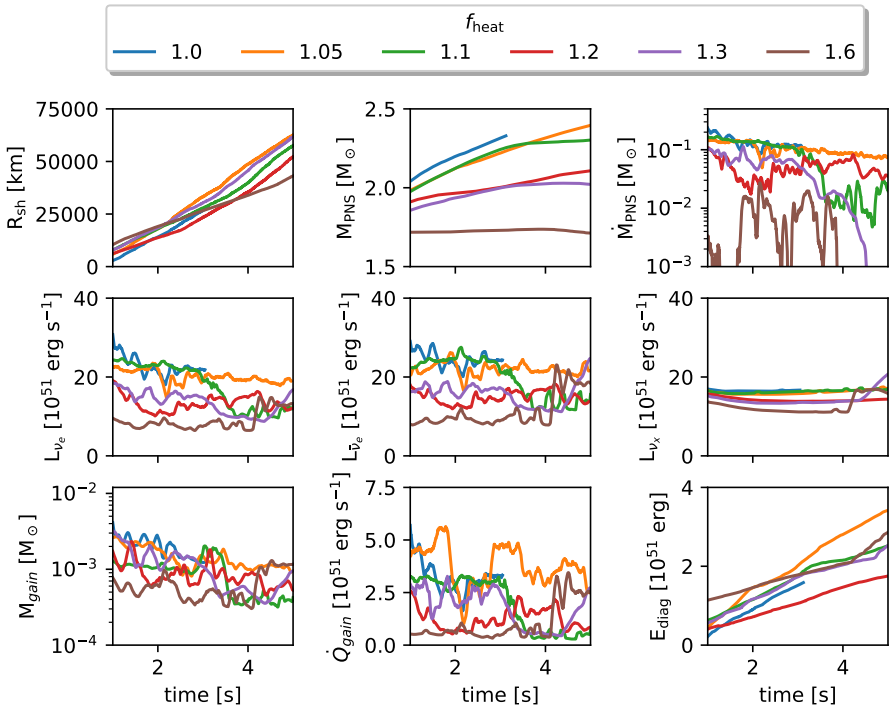

Figure 5.8: Evolution after one second for models whith different heating factors. From the upper left penel to the right in the first row, we present the evolution of shock radius, the PNS mass, the mass accretion rate of the PNS. The second row shows the energy luminosities for the different ASL neutrino flavors, and in the last row, we display the mass of the gain region, the neutrino energy deposition in the gain region, and the diagnostic energy.

which then begins to peel off the PNS crust. Another problem of the simulation setup concerns the diagnostic energy. Instead of saturating, it continues growing. Even for the case with $f_{\mathrm{heat}} = 1.60$, where during the first second it appeared to saturate, it continues growing for the following seconds. The origin of the continuously growing diagnostic energy are the very long lasting down flows which result in PNS masses beyond 2 $\mathrm{M}_\odot$. The questions that arise are: can we explain these down flows? And how does ASL deal with the high neutron star masses?

Beginning with the latter question, we take a closer look at the evolution of the reference case with $f_{\mathrm{heat}} = 1.00$ regarding the trapped component and the inner PNS. At about 300 ms, when the mass accretion rate declines, the PNS begins to cool faster. This results in the reduction of trapped neutrino component and therewith trapped neutrino energy, i.e.

$$E_{\mathrm{tr}} = \int_{\mathrm{M_{PNS}}} \frac{1}{m_u} (Z_{\nu_e} + Z_{\bar{\nu}_e} + 4Z_{\nu_{\mu,\tau}})\, \mathrm{d}m, \tag{5.5}$$

as seen in the first panel of Fig. 5.9. However, at about 800 ms the simulation experiences a glitch. All of a sudden, the central density drops from about 3.5×10^{14} to 2.5×10^{14} g cm^{-3}. At this time the averaged PNS density stalls for about 50 ms, but then continues growing again. Also the central density raises again together with the total trapped energy, but after the glitch, the PNS center begins moving in southern direction. A good reason why the trapped component has initiated the glitch is the direct link of trapped energy to the specific internal energy, see Eq. 3.95. Another weak point of ASL is the reconstruction of the trapped distribution function which is only based on the trapped neutrino density Y_ν, but not on Z_ν. Therefore, the resulting distribution func-

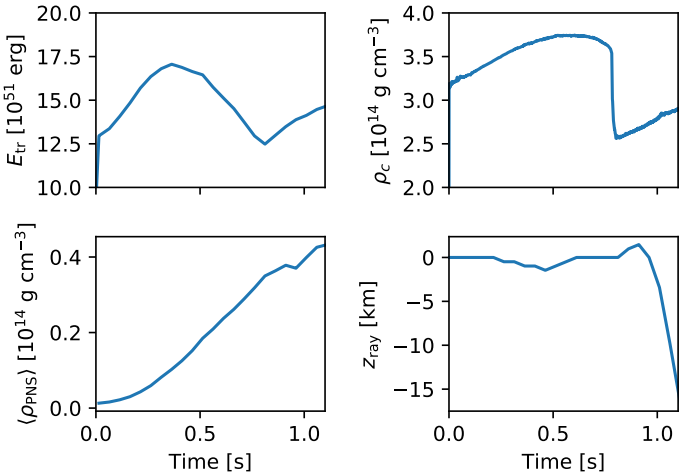

Figure 5.9: Evolution of the PNS during the first second after core bounce. From the upper left to the lower right, the panels show the total amount of trapped neutrino energy, the central density, the averaged PNS density, and the coordinate of the leakage ray center with respect to the simulation domain center. Note, that the ray center is also the position of maximum density.

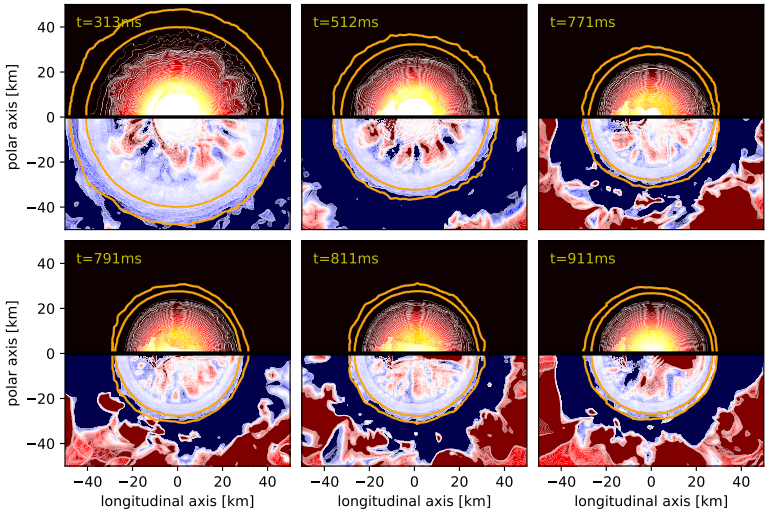

Figure 5.10: Evolution of the PNS through the glitch. On each panel, the upper half gives the distribution of the trapped specific energy ranging from 0 (black) to 10^{19} erg g^{-1} (white), the lower half shows the neutrino energy deposition between $\pm 10^{21}$ erg g^{-1} s^{-1}, where red indicates heating (positive sign) and blue cooling (negative sing), respectively. The yellow contours refer to the densities of 10^{11} g cm^{-3} and 10^{12} g cm^{-3}, where the inner corresponds to the greater value.

tion f^t in Eq. 3.76, might reproduce a wrong energy state after normalization. The response is a large neutrino energy source term for the trapped component. The course of the glitch is shown in Fig. 5.10. Before the mass accretion rate drops, at about 300 ms, the inner core of the PNS, below 10 km from the center, appears inactive. This is expected, because at densities above 10^{13} g cm^{-3}, neutrinos are in chemical and thermal equilibrium with the matter. However, once the accretion rate drops, pressure waves start propagating through the PNS and perturb the equilibrium. The traces of these waves are visible in the second panel of Fig. 5.10 in the inner core for instance. Furthermore, the initially spherically symmetric distribution of neutrino energy gets broken and a large amount of energy accumulates on the southern part of the PNS, see third panel. The perturbation grows and in less then 20 ms the whole inner core gets affected. The release of neutrino energy causes the strong decompression of the center which afterwards again starts contracting. The pressure waves only propagate along the longitudinal axis which is a side effect of our symmetry which forces the PNS center to stay on the longitudinal axis. In order to prevent the contraction which caused the glitch, we tried to include the neutrino pressure of the trapped component, given by Eq. 25 in Ref. [116],

$$P_\nu = \frac{1}{3}\frac{\rho}{m_u}(Z_{\nu_e} + Z_{\bar{\nu}_e} + 4Z_{\nu_{\mu,\tau}}). \tag{5.6}$$

Unfortunately, it made the simulation unstable causing artificial shocks already during the collapse phase. As a workaround to prevent high neutrino energy deposition in the PNS center, we smoothly shut down the neutrino source terms above the density of 10^{13} g cm^{-1}. The idea is to enforces the rate equilibrium and keeps the inner core unperturbed. Still the question remains how far we can trust the PNS evolution with ASL. At late times neutrino diffusion becomes the dominant energy transport inside the PNS as well as convection, but the energy transport with ASL at high density seems fragile.

The remaining question concerns the long lasting down flows. When we take a closer look at the fluid motion, we find that the late-time accretion particularly comes from the equatorial plain. Our simulation models do not include rotation, therefore it might come from the imposed symmetry. As discussed in e.g. [52, 33], the inverse turbulent energy cascade in two dimensions favors large-scale motion of matter instead of dissipating it into smaller scales. We confirm that these down flows are not the result of an unfavorable choice of parameters by changing the EoS to the SFHo [132], which has also been used in Ch. 4. We also varied the ASL parameters, i.e. $\tau_{\text{cut}} \in [5, 15]$ and $\alpha_{\text{bulk}} \in [0.5, 0.6]$. Furthermore, we have included the momentum source term, Eq. 41 in [116]

$$\dot{\mathbf{v}}^s(\mathbf{x}) = \left(\frac{1}{c}\sum_{\nu}\int_0^{\infty} h_\nu(E,\mathbf{x})\mu_\nu(E,\mathbf{x})E^3\,\mathrm{d}E\right)\mathbf{n}_r, \tag{5.7}$$

into our ASL implementation which so far has been missing. Here, $\mathbf{n}_r$ is the normalized vector in radial direction and the other variables are the same as defined in Ch. 3. However, the down flows and the increasing diagnostic energy remain. It turns out, that these down flows originate from a gigantic convection cycle. Matter, that crosses the shock surface, moves towards the equatorial plane. At the interface where the flows from the northern and southern hemisphere collide, a new shock forms. At this interface, the tangential component of the fluid velocity vanishes. In the case of a spherical explosion, the flow splits into a fraction that flows outwards and the remaining part, that falls back on the PNS. At the height of about 2/3 the distance to the shock, the matter floats. When the falling matter eventually reaches the PNS, it gets heated in a rather turbulent flow. However, the hot matter lifts up on large cones along the longitudinal direction and aligns with the matter that falls through the shock. The cycle is shown in Fig. 5.11, where we see the tangential component of the normalized velocity,

$$\mathbf{n}_{\mathbf{v}} = \frac{\mathbf{v}}{|\mathbf{v}|}, \tag{5.8}$$

on the upper half and the radial component on the lower half. From left to right, we see representations of the different ejection/shock morphologies as discussed before, i.e. bipolar for $f_{heat} = 1.0$, monopolar for $f_{heat} = 1.0$, and spherical for $f_{heat} = 1.3$. In the case of the bipolar explosion, we see the colliding tangential flows at the equatorial plane. The radial component tells us that strong down flows originate from this area including material that passes the shock from the equator. The radial component also reveals the extent of the ejection cones where the one in northern direction is greater as already seen in Fig. 5.7. The second panel shows the case of a monopolar explosion. All matter below the shock has a velocity component towards the southern hemisphere. In the southern hemisphere, accreded matter falls into the PNS environment. The

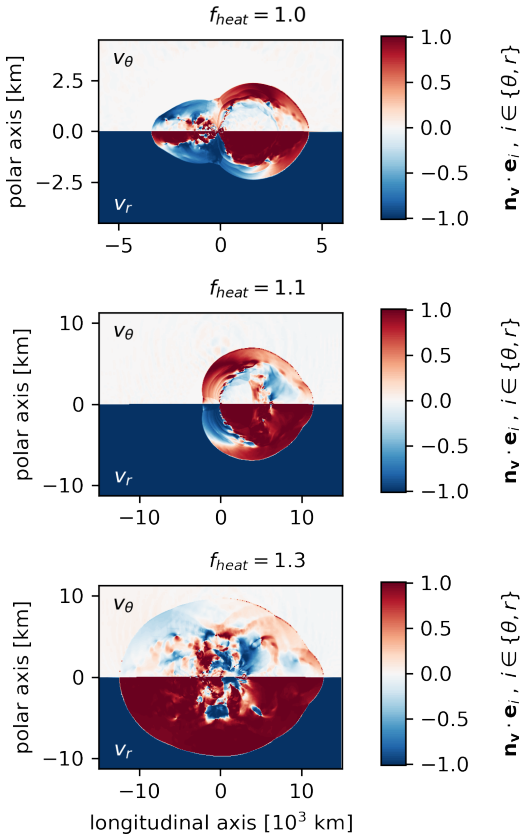

Figure 5.11: Normalized velocity components for a isotropic mass ejection (left) and a polar mass ejection (right) at 1 s after core bounce. The upper half on each panel presents the tangential component where blue represents a clockwise velocity and red a counter clockwise motion. The lower half shows the radial component, where blue represents in-falling matter and red is ejected matter. The coordinate origin lies on the PNS center.

case of a spherically symmetric explosion has similar tangential flows close to the shock surface as the bipolar case, but the dominating direction is the radial flow. The region of interest here, is in the equatorial plane and reaches up to 5000 km above the PNS center. The separation line between accretion and ejection (floating matter) is clearly visible in the radial component. From this height, matter falls into the PNS environment and leads to the continuously growing energy release. For the strong explosion case, we would expect that this cycle may stop and a wind could follow, but as seen Fig. 5.8 the simulation becomes unstable when the PNS detaches from the expanding envelope.

The cycle that we found might be an artifact of the cylindrical symmetry and may not be present in full 3D simulation. It explains why we do not observe a saturation of the diagnostic energy. Altogether, we conclude that ASL predicts reasonable results up to 1s. However, the longtime behavior of our

simulation needs further investigation. Moreover, there is the PNS convection which may need a more elaborate treatment. My suggestion is to assume the equilibrium distribution for neutrinos at densities greater than 10^{13} g cm^{-3}. And include the pressure of the trapped component as function of density in the EoS. Maybe the sink in internal energy due to neutrino trapping together with the missing neutrino pressure of the trapped component leads to artifacts such as the observed glitch in the run with a heating factor of 1. The values of electron fraction at the shock are reasonable so that the study of the explosive nucleosynthesis may be fine.

Chapter 6

Summary and Conclusions

Neutrinos play a crucial role in the dynamics of core-collapse supernovae. Therefore, an appropriate treatment of neutrinos is essential in order to generate reliable results. However, solving the seven dimensional Boltzmann transport equation is in most cases numerically impracticable. When performing parameter studies or performing multidimensional simulations, the choice of the neutrino treatment is a decision between accuracy of the solution and consumption of computational resources. A good approximation should capture all essential features relevant for the underlying study.

The major part of this thesis was the implementation of the approximate neutrino treatment ASL [116] into the simulation framework `FLASH` [48, 43]. Beside a neutrino light bulb [34] and a gray leakage scheme [37] at present, there are three spectral neutrino schemes available in FLASH which are M1 [110], IDSA [114], and our implementation of ASL. In order to investigate the differences between these neutrino treatments, we have performed a detailed comparison in spherical and cylindrical symmetry. Using the same hydrodynamics code and gravity solver has allowed us to disentangle effects on the evolution which are caused by the neutrino scheme from those which may be caused by other sources, e.g. grid effects. The results are presented in Ch. 4 which is based on Ref. [115]. For this study, we extended ASL with the leading order GR corrections, which are the gravitational redshift and doppler correction of the streaming neutrino energies, see Sec. 4.2.3. We have found that all schemes produce consistent results in spherical symmetry, with variation in certain metrics, e.g. luminosities at 100 ms, below 10% on the predicted neutrino quantities. The comparison in cylindrical symmetry shows the important influence of PNS convection on the neutrino schemes and their impact on the overall evolution. Especially, the neutrino luminosities and mean energies show a large spread among the schemes even at later times. Asymmetries at the PNS surface translate to jittering luminosities which in the case of ASL propagate to the gain region through the rays. The imbalance of ν_e & $\bar{\nu}_e$ at the trace of the rays leads to large values of electron fraction inside the gain region. We have also noticed, while testing the sensitivity of our results, that the explosiveness of the progenitor model, used in our study, can be triggered by a 0.1% density perturbation in the initial 2D profile which might be regardless of the neutrino treatment. In the presented study, ASL is the most approximate treatment. However, ASL shows its strength in its efficiency. In cylindrical symmetry, ASL runs about 10 times

faster than M1 and IDSA, and we expect a greater factor in full 3D simulations. When computing resources are limited, approximate neutrino treatments are still valuable and are able to produce competitive results.

In Ch. 5 of this work, we have presented the application of ASL in long-time simulations. We have investigated different explosions by variation of an artificial heating factor. It reveals that ASL is a good approximation for the collapse phase and the first second after core bounce. During the first second the results are consistent with the findings of the study presented in Ch. 4 including the fact that in this chapter we have used the standard Newtonian implementation of ASL. Among the explosion models, we have found a variety of ejection morphologies including monopolar, bipolar, and spherical mass ejection. We have seen that the morphology has a strong impact on the dynamics but also on the diagnostic quantities such as peak shock temperature or the diagnostic energy. Despite the imposed heating factor, the driving force of the explosions is an aspherical accretion (down flow) which is part of a giant flow cycle. Matter that falls through the shock accumulates at in the equatorial plane and falls into the vicinity of the PNS. There it gets ejected in the polar direction. The symmetry of this cycle lets us infer that it may be an artifact of the cylindrical symmetry. At one second after core bounce, we have investigated several indicators for the nucleosynthesis in the distribution of ejected matter. For almost all models the majority of ejected matter has already cooled down below 3 GK which implies that the explosive nucleosynthesis is already fading in these models.

A problem of ASL that has already been observed in Ch. 4 is the prediction of large values of the electron fraction. This has also been found for these explosion models, where for all models values of about $Y_e = 0.54$ has been observed for more than 10^{-3} $M_\odot$ of ejecta. In order to observe a neutrino driven wind, we have ran the models for more than one second. We have encountered that the long lasting down flow and its non linear feedback leads to very unpredictable results. After one second, the neutrino luminosities become very noisy as well as the extent of the gain region. The diagnostic energy continues rising for all models, even those with initially strong explosions. The cases in which we could find an ejection of matter driven by neutrinos from the PNS surface turned out to be a numerical artifact and unfortunately does not represent a realistic neutrino driven wind. The other weak point of ASL mentioned in Ch. 4 is the PNS convection. Accordingly, we have also analyzed the influence of the trapped component in the long-time setup. The trapped neutrino component inside the PNS seems to become unstable under certain circumstances. During the long-time simulation, we observed a sudden decompression of the PNS center which was induced by a sudden release of trapped energy. The trigger has been an aspherical distribution which was induced by the PNS convection. We tried a different treatment of the trapped component for densities above 10^{13} g cm^{-3} which directly enforces the equilibrium distribution for trapped neutrinos without the fragile reconstruction from the neutrino density. This could facilitate the incorporation of neutrino pressure from the trapped component which in the current implementation is still missing.

Despite these issues found in ASL, we still see the potential in full 3D simulations where a higher focus might lay on effects originating from other sources, e.g. magnetic field. Moreover, we expect that 3D simulations using ASL might relativize the encountered issues found in 2D simulations. For example the amount of mass which is influenced by a single ray is equal in 3D, which means

that effects of asymmetries on the PNS surface have the same impact on the total luminosities and averaged neutrino energies independent of their exact location on the PNS surface. In the appendix A, we shown that our implementation of ASL scales on large number of computing nodes and is ready for the usage in 3D.

Appendix A

Preview of ASL in full 3D simulations

The efficiency of ASL may offer the ability to explore simulations taking into account all directional degrees of freedom (3D) at reasonable computational costs. In this section, we present the scaling results of ASL for a similar setup as presented in Ch. 4. The only difference is a slightly smaller domain containing only the inner 6,000 km of the star. The angular resolution in azimuth direction is equal the polar resolution in Ch. 4 leading to the total number of 2522 rays. The following performance tests have been made on the on the Swiss National Supercomputing Centre (CSCS) using the machine Piz Daint. At present, each CPU node on Piz Daint consists of two Intel Xenon E5-2695v4 processors allowing for the use of 36 cores per node and 128 GB RAM. Our first goal is to investigate the scaling of ASL when working on a large number of computing nodes. The critical step in our algorithm is the calculation of the optical depths, Eq. 3.66, and the solution of Eq. 3.89 in order to compute the spectral neutrino density of the free streaming component, Eq. 3.90. This step requires the global redistribution of data among the MPI ranks. Our benchmark is the computation of the first 100 steps for the given setup. The rays are equally distributed among the MPI ranks and the calculation on the rays is performed in every time step. One problem is, that the 3D simulation requires more memory than a single node can offer, hence we compute our scaling relative to 10 Nodes, which is fine for our goal, because the when computing on a large number of of MPI ranks, we can expect that the limiting operation may likely become the inter node communication.

Fig. A.1 summarizes the scaling for a variation of the number of computing nodes. The first panel shows how much time is required for our benchmark. The green line shows the result for the ASL performance and the red line reveals how much time in ASL has been used for the communication between MPI ranks. As reference for the total costs of ASL in this simulation setup, we also present the total evolution time and the time required to solve the conservation equations (eqs. 3.14, 3.17, 3.18). In contrast to the performance in 2D shown in Ch.5, this setup is highly dominated by solving the conservation equations. However, the important result is that the time spend in communication does not rise and that for 160 nodes, ASL is still not dominated by its communication. The second

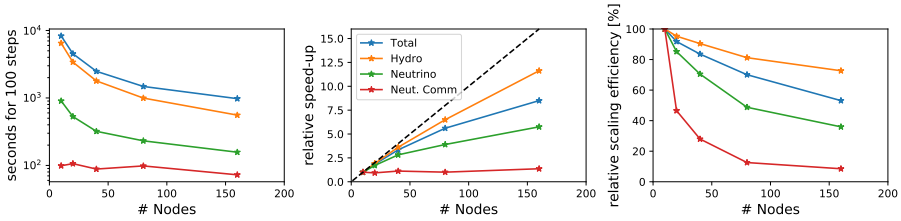

Figure A.1: Scaling plots for ASL in 3D performed on the Piz-Daint cluster at CSCS. The workload is evolving the simulation for 100 steps. The first panel gives the time consumption, the central panel is the speed-up, the last panel shows the strong scaling for the total simulation (blue), the hydrodynamics solver (yellow), the neutrino treatment (green), and the communication inside the neutrino treatment (red). The dashed line in the central panel indicates the perfact scaling relation.

panel shows the relative speed-up which is the ratio of the time consumption for 10 nodes t_{10} to the time consumption of the actually used number of nodes t_N. The ideal speedup represented by the dashed black line is the case when the time consumption for the solution reduces proportional to the amount of acquired working resources (nodes). On this panel we confirm that the communication stays at a constant level. The speedup of ASL is expected to saturate once the time consumption for communication equals the time spend on calculations. At the last panel, we show the relative scaling efficiency η_k, which is defined by

$$\eta_k(N) = \frac{t_k}{(N/k)t_N} \times 100\%, \tag{A.1}$$

where k is the number of reference working units (in our case $k = 10$ nodes), and N is the number of working units. It tells how far the actual speedup compares to the ideal speedup. It is an important quantity in order to judge if a further allocation of resources is reasonable. In our benchmark the total efficiency using 160 nodes is already at about 50%, but please note that it includes the writing of an output file.

Since our simulation is a hybrid code which uses parallelism on shared memory via openMP as well, we also investigate the thread scaling behavior of ASL. We performed runs using 10 nodes, each using 6 MPI ranks. The results are shown in Fig. A.2. It reveals, that ASL benefits much by increasing the amount of threads. Interestingly, the time consumption for the communication in ASL also reduces. This cannot be a direct effect of the hyper threading, but it may be a result of reduced idle time which occurs when a process needs the data of a ray that is still in the queue of another process on a different MPI rank. However, since ASL is not the simulation's bottleneck, the massive use of threads is not recommended. Though, it turns out that when using only few nodes, the memory consumption does not allow for the full allocation of all cores available on the node with MPI ranks and therefore the usage of hyper threading up to the limit of available cores is justified.

We expect that 3D simulations using ASL might relativize the encountered issues found in 2D simulations, see Ch. 4. For instance, the amount of mass which is influenced by a single ray is equal in 3D, which means that effects of

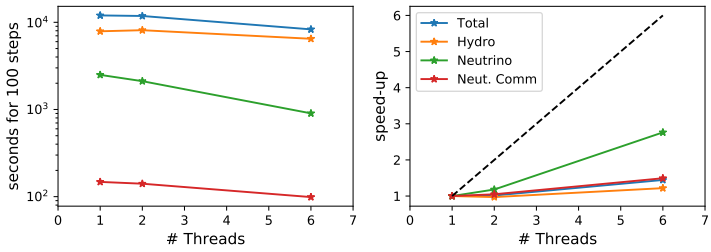

Figure A.2: Thread scaling plots for ASL in 3D performed on the Piz-Daint cluster at CSCS. The workload is evolving the simulation for 100 steps. The left panel shows the time consumption, the right panel is the speed-up for the total simulation (blue), the hydrodynamics solver (yellow), the neutrino treatment (green), and the communication inside the neutrino treatment (red). The dashed line in the right panel indicates the perfact scaling relation.

asymmetries on the PNS surface have the same impact on the total luminosities and averaged neutrino energies which therewith becomes independent of their exact location on the PNS surface.

Bibliography

[1] B. P. Abbott, R. Abbott, T. D. Abbott, F. Acernese, K. Ackley, C. Adams, T. Adams, P. Addesso, R. X. Adhikari, V. B. Adya, and et al. Multi-messenger Observations of a Binary Neutron Star Merger. *ApJ*, 848:L12, Oct. 2017.

[2] A. Arcones and J. Bliss. Nucleosynthesis of elements between Sr and Ag in neutron- and proton-rich neutrino-driven winds. *Journal of Physics G Nuclear Physics*, 41(4):044005, Apr. 2014.

[3] A. Arcones and H.-T. Janka. Nucleosynthesis-relevant conditions in neutrino-driven supernova outflows. II. The reverse shock in two-dimensional simulations. *A&A*, 526:A160, Feb. 2011.

[4] A. Arcones, H.-T. Janka, and L. Scheck. Nucleosynthesis-relevant conditions in neutrino-driven supernova outflows. I. Spherically symmetric hydrodynamic simulations. *A&A*, 467:1227–1248, June 2007.

[5] A. Arcones, G. Martínez-Pinedo, E. O'Connor, A. Schwenk, H.-T. Janka, C. J. Horowitz, and K. Langanke. Influence of light nuclei on neutrino-driven supernova outflows. *Phys. Rev. C*, 78(1):015806, July 2008.

[6] D. Arnett. Mass dependence in gravitational collapse of stellar cores. *Canadian Journal of Physics*, 45:1621–1641, 1967.

[7] D. Arnett. *Supernovae and Nucleosynthesis: An Investigation of the History of Matter from the Big Bang to the Present.* Princeton University Press, 1996.

[8] W. D. Arnett. Gravitational collapse and weak interactions. *Canadian Journal of Physics*, 44:2553–2594, 1966.

[9] M. Arnould, S. Goriely, and K. Takahashi. The r-process of stellar nucleosynthesis: Astrophysics and nuclear physics achievements and mysteries. *Phys. Rep.*, 450:97–213, Sept. 2007.

[10] D. S. Balsara. Second-Order-accurate Schemes for Magnetohydrodynamics with Divergence-free Reconstruction. *ApJS*, 151:149–184, Mar. 2004.

[11] E. Bear and N. Soker. Neutron Star Natal Kick and Jets in Core Collapse Supernovae. *ApJ*, 855:82, Mar. 2018.

[12] H. Berninger, E. Frenod, M. Gander, M. Liebendörfer, J. Michaud, and N. Vasset. A Mathematical Description of the IDSA for Supernova Neutrino transport, its discretization and a comparison with a finite volume scheme for Boltzmann's Equation. *ArXiv e-prints*, Nov. 2012.

[13] H. A. Bethe. Supernova mechanisms. *Reviews of Modern Physics*, 62:801–866, Oct. 1990.

[14] H. A. Bethe and J. R. Wilson. Revival of a stalled supernova shock by neutrino heating. *ApJ*, 295:14–23, Aug. 1985.

[15] G. S. Bisnovatyi-Kogan. The Explosion of a Rotating Star As a Supernova Mechanism. *Soviet Ast.*, 14:652, Feb. 1971.

[16] S. I. Blinnikov, I. V. Panov, M. A. Rudzsky, and K. Sumiyoshi. The equation of state and composition of hot, dense matter in core-collapse supernovae. *A&A*, 535:A37, Nov. 2011.

[17] J. Bliss, M. Witt, A. Arcones, F. Montes, and J. Pereira. Survey of Astrophysical Conditions in Neutrino-driven Supernova Ejecta Nucleosynthesis. *ApJ*, 855:135, Mar. 2018.

[18] J. M. Blondin, A. Mezzacappa, and C. DeMarino. Stability of Standing Accretion Shocks, with an Eye toward Core-Collapse Supernovae. *ApJ*, 584:971–980, Feb. 2003.

[19] V. Brdar, M. Lindner, and X.-J. Xu. Neutrino astronomy with supernova neutrinos. *Journal of Cosmology and Astroparticle Physics*, 4:025, Apr. 2018.

[20] S. W. Bruenn. Stellar core collapse - Numerical model and infall epoch. *ApJS*, 58:771–841, Aug. 1985.

[21] S. W. Bruenn, E. J. Lentz, W. R. Hix, A. Mezzacappa, J. A. Harris, O. E. B. Messer, E. Endeve, J. M. Blondin, M. A. Chertkow, E. J. Lingerfelt, P. Marronetti, and K. N. Yakunin. The Development of Explosions in Axisymmetric Ab Initio Core-collapse Supernova Simulations of 12-25 M Stars. *ApJ*, 818:123, Feb. 2016.

[22] R. Buras, M. Rampp, H.-T. Janka, and K. Kifonidis. Two-dimensional hydrodynamic core-collapse supernova simulations with spectral neutrino transport. I. Numerical method and results for a 15 $M_\odot$ star. *A&A*, 447:1049–1092, Mar. 2006.

[23] A. Burrows. Colloquium: Perspectives on core-collapse supernova theory. *Reviews of Modern Physics*, 85:245–261, Jan. 2013.

[24] A. Burrows, J. Hayes, and B. A. Fryxell. On the Nature of Core-Collapse Supernova Explosions. *ApJ*, 450:830, Sept. 1995.

[25] A. Burrows, S. Reddy, and T. A. Thompson. Neutrino opacities in nuclear matter. *Nuclear Physics A*, 777:356–394, Oct. 2006.

[26] A. Burrows, D. Vartanyan, J. C. Dolence, M. A. Skinner, and D. Radice. Crucial Physical Dependencies of the Core-Collapse Supernova Mechanism. *Space Sci. Rev.*, 214:33, Feb. 2018.

[27] R. M. Cabezón, D. García-Senz, and A. Relaño. A one-parameter family of interpolating kernels for smoothed particle hydrodynamics studies. *Journal of Computational Physics*, 227:8523–8540, Oct. 2008.

[28] R. M. Cabezón, K.-C. Pan, M. Liebendörfer, T. Kuroda, K. Ebinger, O. Heinimann, A. Perego, and F.-K. Thielemann. Core-collapse supernovae in the hall of mirrors. A three-dimensional code-comparison project. *A&A*, 619:A118, Nov. 2018.

[29] J. I. Castor. Radiative Transfer in Spherically Symmetric Flows. *ApJ*, 178:779–792, Dec. 1972.

[30] S. Chandrasekhar. The highly collapsed configurations of a stellar mass (Second paper). *Monthly Notices of the Royal Astronomical Society*, 95:207–225, Jan. 1935.

[31] P. Colella and P. R. Woodward. The Piecewise Parabolic Method (PPM) for Gas-Dynamical Simulations. *Journal of Computational Physics*, 54:174–201, Sept. 1984.

[32] S. A. Colgate and R. H. White. The Hydrodynamic Behavior of Supernovae Explosions. *ApJ*, 143:626, Mar. 1966.

[33] S. M. Couch. On the Impact of Three Dimensions in Simulations of Neutrino-driven Core-collapse Supernova Explosions. *ApJ*, 775:35, Sept. 2013.

[34] S. M. Couch. The Dependence of the Neutrino Mechanism of Core-collapse Supernovae on the Equation of State. *ApJ*, 765:29, Mar. 2013.

[35] S. M. Couch, E. Chatzopoulos, W. D. Arnett, and F. X. Timmes. The Three-dimensional Evolution to Core Collapse of a Massive Star. *ApJ*, 808:L21, July 2015.

[36] S. M. Couch, C. Graziani, and N. Flocke. An Improved Multipole Approximation for Self-gravity and Its Importance for Core-collapse Supernova Simulations. *ApJ*, 778:181, Dec. 2013.

[37] S. M. Couch and E. P. O'Connor. High-resolution Three-dimensional Simulations of Core-collapse Supernovae in Multiple Progenitors. *ApJ*, 785:123, Apr. 2014.

[38] S. M. Couch and C. D. Ott. Revival of the Stalled Core-collapse Supernova Shock Triggered by Precollapse Asphericity in the Progenitor Star. *ApJ*, 778:L7, Nov. 2013.

[39] S. M. Couch and C. D. Ott. The Role of Turbulence in Neutrino-driven Core-collapse Supernova Explosions. *ApJ*, 799:5, Jan. 2015.

[40] C. L. Cowan, Jr., F. Reines, F. B. Harrison, H. W. Kruse, and A. D. McGuire. Detection of the Free Neutrino: A Confirmation. *Science*, 124:103–104, July 1956.

[41] P. F. de Salas, S. Gariazzo, O. Mena, C. A. Ternes, and M. Tórtola. Neutrino Mass Ordering from Oscillations and Beyond: 2018 Status and Future Prospects. *Frontiers in Astronomy and Space Sciences*, 5:36, Oct. 2018.

[42] P. B. Demorest, T. Pennucci, S. M. Ransom, M. S. E. Roberts, and J. W. T. Hessels. A two-solar-mass neutron star measured using Shapiro delay. *Nature*, 467:1081–1083, Oct. 2010.

[43] A. Dubey, L. B. Reid, K. Weide, K. Antypas, M. K. Ganapathy, K. Riley, D. Sheeler, and A. Siegal. Extensible Component Based Architecture for FLASH, A Massively Parallel, Multiphysics Simulation Code. *Parallel Computing*, 35(10-11):512–522, Mar. 2009.

[44] M. Eichler, K. Nakamura, T. Takiwaki, T. Kuroda, K. Kotake, M. Hempel, R. Cabezón, M. Liebendörfer, and F.-K. Thielemann. Nucleosynthesis in 2D core-collapse supernovae of 11.2 and 17.0 $M_\odot$ progenitors: implications for Mo and Ru production. *Journal of Physics G Nuclear Physics*, 45(1):014001, Jan. 2018.

[45] G. G. Emch and C. Liu. *The logic of thermostatistical physics*. Springer-Verlag, 2002.

[46] T. Ertl, M. Ugliano, H.-T. Janka, A. Marek, and A. Arcones. Erratum: "Progenitor-explosion Connection and Remnant Birth Masses for Neutrino-driven Supernovae of Iron-core Progenitors". *ApJ*, 821:69, Apr. 2016.

[47] T. Fischer, M. Hempel, I. Sagert, Y. Suwa, and J. Schaffner-Bielich. Symmetry energy impact in simulations of core-collapse supernovae. *European Physical Journal A*, 50:46, Feb. 2014.

[48] B. Fryxell, K. Olson, P. Ricker, F. X. Timmes, M. Zingale, D. Q. Lamb, P. MacNeice, R. Rosner, J. W. Truran, and H. Tufo. FLASH: An Adaptive Mesh Hydrodynamics Code for Modeling Astrophysical Thermonuclear Flashes. *ApJS*, 131:273–334, Nov. 2000.

[49] P. Goldreich and S. V. Weber. Homologously collapsing stellar cores. *ApJ*, 238:991–997, June 1980.

[50] S. A. Grebenev, A. A. Lutovinov, S. S. Tsygankov, and C. Winkler. Hard-X-ray emission lines from the decay of ^{44}Ti in the remnant of supernova 1987A. *Nature*, 490:373–375, Oct. 2012.

[51] B. W. Grefenstette, F. A. Harrison, S. E. Boggs, S. P. Reynolds, C. L. Fryer, K. K. Madsen, D. R. Wik, A. Zoglauer, C. I. Ellinger, D. M. Alexander, H. An, D. Barret, F. E. Christensen, W. W. Craig, K. Forster, P. Giommi, C. J. Hailey, A. Hornstrup, V. M. Kaspi, T. Kitaguchi, J. E. Koglin, P. H. Mao, H. Miyasaka, K. Mori, M. Perri, M. J. Pivovaroff, S. Puccetti, V. Rana, D. Stern, N. J. Westergaard, and W. W. Zhang.

Asymmetries in core-collapse supernovae from maps of radioactive ^{44}Ti in CassiopeiaA. *Nature*, 506:339–342, Feb. 2014.

[52] F. Hanke, A. Marek, B. Müller, and H.-T. Janka. Is Strong SASI Activity the Key to Successful Neutrino-driven Supernova Explosions? *ApJ*, 755:138, Aug. 2012.

[53] F. Hanke, B. Müller, A. Wongwathanarat, A. Marek, and H.-T. Janka. SASI Activity in Three-dimensional Neutrino-hydrodynamics Simulations of Supernova Cores. *ApJ*, 770:66, June 2013.

[54] S. Hannestad and G. Raffelt. Supernova Neutrino Opacity from Nucleon-Nucleon Bremsstrahlung and Related Processes. *ApJ*, 507:339–352, Nov. 1998.

[55] J. A. Harris, W. R. Hix, M. A. Chertkow, C. T. Lee, E. J. Lentz, and O. E. B. Messer. Implications for Post-processing Nucleosynthesis of Core-collapse Supernova Models with Lagrangian Particles. *ApJ*, 843:2, July 2017.

[56] K. Hebeler, J. M. Lattimer, C. J. Pethick, and A. Schwenk. Equation of State and Neutron Star Properties Constrained by Nuclear Physics and Observation. *ApJ*, 773:11, Aug. 2013.

[57] M. Hempel, T. Fischer, J. Schaffner-Bielich, and M. Liebendörfer. New Equations of State in Simulations of Core-collapse Supernovae. *ApJ*, 748:70, Mar. 2012.

[58] M. Hempel and J. Schaffner-Bielich. A statistical model for a complete supernova equation of state. *Nuclear Physics A*, 837:210–254, June 2010.

[59] F. Hoyle and W. A. Fowler. Nucleosynthesis in Supernovae. *ApJ*, 132:565, Nov. 1960.

[60] K. Huang. *Statistical mechanics*. Wiley, New York, 1987.

[61] J. P. Hughes, C. E. Rakowski, D. N. Burrows, and P. O. Slane. Nucleosynthesis and Mixing in Cassiopeia A. *ApJ*, 528:L109–L113, Jan. 2000.

[62] H.-T. Janka. *Supernovae und kosmische Gammablitze: Ursachen und Folgen von Sternexplosionen (Astrophysik aktuell) (German Edition)*. Spektrum Akademischer Verlag, 2011.

[63] H.-T. Janka. Explosion Mechanisms of Core-Collapse Supernovae. *Annual Review of Nuclear and Particle Science*, 62:407–451, Nov. 2012.

[64] O. Just, R. Bollig, H.-T. Janka, M. Obergaulinger, R. Glas, and S. Nagataki. Core-collapse supernova simulations in one and two dimensions: comparison of codes and approximations. *MNRAS*, 481:4786–4814, Dec. 2018.

[65] F. Käppeler, R. Gallino, S. Bisterzo, and W. Aoki. The s process: Nuclear physics, stellar models, and observations. *Reviews of Modern Physics*, 83:157–194, Jan. 2011.

[66] R. Käppeli, S. C. Whitehouse, S. Scheidegger, U.-L. Pen, and M. Liebendörfer. FISH: A Three-dimensional Parallel Magnetohydrodynamics Code for Astrophysical Applications. *ApJS*, 195:20, Aug. 2011.

[67] R. Kippenhahn and A. Weigert. *Stellar Structure and Evolution*. Springer-Verlag, 1994.

[68] F. S. Kitaura, H.-T. Janka, and W. Hillebrandt. Explosions of O-Ne-Mg cores, the Crab supernova, and subluminous type II-P supernovae. *A&A*, 450:345–350, Apr. 2006.

[69] K. Kotake. Multiple physical elements to determine the gravitational-wave signatures of core-collapse supernovae. *Comptes Rendus Physique*, 14:318–351, Apr. 2013.

[70] T. Krüger, I. Tews, K. Hebeler, and A. Schwenk. Neutron matter from chiral effective field theory interactions. *Phys. Rev. C*, 88(2):025802, Aug. 2013.

[71] T. Kuroda, K. Kotake, and T. Takiwaki. A New Gravitational-wave Signature from Standing Accretion Shock Instability in Supernovae. *ApJ*, 829:L14, Sept. 2016.

[72] J. M. Lattimer and F. Douglas Swesty. A generalized equation of state for hot, dense matter. *Nuclear Physics A*, 535:331–376, Dec. 1991.

[73] N. M. Law, S. R. Kulkarni, R. G. Dekany, E. O. Ofek, R. M. Quimby, P. E. Nugent, J. Surace, C. C. Grillmair, J. S. Bloom, M. M. Kasliwal, L. Bildsten, T. Brown, S. B. Cenko, D. Ciardi, E. Croner, S. G. Djorgovski, J. van Eyken, A. V. Filippenko, D. B. Fox, A. Gal-Yam, D. Hale, N. Hamam, G. Helou, J. Henning, D. A. Howell, J. Jacobsen, R. Laher, S. Mattingly, D. McKenna, A. Pickles, D. Poznanski, G. Rahmer, A. Rau, W. Rosing, M. Shara, R. Smith, D. Starr, M. Sullivan, V. Velur, R. Walters, and J. Zolkower. The Palomar Transient Factory: System Overview, Performance, and First Results. *PASP*, 121:1395, Dec. 2009.

[74] D. Lee. A solution accurate, efficient and stable unsplit staggered mesh scheme for three dimensional magnetohydrodynamics. *Journal of Computational Physics*, 243:269–292, June 2013.

[75] D. Lee, A. E. Deane, and C. Federrath. A New Multidimensional Unsplit MHD Solver in FLASH3. In N. V. Pogorelov, E. Audit, P. Colella, and G. P. Zank, editors, *Numerical Modeling of Space Plasma Flows: ASTRONUM-2008*, volume 406 of *Astronomical Society of the Pacific Conference Series*, page 243, Apr. 2009.

[76] E. J. Lentz, S. W. Bruenn, W. R. Hix, A. Mezzacappa, O. E. B. Messer, E. Endeve, J. M. Blondin, J. A. Harris, P. Marronetti, and K. N. Yakunin. Three-dimensional Core-collapse Supernova Simulated Using a 15 M_{sun} Progenitor. *ApJ*, 807:L31, July 2015.

[77] R. J. LeVeque, D. Mihalas, E. A. Dorfi, and E. Müller. *Computational Methods for Astrophysical Fluid Flow: Saas-Fee Advanced Course 27. Lecture Notes 1997. Swiss Society for Astrophysics and Astronomy (Saas-Fee Advanced Courses)*. Springer, 1998.

[78] M. Liebendörfer, O. E. B. Messer, A. Mezzacappa, S. W. Bruenn, C. Y. Cardall, and F.-K. Thielemann. A Finite Difference Representation of Neutrino Radiation Hydrodynamics in Spherically Symmetric General Relativistic Spacetime. *ApJS*, 150:263–316, Jan. 2004.

[79] M. Liebendörfer, A. Mezzacappa, and F.-K. Thielemann. Conservative general relativistic radiation hydrodynamics in spherical symmetry and comoving coordinates. *Phys. Rev. D*, 63(10):104003, May 2001.

[80] M. Liebendörfer, M. Rampp, H.-T. Janka, and A. Mezzacappa. Supernova Simulations with Boltzmann Neutrino Transport: A Comparison of Methods. *ApJ*, 620:840–860, Feb. 2005.

[81] M. Liebendörfer, S. Rosswog, and F.-K. Thielemann. An Adaptive Grid, Implicit Code for Spherically Symmetric, General Relativistic Hydrodynamics in Comoving Coordinates. *ApJS*, 141:229–246, July 2002.

[82] M. Liebendörfer, S. C. Whitehouse, and T. Fischer. The Isotropic Diffusion Source Approximation for Supernova Neutrino Transport. *ApJ*, 698:1174–1190, June 2009.

[83] R. W. Lindquist. Relativistic transport theory. *Annals of Physics*, 37:487–518, May 1966.

[84] Q. A. Mabanta and J. W. Murphy. How Turbulence Enables Core-collapse Supernova Explosions. *ApJ*, 856:22, Mar. 2018.

[85] M.-M. Mac Low and R. S. Klessen. Control of star formation by supersonic turbulence. *Reviews of Modern Physics*, 76:125–194, Jan. 2004.

[86] P. MacNeice, K. M. Olson, C. Mobarry, R. de Fainchtein, and C. Packer. PARAMESH: A parallel adaptive mesh refinement community toolkit. *Computer Physics Communications*, 126:330–354, Apr. 2000.

[87] A. Marek, H. Dimmelmeier, H.-T. Janka, E. Müller, and R. Buras. Exploring the relativistic regime with Newtonian hydrodynamics: an improved effective gravitational potential for supernova simulations. *A&A*, 445:273–289, Jan. 2006.

[88] A. Marek, H.-T. Janka, and E. Müller. Equation-of-state dependent features in shock-oscillation modulated neutrino and gravitational-wave signals from supernovae. *A&A*, 496:475–494, Mar. 2009.

[89] T. Melson, H.-T. Janka, R. Bollig, F. Hanke, A. Marek, and B. Müller. Neutrino-driven Explosion of a 20 Solar-mass Star in Three Dimensions Enabled by Strange-quark Contributions to Neutrino-Nucleon Scattering. *ApJ*, 808:L42, Aug. 2015.

[90] T. Melson, H.-T. Janka, and A. Marek. Neutrino-driven Supernova of a Low-mass Iron-core Progenitor Boosted by Three-dimensional Turbulent Convection. *ApJ*, 801:L24, Mar. 2015.

[91] B. S. Meyer. The r-, s-, and p-Processes in Nucleosynthesis. *ARA&A*, 32:153–190, 1994.

[92] B. S. Meyer, G. J. Mathews, W. M. Howard, S. E. Woosley, and R. D. Hoffman. R-process nucleosynthesis in the high-entropy supernova bubble. *ApJ*, 399:656–664, Nov. 1992.

[93] A. Mezzacappa and S. W. Bruenn. Stellar core collapse - A Boltzmann treatment of neutrino-electron scattering. *ApJ*, 410:740–760, June 1993.

[94] A. Mezzacappa and O. E. B. Messer. Neutrino transport in core collapse supernovae. *Journal of Computational and Applied Mathematics*, 109:281–319, Sept. 1999.

[95] D. Mihalas and B. W. Mihalas. *Foundations of radiation hydrodynamics*. Oxford University Press, 1984.

[96] G. N. Minerbo. Maximum entropy Eddington factors. *J. Quant. Spec. Radiat. Transf.*, 20:541–545, 1978.

[97] V. Morozova, D. Radice, A. Burrows, and D. Vartanyan. The Gravitational Wave Signal from Core-collapse Supernovae. *ApJ*, 861:10, July 2018.

[98] P. Mösta, C. D. Ott, D. Radice, L. F. Roberts, E. Schnetter, and R. Haas. A large-scale dynamo and magnetoturbulence in rapidly rotating core-collapse supernovae. *Nature*, 528:376–379, Dec. 2015.

[99] B. Müller and H.-T. Janka. Non-radial instabilities and progenitor asphericities in core-collapse supernovae. *MNRAS*, 448:2141–2174, Apr. 2015.

[100] B. Müller, T. Melson, A. Heger, and H.-T. Janka. Supernova simulations from a 3D progenitor model - Impact of perturbations and evolution of explosion properties. *MNRAS*, 472:491–513, Nov. 2017.

[101] B. Müller, M. Viallet, A. Heger, and H.-T. Janka. The Last Minutes of Oxygen Shell Burning in a Massive Star. *ApJ*, 833:124, Dec. 2016.

[102] E. Müller, H.-T. Janka, and A. Wongwathanarat. Parametrized 3D models of neutrino-driven supernova explosions. Neutrino emission asymmetries and gravitational-wave signals. *A&A*, 537:A63, Jan. 2012.

[103] J. W. Murphy and A. Burrows. Criteria for Core-Collapse Supernova Explosions by the Neutrino Mechanism. *ApJ*, 688:1159–1175, Dec. 2008.

[104] J. W. Murphy, J. C. Dolence, and A. Burrows. The Dominance of Neutrino-driven Convection in Core-collapse Supernovae. *ApJ*, 771:52, July 2013.

[105] H. Nagakura, W. Iwakami, S. Furusawa, H. Okawa, A. Harada, K. Sumiyoshi, S. Yamada, H. Matsufuru, and A. Imakura. Simulations of Core-collapse Supernovae in Spatial Axisymmetry with Full Boltzmann Neutrino Transport. *ApJ*, 854:136, Feb. 2018.

[106] K. Nakamura, T. Takiwaki, T. Kuroda, and K. Kotake. Systematic features of axisymmetric neutrino-driven core-collapse supernova models in multiple progenitors. *PASJ*, 67:107, Dec. 2015.

[107] E. O'Connor. An Open-source Neutrino Radiation Hydrodynamics Code for Core-collapse Supernovae. *ApJS*, 219:24, Aug. 2015.

[108] E. O'Connor and C. D. Ott. A new open-source code for spherically symmetric stellar collapse to neutron stars and black holes. *Classical and Quantum Gravity*, 27(11):114103, June 2010.

[109] E. O'Connor and C. D. Ott. Black Hole Formation in Failing Core-Collapse Supernovae. *ApJ*, 730:70, Apr. 2011.

[110] E. P. O'Connor and S. M. Couch. Two-dimensional Core-collapse Supernova Explosions Aided by General Relativity with Multidimensional Neutrino Transport. *ApJ*, 854:63, Feb. 2018.

[111] J. R. Oppenheimer and G. M. Volkoff. On Massive Neutron Cores. *Physical Review*, 55:374–381, Feb. 1939.

[112] J. P. Ostriker and J. E. Gunn. Do Pulsars Make Supernovae? *ApJ*, 164:L95, Mar. 1971.

[113] K.-C. Pan, M. Liebendörfer, S. M. Couch, and F.-K. Thielemann. Equation of State Dependent Dynamics and Multi-messenger Signals from Stellar-mass Black Hole Formation. *ApJ*, 857:13, Apr. 2018.

[114] K.-C. Pan, M. Liebendörfer, M. Hempel, and F.-K. Thielemann. Two-dimensional Core-collapse Supernova Simulations with the Isotropic Diffusion Source Approximation for Neutrino Transport. *ApJ*, 817:72, Jan. 2016.

[115] K.-C. Pan, C. Mattes, E. P. O'Connor, S. M. Couch, A. Perego, and A. Arcones. The impact of different neutrino transport methods on multidimensional core-collapse supernova simulations. *Journal of Physics G Nuclear Physics*, 46(1):014001, Jan. 2019.

[116] A. Perego, R. M. Cabezón, and R. Käppeli. An Advanced Leakage Scheme for Neutrino Treatment in Astrophysical Simulations. *ApJS*, 223:22, Apr. 2016.

[117] A. Perego, E. Gafton, R. Cabezón, S. Rosswog, and M. Liebendörfer. MODA: a new algorithm to compute optical depths in multidimensional hydrodynamic simulations. *A&A*, 568:A11, Aug. 2014.

[118] A. Perego, M. Hempel, C. Fröhlich, K. Ebinger, M. Eichler, J. Casanova, M. Liebendörfer, and F.-K. Thielemann. PUSHing Core-collapse Supernovae to Explosions in Spherical Symmetry I: the Model and the Case of SN 1987A. *ApJ*, 806:275, June 2015.

[119] A. Y. Potekhin, G. Chabrier, and F. J. Rogers. Equation of state of classical Coulomb plasma mixtures. *Phys. Rev. E*, 79(1):016411, Jan. 2009.

[120] Y.-Z. Qian and S. E. Woosley. Nucleosynthesis in Neutrino-driven Winds. I. The Physical Conditions. *ApJ*, 471:331, Nov. 1996.

[121] J. J. Quirk. A contribution to the great Riemann solver debate. *International Journal for Numerical Methods in Fluids*, 18:555–574, Mar. 1994.

[122] D. Radice, A. Burrows, D. Vartanyan, M. A. Skinner, and J. C. Dolence. Electron-capture and Low-mass Iron-core-collapse Supernovae: New Neutrino-radiation-hydrodynamics Simulations. *ApJ*, 850:43, Nov. 2017.

[123] S. Richers, C. D. Ott, E. Abdikamalov, E. O'Connor, and C. Sullivan. Equation of state effects on gravitational waves from rotating core collapse. *Phys. Rev. D*, 95(6):063019, Mar. 2017.

[124] S. Rosswog and M. Brüggen. *Introduction to High-Energy Astrophysics*. Cambridge University Press, Aug. 2007.

[125] S. Rosswog and M. Liebendörfer. High-resolution calculations of merging neutron stars - II. Neutrino emission. *MNRAS*, 342:673–689, July 2003.

[126] M. Ruffert and H.-T. Janka. Colliding neutron stars. Gravitational waves, neutrino emission, and gamma-ray bursts. *A&A*, 338:535–555, Oct. 1998.

[127] H. Shen, H. Toki, K. Oyamatsu, and K. Sumiyoshi. Relativistic Equation of State for Core-collapse Supernova Simulations. *ApJS*, 197:20, Dec. 2011.

[128] M. Shibata and K. Taniguchi. Coalescence of Black Hole-Neutron Star Binaries. *Living Reviews in Relativity*, 14:6, Aug. 2011.

[129] S. N. Shore. *Astrophysical Hydrodynamics: An Introduction*. Wiley, 2007.

[130] S. Simon and J. C. Mandal. A simple cure for numerical shock instability in the HLLC Riemann solver. *Journal of Computational Physics*, 378:477–496, Feb. 2019.

[131] M. A. Skinner, A. Burrows, and J. C. Dolence. Should One Use the Ray-by-Ray Approximation in Core-collapse Supernova Simulations? *ApJ*, 831:81, Nov. 2016.

[132] A. W. Steiner, M. Hempel, and T. Fischer. Core-collapse Supernova Equations of State Based on Neutron Star Observations. *ApJ*, 774:17, Sept. 2013.

[133] A. Summa, F. Hanke, H.-T. Janka, T. Melson, A. Marek, and B. Müller. Progenitor-dependent Explosion Dynamics in Self-consistent, Axisymmetric Simulations of Neutrino-driven Core-collapse Supernovae. *ApJ*, 825:6, July 2016.

[134] A. Summa, H.-T. Janka, T. Melson, and A. Marek. Rotation-supported Neutrino-driven Supernova Explosions in Three Dimensions and the Critical Luminosity Condition. *ApJ*, 852:28, Jan. 2018.

[135] Y. Suwa, T. Takiwaki, K. Kotake, T. Fischer, M. Liebendörfer, and K. Sato. On the Importance of the Equation of State for the Neutrino-driven Supernova Explosion Mechanism. *ApJ*, 764:99, Feb. 2013.

[136] T. Takiwaki, K. Kotake, and Y. Suwa. Three-dimensional Hydrodynamic Core-collapse Supernova Simulations for an 11.2 $M_\odot$ Star with Spectral Neutrino Transport. *ApJ*, 749:98, Apr. 2012.

[137] T. Takiwaki, K. Kotake, and Y. Suwa. A Comparison of Two- and Three-dimensional Neutrino-hydrodynamics Simulations of Core-collapse Supernovae. *ApJ*, 786:83, May 2014.

[138] T. A. Thompson, A. Burrows, and B. S. Meyer. The Physics of Proto-Neutron Star Winds: Implications for r-Process Nucleosynthesis. *ApJ*, 562:887–908, Dec. 2001.

[139] F. X. Timmes and D. Arnett. The Accuracy, Consistency, and Speed of Five Equations of State for Stellar Hydrodynamics. *ApJS*, 125:277–294, Nov. 1999.

[140] F. X. Timmes and F. D. Swesty. The Accuracy, Consistency, and Speed of an Electron-Positron Equation of State Based on Table Interpolation of the Helmholtz Free Energy. *ApJS*, 126:501–516, Feb. 2000.

[141] M. Ugliano, H.-T. Janka, A. Marek, and A. Arcones. Progenitor-explosion Connection and Remnant Birth Masses for Neutrino-driven Supernovae of Iron-core Progenitors. *ApJ*, 757:69, Sept. 2012.

[142] D. Vartanyan, A. Burrows, D. Radice, M. A. Skinner, and J. Dolence. Revival of the fittest: exploding core-collapse supernovae from 12 to 25 $M_\odot$. *MNRAS*, 477:3091–3108, July 2018.

[143] S. Wanajo. The r-process in Proto-neutron-star Wind Revisited. *ApJ*, 770:L22, June 2013.

[144] S. Wanajo, B. Müller, H.-T. Janka, and A. Heger. Nucleosynthesis in the Innermost Ejecta of Neutrino-driven Supernova Explosions in Two Dimensions. *ApJ*, 852:40, Jan. 2018.

[145] A. Wongwathanarat, H.-T. Janka, and E. Müller. Three-dimensional neutrino-driven supernovae: Neutron star kicks, spins, and asymmetric ejection of nucleosynthesis products. *A&A*, 552:A126, Apr. 2013.

[146] A. Wongwathanarat, H.-T. Janka, E. Müller, E. Pllumbi, and S. Wanajo. Production and Distribution of ^{44}Ti and ^{56}Ni in a Three-dimensional Supernova Model Resembling Cassiopeia A. *ApJ*, 842:13, June 2017.

[147] S. E. Woosley, A. Almgren, J. B. Bell, G. Glatzmaier, D. Kasen, A. R. Kerstein, H. Ma, P. Nugent, F. Röpke, V. Sankaran, and M. Zingale. Type Ia supernovae. In *Journal of Physics Conference Series*, volume 78 of *Journal of Physics Conference Series*, page 012081, July 2007.

[148] S. E. Woosley and A. Heger. Nucleosynthesis and remnants in massive stars of solar metallicity. *Phys. Rep.*, 442:269–283, Apr. 2007.

[149] S. E. Woosley, A. Heger, and T. A. Weaver. The evolution and explosion of massive stars. *Reviews of Modern Physics*, 74:1015–1071, Nov. 2002.

[150] S. E. Woosley and T. A. Weaver. The Evolution and Explosion of Massive Stars. II. Explosive Hydrodynamics and Nucleosynthesis. *ApJS*, 101:181, Nov. 1995.

[151] D. G. Yakovlev and D. A. Shalybkov. Effect of plasma screening on thermonuclear reaction rates. *Advances in Space Research*, 8:707–710, 1988.

[152] O. Yaron, D. A. Perley, A. Gal-Yam, J. H. Groh, A. Horesh, E. O. Ofek, S. R. Kulkarni, J. Sollerman, C. Fransson, A. Rubin, P. Szabo, N. Sapir, F. Taddia, S. B. Cenko, S. Valenti, I. Arcavi, D. A. Howell, M. M. Kasliwal, P. M. Vreeswijk, D. Khazov, O. D. Fox, Y. Cao, O. Gnat, P. L. Kelly, P. E. Nugent, A. V. Filippenko, R. R. Laher, P. R. Wozniak, W. H. Lee, U. D. Rebbapragada, K. Maguire, M. Sullivan, and M. T. Soumagnac. Confined dense circumstellar material surrounding a regular type II supernova. *Nature Physics*, 13:510–517, Feb. 2017.

Acknowledgments

Many thanks are due to those who supported me during my doctoral studies and in the preparation of this thesis.

In particular, I would like to express my sincere gratitude to my advisor Prof. Almudena Arcones for the continuous support, confidence, and patience. Her devotion made this work possible.

Besides my advisor, I would like to thank Prof. Sean Couch for the many support and help in all sorts of questions that I could ask anytime. I felt very welcome during my stay at the Michigan State University.

My sincere thanks also go to Dr. Albino Perego. Without his precious support, it would hardly have been possible to conduct this research. I also thank Kuo-Chuan Pan and Evan O'Connor for the good collaboration.
Special thanks go to my colleagues Maximilian Witt and Hannah Yasin who helped a lot during the project, and also thanks to Julia Bliss, Takami Kuroda, Martin Obergaulinger, and Moritz Reichert for the scientific discussions and corrections to this work.

Last but not the least, a big thank you to Martin Pospiech for the time together in the office and the coffee breaks, and many thanks to Susanne Horn and the small koala for the moral support on official journeys and especially during the difficult second half of my doctoral thesis.

This work was funded in the first year by a scholarship of the HGS-HIRe and subsequently by the SFB 1245. My visit to MSU was made possible by the travel price of SFB 1245 and the support by JINA-CEE. My participation in the TALENT summer school "Nuclear Physics of Neutron Stars and Supernovae" was supported by the INT at the University of Washington.

The computing time for the simulations presented in this work were provided by the HHLR at TU-Darmstadt (Project ID: 172 & 463) and by the CSCS at ETH-Zürich (Project ID: s667).

Curriculum Vitae

Carlos Mattes

November 18$^{\text{th}}$, 1988	Born in Frankfurt am Main, Germany
June 4$^{\text{th}}$, 2008	Abitur, Hohe Landesschule Hanau, Germany
2008 – 2012	Bachelor studies, TU Darmstadt, Germany
May 3$^{\text{rd}}$, 2012	Bachelor's degree, thesis title: "Influence of migration on the stability and dynamic of predator-prey systems“
2012 – 2015	Master studies, TU Darmstadt, Germany
September 22$^{\text{nd}}$, 2014	Master's degree, thesis title: "Long-time hydrodynamical simulation of core-collapse supernovae“
2015 – 2018	Doctoral studies and member of the scientific staff, TU Darmstadt, Germany

Erlärung zur Dissertation

Hiermit versichere ich, die vorliegende Dissertation ohne Hilfe Dritter nur mit den angegebenen Quellen und Hilfsmitteln angefertigt zu haben. Alle Stellen, die aus Quellen entnommen wurden, sind als solche kenntlich gemacht. Diese Arbeit hat in gleicher oder ähnlicher Form noch keiner Prüfungsbehörde vorgelegen. Eine Promotion wurde bisher noch nicht versucht.

Darmstadt, den 30. Januar 2019

(Carlos Mattes)